

University of Nottingham
UK | CHINA | MALAYSIA

HIGH RESOLUTION IMAGING OF THE HIPPOCAMPUS AT 7T

BY

ADEYEMI Oluwatobi Folorunsho

Thesis submitted to the University of Nottingham for the degree of Doctor of Philosophy

April 2023

ACKNOWLEDGEMENT

I would like to express my deepest gratitude and appreciation to all the people who have supported and encouraged me throughout my PhD journey.

First and foremost, I am immensely grateful to my supervisors Prof Richard Bowtell and Prof Penny Gowland, whose guidance and insights have been invaluable in shaping my research. Your patience, expertise, and unwavering support have been instrumental in helping me achieve my academic goals.

I am very grateful to Dr Olivier Mougin, his patience teaching me various techniques to process data, answering all my questions. It has all been a huge help. Your input has greatly improved the quality of my research.

I would like to extend my appreciation to my family, especially my wife (Adenike), Daughter (Nicole) and Son (Nathan), for their constant love, encouragement, and support throughout my PhD career. Without their unwavering support, this thesis would not have been possible.

I am also grateful to my friends and colleagues for their encouragement, inspiration, and motivation. Your support and encouragement have been a constant source of strength and inspiration for me.

Finally, I would like to thank the Almighty for the blessings and guidance throughout this journey.

Once again, thank you all for your invaluable support and encouragement.

TABLE OF CONTENT

ACKNOWLEDGEMENT i

TABLE OF CONTENT ii

LIST OF FIGURES vii

LIST OF TABLES xiv

ABSTRACT i

CHAPTER ONE 1

1.0 INTRODUCTION 1

1.1 OVERVIEW 1

1.1 AIM OF THE THESIS 4

1.2 SCOPE OF THE THESIS 5

1.4 REFERENCES 7

CHAPTER 2 9

2.0 NUCLEAR MAGNETIC RESONANCE AND MAGNETIC RESONANCE IMAGING THEORY 9

2.1 INTRODUCTION 9

2.2 NUCLEAR MAGNETIC RESONANCE 9

2.3 THE QUANTUM TO CLASSICAL MECHANICAL DESCRIPTION OF NMR 10

2.3.1 NUCLEAR MAGNETIC MOMENT 11

2.3.2 BOLTZMAN STATISTICS 13

2.3.3 THE BLOCH EQUATIONS 17

2.3.4 PRINCIPLE OF FREE INDUCTION DECAY (FID) 18

2.4 RELAXATION 18

2.4.2 LONGITUDINAL RELAXATION TIME T_1 19

2.4.3 TRANSVERSE RELAXATION TIME T_2 21

2.4.4 $\boldsymbol{T2*}$ TRANSVERSE DECAY RELAXATION TIME 21

2.5 STUDYING THE BRAIN WITH 7T MRI: SUSCEPTIBILITY STUDIES AND HIPPOCAMPAL SEGMENTATION 44

2.6 IMAGING 22

2.6.1 GRADIENTS FOR SPATIAL LOCALIZATION 22

2.6.2 SLICE SELECTION 23

2.6.3 FREQUENCY ENCODING 24

2.6.4 PHASE ENCODING 25

2.6.5 IMAGING SEQUENCES 26

2.7 MRI SAFETY 38

2.7.1 PROJECTILE EFFECT 39

2.7.2 VERTIGO 40

2.7.3 SAR (Specific Absorption Rate) 41

2.7.4 THERMAL INJURY 41

2.7.5 ACOUSTIC NOISE 42

2.8 REFERENCES 47

CHAPTER THREE 53

3.0 REPRODUCIBILITY OF 7T MEASUREMENTS OF THE SUSCEPTIBILITY AND VOLUME OF HIPPOCAMPAL SUBFIELDS 53

3.1 OUTLINE 53

3.2 INTRODUCTION 54

3.2.1 MAGNETIC SUSCEPTIBILITY MAPPING 55
3.2.2 MAGNETIC SUSCEPTIBILITY MEASUREMENT 56
3.2.3 QUANTITATIVE SUSCEPTIBILITY MAPPING 57
3.3 METHODS 59
3.3.1 IMAGING PROTOCOL 60
3.3.2 PREVIOUS WORK ON UK7T DATA FOR QSM REPRODUCIBILITY 61
3.3.3 QSM RECONSTRUCTION 63
3.3.4 AUTOMATIC SEGMENTATION OF HIPPOCAMPAL SUBFIELDS (ASHS) 64
3.4 RESULTS 66
3.4.1 REFERENCING THE QSM 66
3.4.2 ANALYSIS OF THE REAPEATED MEASUREMENTS 68
3.5 DISCUSSION 72
3.6 CONCLUSION 75
3.7 REFERENCES 76
CHAPTER FOUR 84
4.0 MEASUREMENT OF THE SUSCEPTIBILITY AND VOLUME OF HIPPOCAMPAL SUBFIELDS IN ALZHEIMER'S DISEASE PATIENTS 84
4.1 OUTLINE 84
4.2 DEMENTIA 85
4.2.1 CLASSIFICATION OF DEMENTIA 85
4.3 ALZHEIMER'S DISEASE 87
4.4 MRI AS A BIOMAKER FOR EARLY ALZHEIMER'S DISEASE 88
4.5 METHODS 89

4.5.1 STAFF ROLE AND PARTICIPANTS 89
4.5.2 IMAGING PROTOCOL 92
4.5.3 IMAGE PROCESSING AND ANALYSIS 93
4.5.3 STATISTICAL ANALYSIS 95
4.6 RESULTS 96
4.7 DISCUSSION 106
4.8 LIMITATIONS TO THE STUDY 110
4.9 CONCLUSION 111
4.9 REFERENCES 112
CHAPTER FIVE 119
5.0 VASCULARIZATION OF THE HIPPOCAMPUS 119
5.1 OUTLINE 119
5.2 INTRODUCTION 119
5.3 METHODS 125
5.3.1 OPTIMIZATION OF IMAGING SEQUENCES 125
5.3.2 METHODS AND IMAGING PROTOCOL 134
5.3.3 IMAGE PROCESSING AND ANALYSIS 134
5.4 RESULTS 138
5.5 DISCUSSION 148
5.6 CONCLUSION 150
5.7 REFERENCES 151
CHAPTER SIX 155
6.0 CONCLUSIONS 155

6.1 SUMMARY 155

6.2 FUTURE WORK 157

6.3 REFERENCE 159

LIST OF FIGURES

Figure 1. 1: This image showcases the high-resolution capabilities of the 7T MRI scanner at the Sir Peter Mansfield Imaging Centre, University of Nottingham. A) Phase-Sensitive Inversion Recovery (PSIR) image with a voxel size of 0.8 × 0.8 × 0.8 mm³, B) T2-weighted image with a voxel size of 0.4 × 0.4 × 1.0 mm³, and C) 3D T2*-weighted Gradient Echo (GRE) image with a voxel size of 0.38 × 0.37 × 0.74 mm³. The total acquisition time for the three scans combined was 27 minutes and 21 seconds. These high-resolution images allow for greater detail in the study of various medical conditions, enabling more accurate diagnosis and monitoring. 4

Figure 2.1: The difference in energy between spins in the up and down states due to the magnetic field. The energy difference leads to a small difference in the population of the two states giving rise to a net magnetisation. 12

Figure 2.2: The Precession of the magnetization vector in a static magnetic field aligned along the z-axis. 15

Figure 2.3: A perturbing magnetic field, rotating at precisely the Larmor frequency, causes the magnetization simultaneously to precess about the z-axis at frequency $\omega 0$ and about the x-axis at frequency $\omega 1$ 16

Figure 2.4: Free Induction Decay (FID) of the nuclear magnetic resonance signal 18

Figure 2.6: Inversion recovery gradient echo sequence, showing RF pulses and the formation of a gradient echo, the amplitude of which will depend on the inversion time. 20

Figure 2.7: A schematic for the Spin Echo sequence 21

Figure 2.8: Selective excitation of an image slice by applying a shaped RF pulse and a field gradient at the same time.(McRobbie et al., 2009) 24

Figure 2.9: A schematic representation of an MPRAGE imaging sequence with spoiler gradrient 28

Figure 2. 10: T_1 weighted image in Sagittal, coronal and Axial views 29

Figure 2. 11: shows a schematic representation of the Fast Spin Echo/Turbo Spin Echo (FSE/TSE) sequence. 30

Figure 2.12: shows a T_2 weighted image obtained using the FSE/TSE sequence 31

Figure 2.13: FLAIR image 32

Figure 2.14: The FLAIR sequence 33

Figure 2.15: A) showing a T_2* (Gradient Echo) image, B) showing SWI (Susceptibility Weighted image) and C) the minimum intensity projection of the SWI 34

Figure 2.16: The GRE sequence 35

Figure 2.17: shows an example of TOF image with 0.38 mm isotropic resolution 7:23min acquisition time, TR= 14 TE= 4.5 FA=22 multi-chunk with 4 chunks each of thickness 8.36 mm. 37

Figure 2.18: Direct contact burn (a) Photograph shows a third-degree burn on a patient's calf, which was pressed against the cable of the radiofrequency coil. (b) Photograph shows a phased array coil similar to the one involved in the incident. The coil cable showed no indication of a burn. The arrow indicates the approximate contact point (Tsai et al., 2015). 42

Figure 3.1: Axial slices at the level of the globus pallidus and optic radiations taken from the QSM maps of one participant from each of the 5 sites in this study (A) Subj01 (B) Subj03 (C) Subj05 (D) Subj07 and (E) Subj09. 64

Figure 3.2: TSE images showing the segmented subfields of the hippocampus of one participant from each of the 5 sites in this study (A) Subj01 (B) Subj03 (C) Subj05 (D) Subj07 and (E) Subj09. 65

Figure 3. 3: shows a three-plane view of 0.7 mm resolution susceptibility map of one of the subjects, with an overlay of the ASHS segmentation of the hippocampus. This figure provides a visual representation of the segmentation of the hippocampus and the distribution of magnetic susceptibility across the subfields. 66

Figure 3. 4: illustrates an example of the manually defined region of interest (ROI) for cerebrospinal fluid (CSF) in red, overlaid on the T2-weighted image. These ROIs were used to measure the susceptibility values of CSF, which were then subtracted from the susceptibility values of other regions of interest to obtain a value of susceptibility referenced to CSF. This referencing method was compared to the default referencing to the average susceptibility in the whole brain volume considered in the analysis 67

Figure 3. 5: The average across the 10 participants of the value of the standard deviation of the five susceptibility measurements in ppm, with and without referencing to the CSF. 68
Figure 3. 6: Plots showing the A) susceptibility (ppm), B) Absolute volume (mm^3) and C) Percentage volume (%) averaged over the five repeat measurements of the subfields of the hippocampus for the 10 different subjects. Error bars show the standard deviation across repeated measurements. 69
Figure 3. 7**:** shows the average values of A) susceptibility B) Absolute volume and C) TIV-scaled percentage volume in the different subfields of the hippocampus for the ten participants. The error bars indicate the standard deviation across participants. 69
Figure 3. 8: Values of (A) susceptibility for sub07 (B) susceptibility for sub08 (C) volume of sub07 (D) volume for sub08 (E) TIV-scaled volume for sub07 (F) TIV-scaled volume for sub08, for the five repeated measurements at the Nottingham site. 70
Figure 4.1: Comparison between a healthy brain and a brain with Alzheimer's disease. In AD the cortex shrinks, especially in the hippocampal region which is responsible for forming new memories. The ventricles which are fluid filled cavities in the brain, consequently enlarge. Taken from https://commons.wikimedia.org/wiki/File:Alzheimer%27s_disease_brain_comparison.jpg 87
Figure 4.2: T2*-weighted image (left) and corresponding quantitative susceptibility map (QSM) (right) obtained for one of the participants in the study. The QSM data was generated using QSMbox (Acosta-Cabronero et al., 2018) to produce a susceptibility map spanning the whole brain..... 93
Figure 4.3: Coronal view of MRI images obtained for one of the participants in the study. The images include PSIR, T2-weighted, and QSM images, with the segmentation of the hippocampus overlaid on the T2-weighted image. 94
Figure 4.4: Showing the whole brain segmentation of the PSIR image for one slice in an image of one of the participants. Whole brain volume was used for scaling the volume of the hippocampal subfields into a percentage volume. 95
Figure 4.5: Showing the average volume of the whole brain for 11 Alzheimer's disease (AD) participants and 11 healthy controls. Error bars show the standard deviation across participants in each group. The difference in average volume between the AD patients and controls was not statistically significant..... 97

Figure 4. 6: Showing A) the average percentage volume and the absolute volume of the whole hippocampus for AD participants and healthy controls (HC). B) The average susceptibility of the whole hippocampus for AD participants and HCs. There was a statistically significant difference between the AD and controls for the volume of the hippocampus, but no difference statistically for the susceptibility. 98

Figure 4.7: A) The average relative volumes of the hippocampal subfields in AD patients and healthy controls (as a percentage of the whole brain volume) B) the average susceptibility values for the AD and HC. The error bars represent the standard deviation of the measurements.* means comparison of values for AD and HC yields a statistically significant difference with $p \leq 0.05$, ** means $p < 0.01$ while no sign means that the values are not significantly different. 99

Figure 4. 8: Scatter plots showing the relationship between the absolute volume and relative volume of the whole hippocampus and the concentration of CSF Amyloidβ1-42 or MoCA Score, with the linear relationship on the trend line indicated. Orange circles represent measurements from AD participants, while blue circles show HC values. CSF Amyloidβ1-42 measurements were only made on AD participants. 101

Figure 4 9: (Top) Scatter plot showing the relationship between the susceptibility of the whole hippocampus and CSF Amyloidβ1-42 concentration in AD participants.(Bottom) Scatter plot showing the relationship between the susceptibility of the whole hippocampus the MoCA score in AD participants and healthy controls.. The orange squares represent the values for the AD participants and the blue circles show values for the healthy controls 103

Figure 4. 10: Scatter plots showing the relationship between (A) relative volume (%) or (B) susceptibility (ppm) of the hippocampal subfields of AD participants and the value of MoCA score. Linear fits are indicated by the trend lines. * means they have $p \leq 0.05$, ** $p < 0.01$ and no sign means they are not significant. 105

Figure 4.11: Scatter plots showing the relationship between (A) relative volume (%) or (B) susceptibility (ppm) of the hippocampal subfields of AD participants and the concentration of CSF Amyloidβ1-42. in pg/ml. Linear fits are indicated by the trend lines. * means they have $p \leq 0.05$, ** $p < 0.01$ and no sign means they are not significant. 106

Figure 5.1: pictorial representation of different group categorizations of hippocampal arterial supply, showing the intra and extraventricular view of the hippocampus. See text for further explanation. CA: Calcarine artery; ICA: Internal carotid artery, PCA: Posterior cerebral artery, POA: Parieto-occipital artery, AITA: Anterior inferior temporal artery, MITA: Medial inferior temporal artery, PITA: Posterior inferior temporal artery, AChA: Anterior choroidal artery. 1, 2, 3, and 4: Hippocampal arteries'. (Isolan et al., 2020). 122

Figure 5.2: schematic showing the inflow effect in the TOF sequence for a 3D angiography. Ideally the velocity of flow must be sufficient so that the blood is replenished (refreshed) across the thickness of the whole slab in the repetition time (TR) of the FFE pulse sequence. The relationship between velocity and flow rate is also shown. In a real 3D slab it is likely that multiple small vessels will be emanating from a single point of entry at the distal end of the slab. 126

Figure 5.3: a plot of the A) signal of blood and tissue against the flip angle for different TR for the tissue B) the contrast of blood against flip angle for different TR and C) contrast against the specific absorption rate. 128

Figure 5.4a: showing the sagittal, coronal and axial of the three TOF MRA sequences investigated i) TOF1 4 stack scan ii) TOF2 with 0.34mm isotropic resolution and iii) TOF3 with 0.38mm isotropic resolution covering the entire hippocampus. This was use for the identification of the arteries around the hippocampus 130

Figure 5.5: Showing the 3 sequences use for the generation of the SWI to identify the veins in this study as shown in Table 5.2..... 133

Figure 5.6: The Axial, sagittal and coronal view of the hippocampus segmentation and it overlaid on the T_2-weigthed..... 135

Figure 5. 7: A) The Time of Flight (TOF) B) the maximum intensity projection of the TOF for one of the participants in the study and C) the TOF (red) covering the entire hippocampus as acquired from the scanner. 136

Figure 5.8: shows A) the magnitude image of the SE T_2* sequence and B) the magnitude image of the SWI obtained after processing A. 137

Figure 5.9: showing the arteries (red) and veins (blue) overlaid on the segmentation of the hippocampus for Subject 1. The images are taking from different orientations to show the vascularization clearly around the hippocampus. Subj01 exhibited a vasculature pattern aligned with group A from Isolan et al., featuring a combination of PCA, AchA, AIA, and SA as the sources of hippocampus arteries... 140
Figure 5.10: showing the arteries (red) and veins (blue) overlaid on the segmentation of the hippocampus for Subject 2. The images are taking from different orientations to show the vascularization clearly around the hippocampus 141
Figure 5.11: showing the arteries (red) and veins (blue) overlaid on the segmentation of the hippocampus for Subject 3. The images are taking from different orientations to show the vascularization clearly around the hippocampus 141
Figure 5. 12: showing the arteries (red) and veins (blue) overlaid on the segmentation of the hippocampus for Subject 4. The images are taking from different orientations to show the vascularization clearly around the hippocampus 142
Figure 5. 13: showing the arteries (red) and veins (blue) overlaid on the segmentation of the hippocampus for Subject 5. The images are taking from different orientations to show the vascularization clearly around the hippocampus 142
Figure 5. 14: showing the arteries (red) and veins (blue) overlaid on the segmentation of the hippocampus for Subject 6. The images are taking from different orientations to show the vascularization clearly around the hippocampus 143
Figure 5. 15: showing the arteries (red) and veins (blue) overlaid on the segmentation of the hippocampus for Subject 7. The images are taking from different orientations to show the vascularization clearly around the hippocampus 143
Figure 5. 16: showing the arteries (red) and veins (blue) overlaid on the segmentation of the hippocampus for Subject 8. The images are taking from different orientations to show the vascularization clearly around the hippocampus 144
Figure 5. 17: show the complete vasculature of the hippocampus i.e a combination of both the artery (red) and veins (blue) and a 2D presentation overlaid on the segmentation of the hippocampus for subject 8. 144

Figure 5.18: showing the hippocampus vascularisation pattern observed in subject 1; on the left is the TOF MRA image and on the left is the pattern from (Isolan et al., 2020) study. PCA: Posterior cerebral artery (red), AChA: Anterior choroidal artery (blue) and (PITA: Posterior inferior temporal artery/HA: Hippocampal arteries/AITA: Anterior inferior temporal artery) are in green 145
Figure 5.19: showing the hippocampus vascularisation pattern observed in subject 3; on the left is the TOF MRA image and on the left is the pattern from (Isolan et al., 2020) study. PCA: Posterior cerebral artery (red), AChA: Anterior choroidal artery (blue) and (PITA: Posterior inferior temporal artery/HA: Hippocampal arteries/AITA: Anterior inferior temporal artery) are in green 145
Figure 5.20: showing the hippocampus vascularisation pattern observed in subject 4; on the left is the TOF MRA image and on the left is the pattern from (Isolan et al., 2020) study. PCA: Posterior cerebral artery (red), AChA: Anterior choroidal artery (blue) and (PITA: Posterior inferior temporal artery/HA: Hippocampal arteries/AITA: Anterior inferior temporal artery) are in green 146
Figure 5.21: showing the hippocampus vascularisation pattern observed in subject 2; on the left is the TOF MRA image and on the left is the pattern from (Isolan et al., 2020) study. PCA: Posterior cerebral artery (red), AChA: Anterior choroidal artery (blue) and (PITA: Posterior inferior temporal artery/HA: Hippocampal arteries/AITA: Anterior inferior temporal artery) are in green. 146
Figure 5.22: showing the pattern of hippocampal vascularisation observed in subject 5 (left), subject 6 (right) and subject 8 (bottom); the central image is the pattern from (Isolan et al., 2020) study. PCA: Posterior cerebral artery (red), AChA: Anterior choroidal artery (blue). 147
Figure 5.23: comparing A) the Cadaver image of the hippocampus (Wen et al., 1999) with B) our image of the arteries overlaid on the hippocampus and C) veins overlaid on the hippocampus. 1, anterior choroidal artery; 2, inferior surface of the posterior segment of the uncus; 3, P2A segment of the posterior cerebral artery; 4, basal vein; 5, dentate gyrus and fimbria; 6, anterior and posterior longitudinal hippocampal veins; 7, pulvinar of the thalamus; 8, P2P segment of the posterior cerebral artery; *, hippocampal arteries; **, lateral posterior choroidal artery.. 148

LIST OF TABLES

Table 2.1: T_1 at 7T for different tissues (Rooney et al., 2007)..... 20

Table 3.1**:** Scanner systems used at each site for data acquisition in the UK7T travelling head study. 60

Table 3. 2: Average value of the susceptibility, absolute volume and percentage volume across the 10 participants and the respective standard deviations across subjects and the average of the standard deviation over repeats across all participants. 71

Table 3. 3: coefficient of variation analysis of the absolute volume and TIV corrected volume for standard deviation across subjects and that across the repeated scans..... 71

Table 3. 4 Coefficient of variation (COV) analysis for segmented hippocampal subfields in participants sub07 and sub08 from the UK7T study, COV calculated as the standard deviation over repeated measurements divided by the mean. 71

Table 4.1: The results of applying a one–way ANOVA statistical test for differences between AD patients and HC in measurements of the volume and susceptibility of each hippocampal subfield. The mean, standard deviation and standard errors for each measurement are shown for the AD and HC groups and for all 22 participants..... 100

Table 4.2: Linear regression analysis to characterise the correlation between the value of absolute volume, relative volume and susceptibility with CSF Amyloidβ1-42 /MoCA score for AD participants, only with age as covariant. The Pearson correlation is reported for the 11 AD participant 102

Table 4.3: Linear correlation analysis of the value of relative volume or susceptibility of each hippocampal subfield with CSF Amyloidβ1-42 concentration or MoCA score for the Alzheimer disease participants. .* means that a statistically significant correlation with $p \leq 0.05$ is found, while ** means that $p < 0.01$. 104

Table 5. 1: the TOF sequences investigated, 3D FFE flow compensated sequence with the sense on 128

Table 5. 2: summary of the T_2* sequence investigated for better identification of the venous system of the hippocampus 132
Table 5. 3: Subject demographics and assigned group for arteries 139

Navigating the Storm: The Impact of COVID-19 on my Ph.D. research Journey during Lockdown

The COVID-19 pandemic brought unforeseen challenges to individuals worldwide, and as an aspiring Physics Ph.D. student, my journey was no exception. The lockdown measures during the pandemic resulted in the closure of the University, making it impossible to scan participants, collect crucial data, and advance my research as planned. The sudden halt to my research posed a significant challenge, leaving me uncertain about the future of my academic pursuits.

The uncertainties brought about by the pandemic took an emotional toll on me. The inability to progress in my research during lockdown tested my resilience and dedication. The sense of stagnation amidst my academic journey weighed heavily on my mind, as I grappled with the desire to contribute to the field, I am passionate about.

Like many researchers worldwide, I had to adapt to remote learning and virtual engagement to continue my academic journey. Online meetings and video conferences replaced in-person interactions, necessitating adjustments to my learning style and communication with my supervisors and peers. Despite these challenges, I persevered, seeking new ways to make progress in my research.

During the lockdown, I found a way to continue my work using already existing scans from the UK7T to further my research. I focused on exploring the reproducibility volume and susceptibility of the Hippocampus subfields. This innovative approach allowed me to forge ahead with my Ph.D. work despite the limitations posed by the pandemic.

In conclusion, the impact of COVID-19 on my MRI Physics Ph.D. journey has been significant, presenting me with unprecedented challenges during the lockdown. University closures, limited resources, and the emotional toll disrupted my research progress, but my resilience and determination shone through. By adapting to remote learning and finding

creative solutions, I managed to continue my work and make strides in my Ph.D. research. As I face the future, I became more determined than ever to overcome obstacles and contribute meaningfully to the field I am passionate about.

ABSTRACT

Magnetic Resonance Imaging (MRI) is a powerful medical imaging technique that provides detailed visualization of internal structures in vivo, making it an indispensable tool in diagnosing and monitoring brain-related diseases and pathologies. In this thesis, we focus on the hippocampus, a critical brain region for memory and learning, and investigate its susceptibility, volume, and vascularization using high-resolution MRI at 7T.

Firstly, we estimate the reproducibility of hippocampal subfield susceptibility and volume in healthy participants to determine the precision required for longitudinal studies aimed at tracking changes in the hippocampus in Alzheimer's disease.

Secondly, we compare the susceptibility and volume of hippocampal subfields between healthy controls and Alzheimer's disease patients to investigate whether they can be used as biomarkers for early detection of AD. We also examine the relationship between hippocampal subfield measurements, the abnormal protein Amyloidβ1-42 in cerebrospinal fluid (CSF), and cognitive performance measured by the Montreal Cognitive Assessment (MoCA).

Thirdly, we investigate the non-invasive visualization of hippocampal vasculature to better understand its pattern, which is critical for surgical planning. We aim to map the vascularity of the hippocampus in vivo without contrast agents to gain insight into the relationship between vascular and degenerative pathology of the hippocampus.

Our findings have implications for the diagnosis, monitoring, and treatment of Alzheimer's disease and provide insights into the structure and function of the hippocampus.

CHAPTER ONE

1.0 INTRODUCTION

1.1 OVERVIEW

Magnetic Resonance Imaging (MRI) is a medical imaging technique that uses magnetic fields and radio waves to generate detailed images of internal organs and tissues in the body based on the phenomenon of Nuclear Magnetic Resonance (NMR). The invention of MRI is attributed to a number of scientists and engineers who made important contributions to its development.

One of the earliest pioneers of NMR was the physicist Felix Bloch, who in 1946 (Bloch et al., 1946) discovered that atomic nuclei, when placed in a magnetic field, could absorb and emit radio frequency energy. Building on this discovery, in 1952, Bloch and Edward Purcell, independently developed the technique of NMR, which could be used to study the molecular structure of solids and liquids. Their work earned them the Nobel Prize in Physics in 1952.

In the 1970s, two scientists, Paul Lauterbur and Peter Mansfield, independently developed methods to create images using NMR. In 1973 (Lauterbur, 1973), Lauterbur published a paper demonstrating the first magnetic resonance image, which he created by encoding spatial information into the NMR signal and later in 1973 Peter Mansfield proposed a method of spatial encoding based on interference phenomena (diffraction) (P. Mansfield & Grannell, 1973)

In 1974 Peter Mansfield put forward his work on image formation using NMR (Garroway et al., 1974). Together, Lauterbur and Mansfield are credited with developing the foundations of modern MRI. In recognition of their contributions, they were jointly awarded the Nobel Prize in Physiology or Medicine in 2003.

Since their pioneering work, MRI has become an essential diagnostic tool in medicine. It is used to diagnose a wide range of conditions, including neurological disorders, cancers, and musculoskeletal injuries (Dean Deyle, 2011,Whiteley et al., 2022, Haris et al., 2015). It is also used to guide medical procedures, such as biopsies and surgeries (Thompson et al., 2017).

There are many MRI scanners used today around the world. According to a study by (McRobbie et al., 2017), there were over 10,000 MRI scanners in the world as early as 1996. By 2008, the number had risen to about 20,000, as reported by Blamire (Blamire, 2008). This rapid growth in the number of MRI scanners is a testament to the importance of this technology in modern healthcare.

MRI is a powerful diagnostic tool that provides detailed images of the internal structures of the body. It can visualize not only tumours, ischemic strokes and bleeds (Ergun et al., 2010), but also provides functional images of the brain and body (G. H. Glover, 2011), as well as images of moving parts like the beating heart (Earls et al., 2002) and the foetus in the mother's womb (Saleem, 2014). This makes it a versatile imaging modality that is used across a wide range of medical specialties.

One of the major advantages of MRI is its ability to provide images that are superior to other imaging modalities such as X-ray and CT scans, especially in soft tissue such as the abdominal and pelvic regions (Oldendorf, 1988). While most pathologies can be seen in both CT and MRI scans, MRI is usually superior when it comes to detailed characterization of pathological lesions (Zaidman et al., 2013). This is particularly important in the diagnosis and monitoring of cancer, where MRI is used to detect and track changes in tumour size, shape, and activity over time.

The growth in the number of MRI scanners used around the world reflects the increasing demand for accurate and detailed diagnostic imaging in modern healthcare. MRI's ability to provide high-resolution images of internal structures and soft tissue areas, as well as functional

and dynamic information, makes it an essential tool in the diagnosis and treatment of a wide range of medical conditions.

MRI technology has come a long way since the first full human body scan was carried out in 1977 by Damadian and colleagues (Damadian et al., 1977). In those early days, acquiring an MRI image could take hours and the field strengths were relatively low. However, with advancements in MRI technology, high-quality high-resolution images as can be seen in fig 1.1 can now be acquired at a much quicker pace using high-field scanners such as the 7T scanner available at the Sir Peter Mansfield Imaging Centre at the University of Nottingham. In fact, the same research group is currently working on developing an even more powerful 11.7T human scanner.

These high-field MRI scanners have allowed us to study the human body with an unprecedented level of detail. For example, the higher spatial resolution achieved by high-field scanners (as shown in Figure 1.1) has enabled researchers to identify subtle changes in brain structures and to study the structural and functional connectivity of the brain. High-field scanners have also improved our ability to detect and monitor various medical conditions, including neurological disorders, cancer, and cardiovascular disease (Dean Deyle, 2011,Whiteley et al., 2022).

In addition to providing higher resolution images, high-field MRI scanners have also reduced the need for invasive procedures. For instance, MRI-guided biopsies are now routinely performed, allowing for more accurate and targeted sampling of tissues for diagnosis (Thompson et al., 2017).

Overall, the continued development and expansion of MRI technology has transformed the way we diagnose and treat various medical conditions. With the ability to produce high-resolution images of the human body in a non-invasive manner, MRI has become an essential tool for healthcare providers around the world.

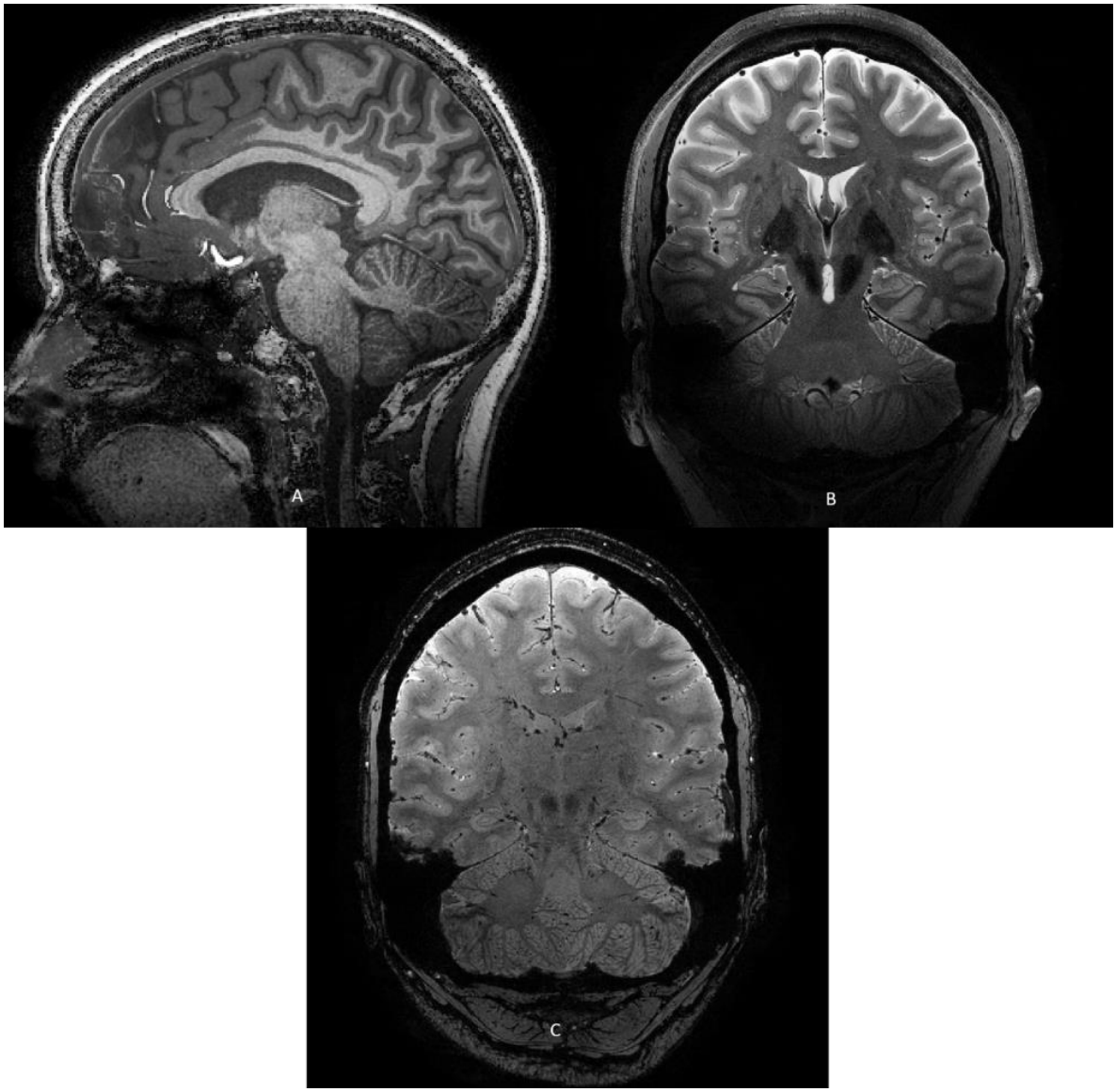


Figure 1. 1: This image showcases the high-resolution capabilities of the 7T MRI scanner at the Sir Peter Mansfield Imaging Centre, University of Nottingham. A) Phase-Sensitive Inversion Recovery (PSIR) image with a voxel size of 0.8 × 0.8 × 0.8 mm³, B) T2-weighted image with a voxel size of 0.4 × 0.4 × 1.0 mm³, and C) 3D T2-weighted Gradient Echo (GRE) image with a voxel size of 0.38 × 0.37 × 0.74 mm³. The total acquisition time for the three scans combined was 27 minutes and 21 seconds. These high-resolution images allow for greater detail in the study of various medical conditions, enabling more accurate diagnosis and monitoring.*

1.1 AIM OF THE THESIS

The primary objectives of this thesis are as follows:

1. To determine the reproducibility of magnetic susceptibility and volume measurements in the subfields of the hippocampus for healthy participants. By establishing the expected level of variability in repeated measurements, we aim to provide a better

understanding of the attainable precision for planning longitudinal studies to track changes in the hippocampus associated with Alzheimer's and other diseases.

2. To use high-resolution volumetric and quantitative susceptibility mapping techniques to produce susceptibility and volume measurements for both Alzheimer's disease patients and healthy controls. Our aim is to investigate whether these measurements can serve as potential biomarkers for detecting atrophy and changes in iron levels in the hippocampal subfields, thereby facilitating early detection of Alzheimer's disease. Additionally, we aim to study the correlation between hippocampal subfield volume and susceptibility, cerebrospinal fluid Amyloidβ1-42 levels, and Montreal Cognitive Assessment scores, in order to explore a non-invasive alternative for Alzheimer's disease diagnosis.

3. To non-invasively visualize the vascularization of the hippocampus, in order to better understand the pattern of vessels that supply and drain the hippocampus. This is particularly relevant for surgical procedures around the hippocampus, as detailed in vivo maps of the vasculature could help identify potential risks and ensure the success of such procedures

1.2 SCOPE OF THE THESIS

This thesis explores the potential use of high spatial resolution imaging to visualize the vasculature of the hippocampus (i.e., the arteries and veins that supply and drain blood from the hippocampus), as well as volumetric and susceptibility mapping of the hippocampus as a biomarker for AD patients using ultra-high field magnetic resonance imaging. The thesis comprises six chapters.

Chapter 2 provides an introduction to the theory of nuclear magnetic resonance (NMR) and magnetic resonance imaging (MRI), including the MR imaging techniques used in this thesis (especially on the 7T Achieva system) and MRI safety considerations.

Chapter 3 investigates the reproducibility of measurements of the magnetic susceptibility and volume of the hippocampal subfields in healthy participants. This study uses data that was acquired as part of a travelling head study carried out on five different 7T scanners linked to the UK7T consortium. We describe the segmentation of the hippocampus using the Automatic Segmentation of Hippocampal Subfields (ASHS) software package and susceptibility mapping of the whole brain using the QSMbox software. We then statistically compare the results obtained to determine the reproducibility of each region of interest (ROI) in the hippocampus.

Chapter 4 focuses on the analysis of the volume and susceptibility of the whole hippocampus and its subfields in Alzheimer's disease patients, with a view to establishing a biomarker for early detection of this devastating disease. We also examine the relationship between hippocampal volume and susceptibility, and the levels of Amyloid$\beta_{1\text{-}42}$ measured in the cerebrospinal fluid (CSF), as well as Montreal Cognitive Assessment (MoCA) results.

Chapter 5 describes the non-invasive visualization of the arterial and venous supply of the hippocampus using a 7T MRI scanner without the use of a contrast agent. We identify and analyse the major vessels supplying and draining the hippocampus, which is important for carrying out successful surgeries around the hippocampus.

Chapter 6, the final chapter, provides a general conclusion of the work carried out in the thesis and highlights possible avenues for future research to build on the findings of this thesis.

1.4 REFERENCES

Blamire, A. M. (2008). The technology of MRI - The next 10 years? *British Journal of Radiology*, *81*(968), 601–617. https://doi.org/10.1259/bjr/96872829

Bloch, F., Hansen, W. W., & Packard, M. (1946). The Nuclear Induction Experiment. *Pysical Review*, *70*(5).

Damadian, R., Golsmith, M., & L.Minkoff. (1977). NMR in cancer XVI. FONAR image.pdf. In *Physiological Chemistry and Physics* (Vol. 9, pp. 97–100).

Earls, J. P., Ho, V. B., Foo, T. K., Castillo, E., & Flamm, S. D. (2002). Cardiac MRI: Recent progress and continued challenges. *Journal of Magnetic Resonance Imaging*, *16*(2), 111–127. https://doi.org/10.1002/jmri.10154

Ergun, T., Lakadamyali, H., & Derincek, A. (2010). Magnetic Resonance Imaging in the Visualization of Benign Tumors and Tumor-like Lesions of Hand and Wrist. *Current Problems in Diagnostic Radiology*, *39*(1), 1–16. https://doi.org/10.1067/j.cpradiol.2009.01.002

Garroway, A. N., Grannell, P. K., & Mansfield, P. (1974). Image formation in NMR by a selective irradiative process. *Journal of Physics C: Solid State Physics*, *7*(24). https://doi.org/10.1088/0022-3719/7/24/006

Glover, G. H. (2011). Overview of functional magnetic resonance imaging. *Neurosurgery Clinics of North America*, *22*(2), 133–139. https://doi.org/10.1016/j.nec.2010.11.001

Haris, M., Yadav, S. K., Rizwan, A., Singh, A., Wang, E., Hariharan, H., Reddy, R., & Marincola, F. M. (2015). Molecular magnetic resonance imaging in cancer. *Journal of Translational Medicine*, 1–16. https://doi.org/10.1186/s12967-015-0659-x

Lauterbur, P. . (1973). © 1973 Nature Publishing Group. *Nat. Phys. Sci.*, *22*, 190–191. https://www.nature.com/articles/242190a0

Mansfield, P., & Grannell, P. K. (1973). NMR ’ diffraction ’ in solids ? *Journal of Physics C:*

Solid State Physics, *6*.

McRobbie, D. W., Moore, E. A., Graves, M. J., & Prince, M. R. (2017). *MRI from Picture to Proton* (3rd ed.). Cambridge University Press. https://doi.org/https://doi.org/10.1017/9781107706958

Oldendorf, W. (1988). Chapter 8: advantages and disadvantages of mri. In *Basics of Magnetic Resonance Imaging* (Issue 1, pp. 125–126). Springer, Boston, MA.

Saleem, S. N. (2014). Fetal MRI: An approach to practice: A review. *Journal of Advanced Research*, *5*(5), 507–523. https://doi.org/10.1016/j.jare.2013.06.001

Thompson, S. M., Gorny, K. R., Jondal, D. E., Rech, K. L., Mardini, S., & Woodrum, D. A. (2017). *MRI-guided Wire Localization Surgical Biopsy in an Adolescent Patient with a Difficult to Diagnose Case of Lymphoma*. 135–138. https://doi.org/10.1007/s00270-016-1464-5

Whiteley, W. N., Macraild, A., Wang, Y., Dennis, M., Al-Shahi Salman, R., Gray, A., Reed, M. J., Graham, C., & Wardlaw, J. M. (2022). Clinical Diagnosis and Magnetic Resonance Imaging in Patients with Transient and Minor Neurological Symptoms: A Prospective Cohort Study. *Stroke*, *53*(11), 3419–3428. https://doi.org/10.1161/STROKEAHA.122.039082

Zaidman, C. M., Seelig, M. J., Baker, J. C., Mackinnon, S. E., & Pestronk, A. (2013). Detection of peripheral nerve pathology: Comparison of ultrasound and MRI. *Neurology*, *80*(18), 1634–1640. https://doi.org/10.1212/WNL.0b013e3182904f3f

CHAPTER 2

2.0 NUCLEAR MAGNETIC RESONANCE AND MAGNETIC RESONANCE IMAGING THEORY

2.1 INTRODUCTION

This chapter delves into the physical principles of NMR and MRI, explaining the concept of nuclear spin and its interactions with magnetic fields. The various factors affecting the resonance frequency of different nuclei, including the strength of the magnetic field, are also discussed. The process of signal acquisition and reconstruction is explored in detail, as well as the different types of MR pulse sequences, such as T1-weighted, T2-weighted, and diffusion-weighted imaging. The hardware components of the MR scanner, including the magnet, gradient coils, and radiofrequency coils, are also explained, along with their roles in the MR signal acquisition process. Finally, MRI safety concerns are discussed, including the potential risks associated with magnetic fields, acoustic noise, and contrast agents.

2.2 NUCLEAR MAGNETIC RESONANCE

The discovery of nuclear magnetic resonance (NMR) by Rabi, Bloch and Purcell (Rabi, 1937, Bloch et al., 1964, Purcell, 1946) has led to one of the most important applications of physics in medicine - magnetic resonance imaging (MRI). MRI uses NMR to obtain images of the human body, and has become an indispensable tool in clinical diagnostics due to its non-invasive nature and high spatial resolution. The basic principle behind MRI is that the nuclei of certain atoms, such as hydrogen in water, can be made to resonate when placed in a strong magnetic field and subjected to a radiofrequency pulse. The resulting signals can be detected and used to reconstruct an image of the body. MRI has revolutionized the field of medical

imaging, allowing physicians to visualize the internal structures of the body in unprecedented detail, leading to improved diagnosis and treatment of many diseases.

NMR has revolutionized our ability to study the behaviour of molecules and atoms in all kinds of matter, from simple gases to complex biological systems. It has been instrumental in advancing our understanding of chemistry, physics, and materials science. By studying the behaviour of atoms and molecules in different environments, we can gain insight into a wide range of physical and biological processes, including protein folding, chemical reactions, and disease processes. The ability to non-invasively image internal structures and processes in the human body has also made MRI an invaluable tool in modern medicine, enabling earlier and more accurate diagnosis of a wide range of diseases. The applications of NMR and MRI continue to expand, with new techniques and technologies constantly being developed to push the limits of what is possible.

NMR has a wide variety of applications today because it allows the chemical environment of atoms to be probed. NMR uses strong magnetic fields and low-energy photons (radiofrequency) to manipulate the spins of atomic nuclei (Giunta & Mainz, 2020). Nuclei have three fundamental characteristics: mass, charge and spin. Spin is an intrinsic property of nuclei, it is not physical movement of the particle like classical angular momentum (Holger Försterling, 2009; Levitt et al., 1986).

2.3 THE QUANTUM TO CLASSICAL MECHANICAL DESCRIPTION OF NMR

NMR is the phenomenon that results from the interaction between atomic nuclei (specifically, their angular momentum) and an external magnetic field. This interaction is fundamentally quantum in nature. While the behaviour of a single nucleus can be predicted using quantum mechanics, it becomes much more complex when dealing with a large number of nuclei. In the

following section, we will first provide a quantum model description of NMR before describing it in classical terms.

2.3.1 NUCLEAR MAGNETIC MOMENT

Similar to the way that electrons have a magnetic dipole moment (from the electron spin and the orbital quantum number), protons and neutrons also have their own magnetic dipole moment. A magnetic dipole moment ($\vec{\mu}$) is created when a positive or negative electric current moves in a circle (current loop). In a simple current loop, $\vec{\mu}$ depends on the current *I* and the area *A* that the loop encloses

$$|\vec{\mu}| = IA \qquad [2.1]$$

We can use the Bohr magneton to estimate the magnetic moment of the proton and neutron as

$$\mu_N = \frac{e\hbar}{2m_p} \qquad [2.2]$$

where e is the charge of the proton, $\hbar$ is Planck's constant scaled by 2π and m_p is the mass of the proton.

In quantum mechanical terms, the nuclear magnetic moment of a nucleus with a spin quantum number *I* can align with an externally applied magnetic field of strength B_0 in $2I+1$ ways, with each way characterized by the spin quantum number m which can take integer or half-integer values ranging from -*m* to *m*. For a single nucleus with $I = \frac{1}{2}$ the spin can be aligned with or against the applied field B_0. The energetically preferred orientation has the magnetic moment aligned parallel with the applied field $\left(m = +\frac{1}{2}\right)$ and is often given the notation α, whereas the higher energy, anti-parallel orientation $\left(m = -\frac{1}{2}\right)$ is referred to as the β state. The rotational axis of the spinning nucleus cannot be oriented exactly parallel (or anti-parallel) with the direction of the applied field B_0 (defined in our coordinate system as about the *z* axis), but

must precess (motion similar to a gyroscope) about this field at an angle, with an angular velocity given by the expression:

$$\omega_0 = \gamma B_0 \qquad [2.3]$$

where ω_0 is the precession rate called the Larmor frequency. The constant γ is called the gyromagnetic ratio.

Each nucleus has a characteristic value of γ, which is defined as the constant of proportionality between the nuclear angular momentum and magnetic moment. For a hydrogen nucleus, γ = 2.674×10^8 $s^{-1}T^{-1}$. This precession of the magnetic moment generates a magnetic field that oscillates at frequency ω_0. If a sample containing precessing nuclei is surrounded by a coil of wire, a voltage will be induced in the coil by the time-varying magnetic field via electromagnetic induction. This voltage forms the NMR signal. If we irradiate the sample with radio waves (MHz) the spins can absorb energy and be promoted to the higher energy state. This absorption is called a resonance because the frequency of the applied radiation and the precession must coincide or resonate for energy absorption to take place.

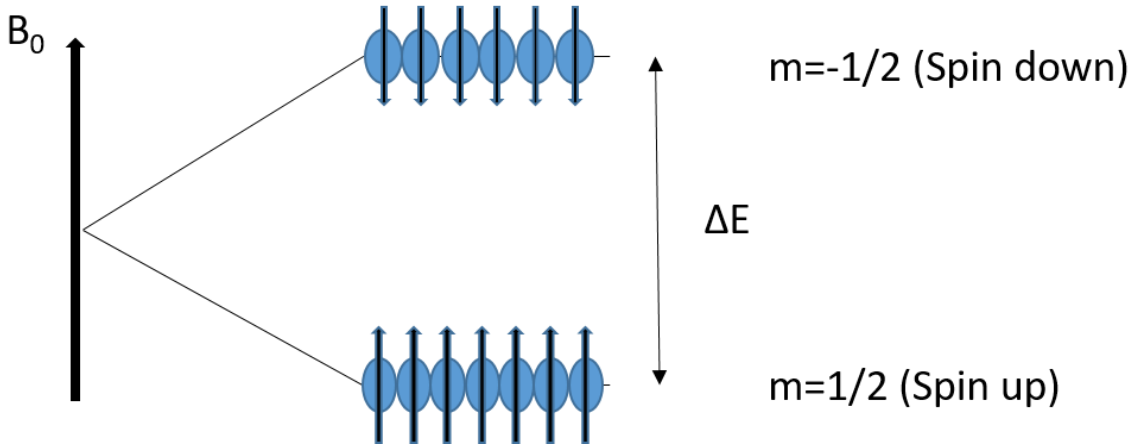


Figure 2.1: The difference in energy between spins in the up and down states due to the magnetic field. The energy difference leads to a small difference in the population of the two states giving rise to a net magnetisation.

When discussing NMR, spin state energy separations are often characterized by the frequency required to induce a transition between the states. While frequency is not a measure of energy, the simple relationship E=hυ (where E=energy, h=Planck's constant, and υ=frequency) makes this substitution understandable.

2.3.2 BOLTZMAN STATISTICS

In water, in the absence of a magnetic field, the hydrogen nuclei present all have magnetic moments which point in different directions, therefore generating a net magnetization of zero. When a magnetic field, B_0, is applied, there are only two possible states for each hydrogen atom, whose magnetic moment can be aligned with the field or against the field. The energy difference ΔE between these two states is given by

$$\Delta E = \gamma \hbar B_0. \qquad [2.4]$$

This energy difference means that at equilibrium the number in each state is different as there is a preference to be in the low energy state. This difference can be derived from the Boltzmann distribution:

$$\frac{N\uparrow}{N\downarrow} = \exp\left(\frac{\Delta E}{k_B T_s}\right) \qquad [2.5]$$

where $N\uparrow$ and $N\downarrow$ are the number of spins that are aligned with and against the field, respectively, T_s is the temperature of the spin system and k_B is the Boltzmann constant. The net magnetization of the sample is given by summing the contributions of the spins pointing with and against the field

$$M_0 = \frac{\gamma\hbar}{2} N\uparrow - \frac{\gamma\hbar}{2} N\downarrow = N_s \frac{\left(\frac{\gamma\hbar}{2}\exp\left(\frac{\gamma\hbar B_0}{2k_B T_s}\right) - \frac{\gamma\hbar}{2}\exp\left(-\frac{\gamma\hbar B_0}{2k_B T_s}\right)\right)}{\exp\left(\frac{\gamma\hbar B_0}{2k_B T_s}\right) + \exp\left(-\frac{\gamma\hbar B_0}{2k_B T_s}\right)} \qquad [2.6]$$

where N_s is the number of hydrogen nuclei in the sample. Making the high temperature approximation $\gamma\hbar B_0 \ll k_B T_s$, which applies at the fields and temperatures that are relevant for MRI this simplifies to

$$M_0 = \frac{\gamma^2 \hbar^2 B_0 N_s}{4 k_B T_s} \quad [2.7]$$

Applying a B_1 RF field in a direction perpendicular to the spins at their resonance (Larmor) frequency causes the system of spins to absorb energy and hence tip the net magnetization vector toward the transverse plane. This creates a net transverse magnetization vector. This vector will precess about the external field and begin to relax towards net alignment with the external field again. The motion of the net magnetization is guided by a set of equations known as the Bloch equations. These are the equations of motion for the net magnetization vector **M** of a sample of spins placed in a main magnetic field B_0 (where the components of M are M_x, M_y and M_z)

The magnetic moment **M** classically of a spin in a magnetic field **B** will experience a torque that can be represented by the equation below

$$\frac{d\boldsymbol{M}}{dt} = \gamma \boldsymbol{M} \times \boldsymbol{B} \quad [2.8]$$

Assuming that the magnetic field is applied in the z direction, Eq. [2.8] can be written

$$\frac{dM_x}{dt} = \gamma M_y B_0$$

$$\frac{dM_y}{dt} = -\gamma M_x B_0 \quad [2.9]$$

$$\frac{dM_z}{dt} = 0$$

with solution

$$M_x(t) = M_x(0)\cos\omega_0 t + M_y(0)\sin\omega_0 t$$

$$M_y(t) = -M_x(0)\sin\omega_0 t + M_y(0)\cos\omega_0 t \quad [2.10]$$

$$M_z(t) = M_z(0).$$

These equations describe the precession of the magnetic moment about the z-axis with angular frequency $\omega_0 = \gamma B_0$ (Larmor frequency).

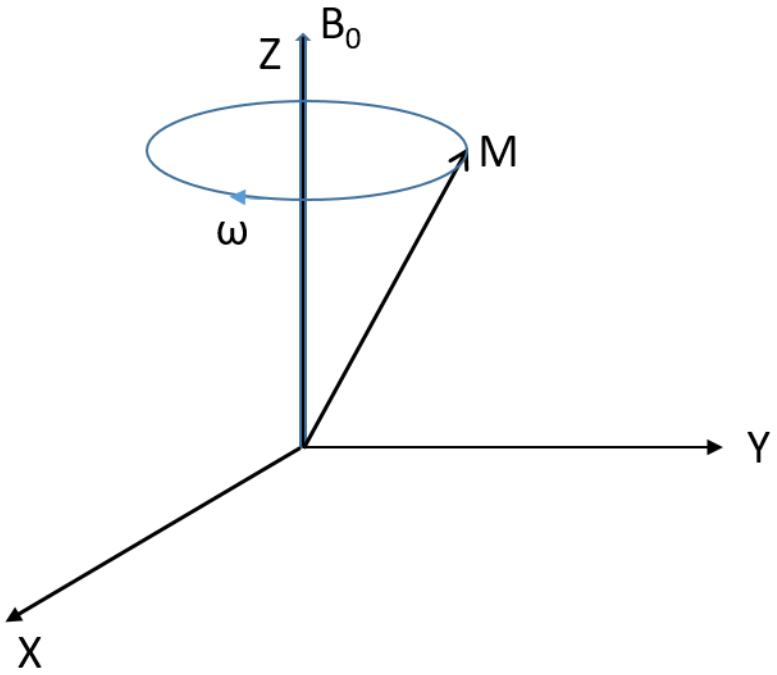


Figure 2.2: The Precession of the magnetization vector in a static magnetic field aligned along the z-axis.

If we now consider the effect of applying a time-varying magnetic field $\boldsymbol{B_1}$ perpendicular to B_0, oscillating at the Larmor frequency, then B_1 can be expressed as

$$\boldsymbol{B_1}(t) = B_1 \cos \omega_0 t\, \boldsymbol{i} - B_1 \sin \omega_0 t\, \boldsymbol{j} \qquad [2.11]$$

where $\boldsymbol{i}$, $\boldsymbol{j}$ and $\boldsymbol{k}$ are the Cartesian unit vectors along the *x*-, *y*- and *z*-directions. The Larmor frequency is generally in the radiofrequency range so the B_1 field is often called an RF field.

Hence Eq. [2.10] becomes

$$\frac{dM_x}{dt} = \gamma\left[M_y B_0 + M_z B_1 \sin \omega_0 t\right]$$

$$\frac{dM_y}{dt} = \gamma[M_z B_1 \cos\omega_0 t - M_x B_0] \qquad [2.12]$$

$$\frac{dM_z}{dt} = \gamma\left[-M_x B_1 \sin\omega_0 t - M_y B_1 \cos\omega_0 t\right]$$

Considering a starting condition $M(0) = M_0\boldsymbol{k}$ then the solution for $\boldsymbol{M}$ is

$$M_x(t) = M_0 \sin\omega_1 t \sin\omega_0 t$$

$$M_y(t) = M_0 \sin\omega_1 t \cos\omega_0 t \qquad [2.13]$$

$$M_z(t) = M_0 \cos\omega_1 t$$

Here $\omega_1 = \gamma B_1$, hence when we apply an oscillating magnetic field of frequency ω_0 the magnetization precesses about B_0 and B_1 at rates ω_0 and ω_1, as shown in Fig. 2.3 below.

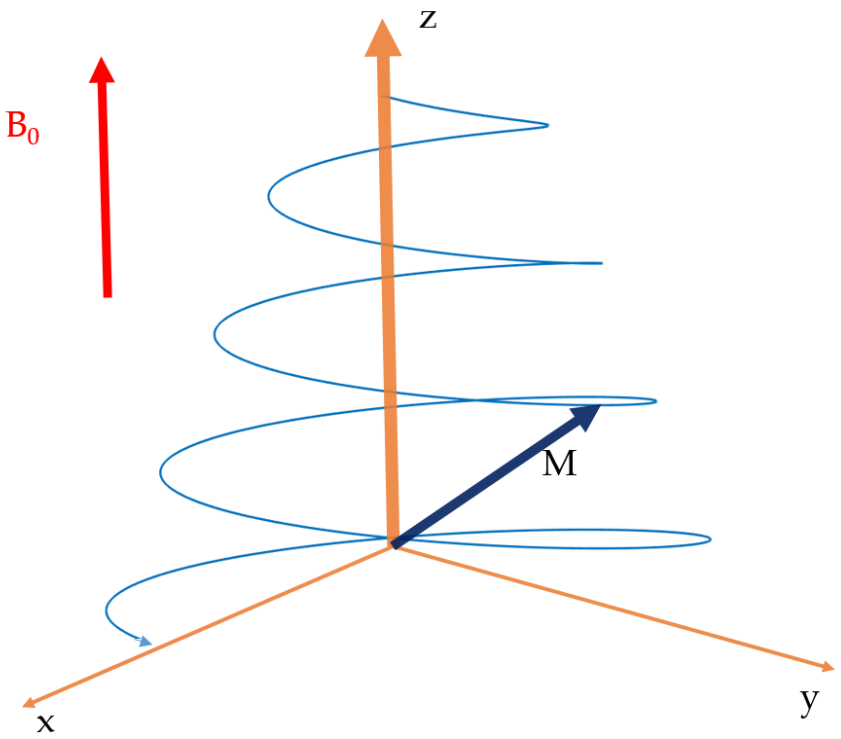


Figure 2.3: A perturbing magnetic field, rotating at precisely the Larmor frequency, causes the magnetization simultaneously to precess about the z-axis at frequency ω_0 and about the x-axis at frequency ω_1.

2.3.3 THE BLOCH EQUATIONS

Nuclear magnetic resonance (NMR) concepts are rooted in quantum mechanics, but MR imaging principles are well described and more easily grasped using classical ideas and formalisms such as Larmor precession and the phenomenological Bloch equations (Lauzon, 2020).

In NMR and MRI, the spins or magnetic moments are exposed to a strong external magnetic field which will cause more spins to align parallel with the magnetic field than anti-parallel to it (see Eq. 2.6). The small excess of spins aligned with the field produces a weak net magnetization known as the equilibrium magnetization M_0.

This motion of the magnetization vector of uncoupled spins is easily expressed in terms of the Bloch equations. Almost all MRI concepts, dynamics and experiments are described by the Bloch equations. These equations relate the macroscopic model of magnetization to the applied radiofrequency, gradient and static magnetic fields.

The Bloch equation given in Eq. (2.8 - 2.12) can be used to describe the behavior of the magnetization in the presence of B_1 fields

$$\frac{dM_x}{dt} = -\frac{M_x}{T_2} \qquad [2.14]$$

$$\frac{dM_y}{dt} = \gamma M_z B_1(x,t) - \frac{M_y}{T_2} \qquad [2.15]$$

$$\frac{dM_z}{dt} = -\gamma M_y B_1(x,t) + \frac{M_0 - M_z}{T_1} \qquad [2.16]$$

where M_x and M_y describes the transverse magnetization, and M_z is the longitudinal magnetization. M_0 is the equilibrium magnetization along the z-direction. $B_1(x)$ is the radio frequency (RF) magnetic field, T_1 is the spin-lattice relaxation time, T_2 is the transverse or spin-spin relaxation time and γ is the gyromagnetic ratio

2.3.4 PRINCIPLE OF FREE INDUCTION DECAY (FID)

The application of an RF pulse can generate rotating magnetization in the transverse plane, which then induces a varying EMF in the RF coil (according to Faraday's law) which forms the NMR signal. This signal depends on the strength and rate of precession of the net magnetization. The magnetization that is generated by this pulse, decays, producing a free induction decay (FID) with the signal generally described by

$$\mathrm{I} = \mathrm{I}_0 e^{i\omega t} \mathrm{e}^{-\frac{\mathrm{t}}{\mathrm{T}_2^*}} \qquad [2.17]$$

where T_2* is so called relaxation time, a constant describing the rate of decay of the magnetization, which is discussed further below.

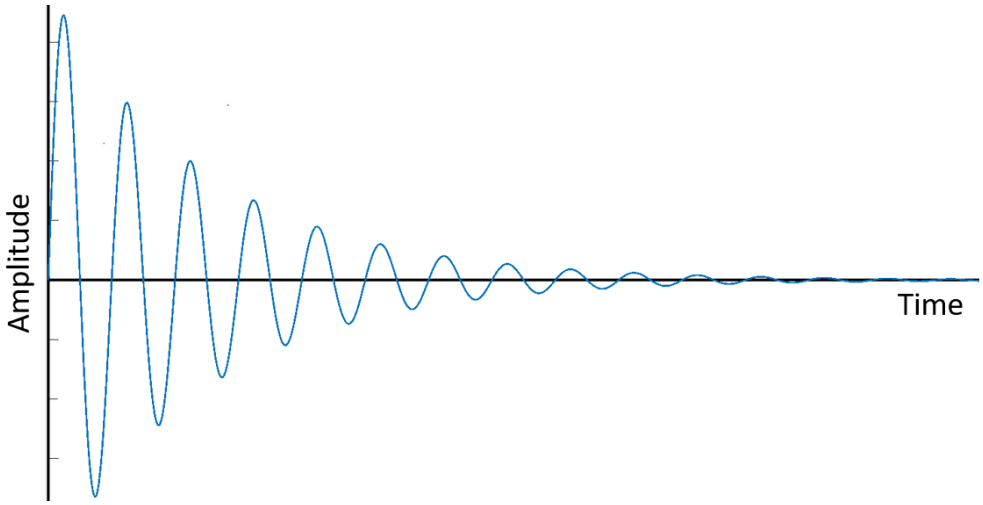


Figure 2.4: Free Induction Decay (FID) of the nuclear magnetic resonance signal

2.4 RELAXATION

Relaxation describes the behaviour of the net magnetization which is formed from the sum of the magnetic moments of all spins. However, to understand the mechanisms of relaxation we will initially look at the fate of individual spins. The rate at which the net longitudinal magnetization vector builds up again to the equilibrium value after the pulse is characterized by the T_1 (or longitudinal) relaxation time. The rate at which the transverse magnetization vector decays is characterized by the T_2 (or transverse) relaxation time. T_1 and T_2 are two of the parameters that strongly influence the amplitude of the magnetic resonance signal. Their

values depend on the molecular environment of the tissue and can allow the distinction of different types of tissues (Stanisz et al., 2005).

Put simply, T_1 parameterizes how rapidly a system of spins changes its total energy and T_2 parameterizes how fast the spins within the system go out of phase in a perfectly uniform external magnet field B_0, whereas T_2* also includes the effect of inhomogeneities in B_0 on the dephasing of the spins (Harlow & Pitre, 2014).

2.4.2 LONGITUDINAL RELAXATION TIME T_1

T_1 characterizes the time required for a system of spin magnetic moments to reach thermal equilibrium after a perturbation (e.g. application of an RF pulse or a change in the strength of the static magnetic field, B_0) is applied. For example, in the process of saturation recovery where the longitudinal magnetization is zero at time *t=0*, the subsequent evolution of M_z is described by a solution to the Bloch Equation with boundary condition, M(0) = 0:

$$M_z(t) = M_0\left(1 - e^{-\frac{t}{T_1}}\right) \qquad [2.18]$$

For a system to reach thermal equilibrium there must be an exchange of energy between the spins and the lattice, hence T_1 (spin-lattice or the longitudinal relaxation time) depends on the mechanisms available for the spins to transfer energy to other repositories of thermal energy such as the translations, rotations, vibrations, and excitations of the surroundings, collectively called the lattice (Bloembergen et al., 1948).

Measurement of T_1 is important as it provides useful information about the tissues that generate the signal (Caused, 2018) with T_1 values varying significantly across different tissue types, as can be seen in the table below

TISSUE	**T_1(ms)**
Grey Matter	2132 ±103

White matter	1220 ±36
CSF	4425 ±137
Blood	2587 ±283

Table 2.1: T_1 at 7T for different tissues (Rooney et al., 2007)

Inversion recovery is one of the most commonly used methods to determine T_1. In this method, we apply an 180^0 inversion pulse, which inverts the magnetization from the +z axis to the –z axis. The longitudinal magnetization is then allowed to relax back towards the +z axis, and then a 90^0 pulse is applied which flips the magnetization into the xy plane for signal detection. This process is illustrated in Fig. 2.6; by varying TI (the time between the 180^o and 90^0 pulses, the longitudinal recovery curve can be plotted and T1 can be measured. Eq (2.18) for $TR > 5T_1$

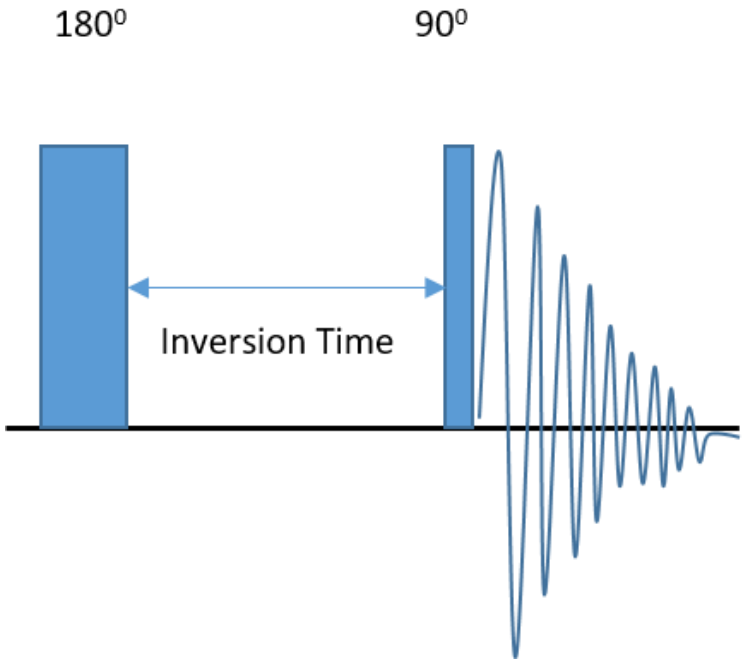


Figure 2.5: Inversion recovery gradient echo sequence, showing RF pulses and the formation of a gradient echo, the amplitude of which will depend on the inversion time.

2.4.3 TRANSVERSE RELAXATION TIME T_2

T_2, known as the spin-spin or the transverse relaxation time describes the rate of reduction of magnetization in the transverse plane which comes about because of the interaction between spins in the system: spins move out of phase with each other due to fluctuating magnetic fields generally from the spins themselves. Such phase coherence changes can occur without any energy being lost or gained by the spin system. The decay of transverse magnetization in the rotating frame is described in Eq. [2.19] below

$$M(t) = M_0 e^{-\frac{t}{T_2^*}} \qquad [2.19]$$

When a 90^0 pulse is applied to the system, the magnetization is tipped into the transverse plane. When the RF pulse is turned off, the spins undergo both a longitudinal recovery and transverse decay because of the spin-spin interactions between and the resulting phase dispersion. This process is described by the equation below

$$M_{xy}(t) = M_{xy}(0)\left(e^{-\frac{TE}{T_2^*}}\right) \qquad [2.20]$$

In the process described above the relaxation measured is the T_2^* relaxation, given by equation [2.19]. But when we apply an 180^0 pulse along the same axis after the first 90^0 pulse, this reverses the phase accumulated and leads to a refocusing and echo formation (see Fig. 2.7). The amplitude of the spin echo (SE) that is formed depends only on the true T_2 decay. The time between the initial excitation and time we acquire the image is called the echo time (TE) (Jung & Weigel, 2013). By applying multiple 180^0 inversion pulses, the signal can be refocused multiple times producing a train of echoes that can be used for T_2 measurement.

Figure 2.6: A schematic for the Spin Echo sequence.

2.4.4 T_2^* TRANSVERSE DECAY RELAXATION TIME

T_2* is the time constant that describes the decay of transverse magnetization when the effect of static magnetic field inhomogeneities is included (whereas T_2 is due to time varying effects).

For example, immediately after the application of a 90^0 pulse, all the magnetic moments are aligned, but if there are inhomogeneities in the static magnetic field over the sample then different magnetic moments will precess at different rates, producing a dephasing which attenuates the net transverse magnetization and hence the measured NMR signal.

As we can see from Eq. (2.10), signal measured after the application of RF pulse decays exponentially with time and the decay time is characterized by T_2^*. T_2^* depends on both T_2 and also T_2' which characterizes the effect of field inhomogeneity:

$$\frac{1}{T_2^*} = \frac{1}{T_2} + \frac{1}{T_2'} \qquad [2.21]$$

2.5 IMAGING

The total signal generated from the entire sample after an RF pulse excitation has been previously discussed, but for the signal to be used to generate meaningful images it needs to be encoded in such a way we can discriminate signal from different parts of the sample. Lauterbur and Mansfield received a Nobel prize in 2003 in recognition of their description of the different ways in which we can spatially localize the NMR signal received from a sample (P. Mansfield, 1977, Lauterbur, 1973, Peter Mansfield & Grannell, 1973). There are several methods or techniques to achieve this process, some of the main ones used in this research work will be discussed in this section.

2.5.1 GRADIENTS FOR SPATIAL LOCALIZATION

To generate images in the scanner we need to be able to spatially localize signals from different parts of the body. We can achieve this by adding a small magnetic field to the main magnetic field of the scanner B_0, this changes the resonance frequency ω_0 of the sample. The gradient coils of the scanner generate spatially varying magnetic fields. These field are weaker than B_0

and vary linearly along the x, y and z axes, with gradients described by Gx, G_y and G_z. The amplitude of the z-component of the magnetic field at point **r** is given by

$$B_z(r) = B_0 + \boldsymbol{G} \cdot \boldsymbol{r} \qquad \textbf{[}2.22]$$

where

$$\mathbf{G}.\mathbf{r} = G_x x + G_y y + G_z z \qquad .$$

2.5.2 SLICE SELECTION

Whenever a RF pulse is applied to a sample, only spins with their resonance frequencies within the bandwidth of the pulse are excited. In the presence of a field gradient, a 90^0 RF pulse only tips into the x-y plane the spins precessing within the range of frequencies found in the pulse (McRobbie et al., 2009). This process is called selective excitation and it produces a thin slice of excited spins. The thickness of the excited slice, Δz depends on the amplitude of the applied gradient G_z and the bandwidth of the RF pulse, $\Delta\omega$

$$\Delta z = \frac{\Delta\omega}{\gamma G_z} \qquad [2.23]$$

The slice select gradient pulse applied is a positive lobe followed by a negative lobe of half the duration. The negative lobe is used to rephase the signal which is dephased by the application of the gradient during the RF pulse.

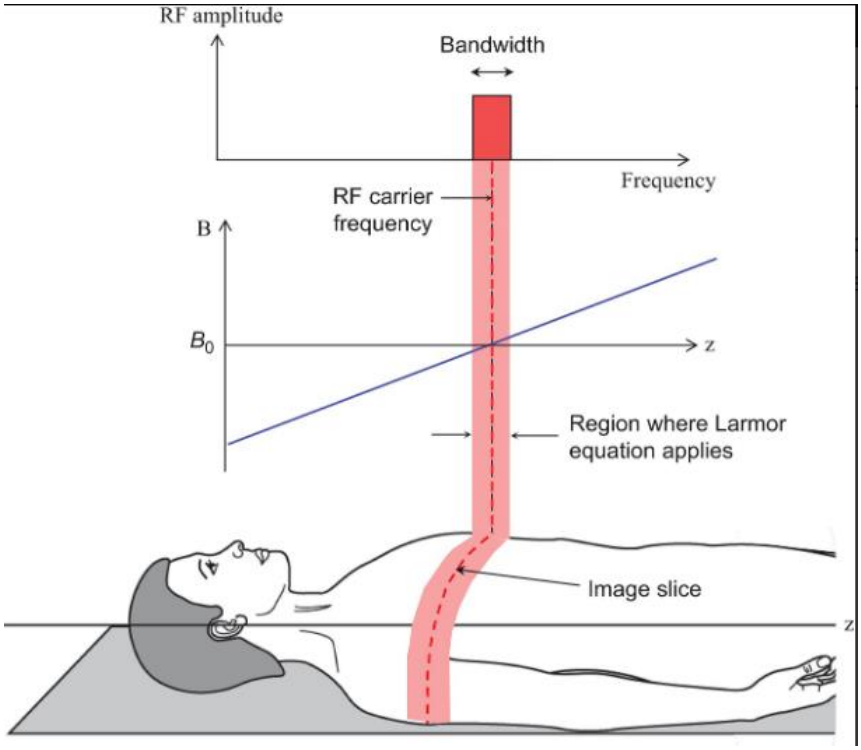


Figure 2.7: Selective excitation of an image slice by applying a shaped RF pulse and a field gradient at the same time.(McRobbie et al., 2009)

2.5.3 FREQUENCY ENCODING

Frequency encoding is a technique used to encode the position from which the signal arises within a slice along one dimension. If a field gradient is applied in the x-direction, the net magnetic field in the z-direction is given by:

$$B_z = B_0 + Gx \quad . \qquad [2.24]$$

where G is the strength of the gradient. The frequency encoding gradient creates a gradient in the precession frequencies of the excited protons along the same direction. This causes the resonant frequency of the protons to vary linearly with position:

$$\omega_0(x) = \gamma B_z = \gamma(B_0 + Gx) \qquad [2.25]$$

where γ is the gyromagnetic ratio. Fourier transformation of the signal, which separates it into its constituent frequencies, can consequently be used to identify how the signal strength varies along the x-axis, producing a one-dimensional image.

For each dimension in the image, frequency encoding requires a different magnetic field gradient strength. If we want to obtain an image in two dimensions, we need to apply gradients in both x and y directions. The strength and duration of the gradients applied determine the resolution and the size of the image that can be obtained. The signal obtained from each frequency-encoded step is stored as a separate column in the k-space matrix, and the spacing of the measurements in k-space determines the field-of-view (FOV) of the image obtained.

Frequency encoding is also used to introduce a spatially varying phase shift in the signal, which can be further manipulated using phase encoding gradients, as described in the previous section.

The concept of k-space was introduced by Lauterbur in 1973 (Lauterbur, 1973) and refined by Ernst et al. in 1986 (Ernst et al., 1987). It is the space in which the signal is acquired before being Fourier transformed into the Cartesian space. Low spatial frequencies (coarse image structures) appear close to the origin while higher spatial frequencies (edges and fine detail) appear at the outer edges of k-space. The further from the centre of k-space, the better the resolution of the image reconstructed.

2.5.4 PHASE ENCODING

Phase encoding is a technique used in MRI to spatially encode the MR signal. In phase encoding, we apply a gradient for a short time. When the gradient is on and for example applied in the y-direction, it causes the frequency of precession to vary along the y-axis, and its net effect is to cause a variation of the signal phase that is proportional to the y-position. When the gradient is turned off, the spins revert to their original frequency but keep the phase change that they have gained. By repeating the acquisition with phase encoding gradients that vary in strength or duration, a series of signals are generated in which the phase evolves from one signal to the next at a rate that depends on the y-position. This phase encoding of the y-position of signal sources can be unravelled by Fourier transformation.

For every line of data, we require one MR signal (i.e., if we have an image that is 256 x 256 in dimensions, we are required to do 256 phase-encoding steps). The phase-encoding steps are stored in the k-space matrix as different rows. k-space was conceptualized in 1983 (Stig, 1983) for visualizing the path of the spin phase as influenced by the gradient field. k-space is the space in which the signal is acquired before being Fourier transformed into the Cartesian space. Low spatial frequencies (coarse image structures) appear close to the origin while higher spatial frequencies (edges and fine detail) appear at the outer edges of k-space. The spacing of the measurements in k-space dictates in the field-of-view (FOV) of the image obtained, and the further from the centre of k-space signal is sampled, the better the resolution of the image reconstructed.

The phase-encoding gradient strength and duration are determined by the desired image resolution, and the field-of-view (FOV) determines the extent of the object being imaged. The relationship between k-space and image space is given by the Fourier transform:

$$F(k_x, k_y) = \iint f(x,y) e^{-2\pi i(k_x x + k_y y)} dx dy \qquad [2.26]$$

where $F(k_x, k_y)$ is the Fourier transform of the image function $f(x,y)$ in k-space, k_x and k_y are the spatial frequency coordinates in k-space, and x and y are the spatial coordinates in image space.

2.5.5 IMAGING SEQUENCES

The contrast of the image obtained during an MRI sequence depends on the intrinsic properties of the tissue being imaged, including proton density, T_1 (longitudinal relaxation time), T_2 (transverse relaxation time), diffusion, and flow sensitivity. However, the way in which the sequence is designed will also determine the dominant contrast.

There are many different techniques used for imaging, and the sequence chosen will depend on several factors, including the region of interest, the desired contrast, and the spatial and

temporal resolution required. The choice of sequence also impacts the acquisition time and the quality of the final image.

Some of the main sequences used in MRI, especially those used in this thesis, include:

1. Spin echo (SE): This is a basic sequence that is commonly used for anatomical imaging. It relies on the creation of a spin echo by using two radiofrequency pulses 90^0 and 180^0 separated by a time delay. The contrast in the resulting image is dominated by T_1 and T_2 relaxation.

2. Gradient echo (GRE): This sequence uses a gradient to cause the spins to dephase and rephase, creating a gradient echo. The contrast in the resulting image is dominated by T_2* relaxation.

3. Inversion recovery (IR): This sequence involves the inversion of the longitudinal magnetization, which is then allowed to recover before the signal is read out. The contrast in the resulting image is dominated by T_1 relaxation time.

4. Magnetic resonance angiography (MRA): This sequence is used to visualize blood vessels and blood flow, typically by using a contrast agent to enhance the signal from the vessels.

The choice of imaging sequence is important in obtaining high-quality images with the desired contrast and resolution. Researchers and clinicians must carefully select the most appropriate sequence for their specific application. Here we discuss the main sequences used in this experimental work.

2.5.5.1 T_1 WEIGHTED (T_1W) IMAGING

T_1 weighted images are commonly used for anatomical imaging of the brain (also used in the whole of the experimental work of this thesis for the segmentation of the hippocampus) as they provide good contrast between grey matter, white matter, and cerebrospinal fluid (CSF). The

image contrast in T_1 weighted imaging depends on the longitudinal relaxation time (T_1) of different tissues. T_1 weighted imaging is generally characterized by short TR (repetition time) and short TE (echo time). One of the most common T_1-weighted sequences used in chapter three of this work is the magnetization-prepared rapid-acquisition gradient echo (MPRAGE) sequence.

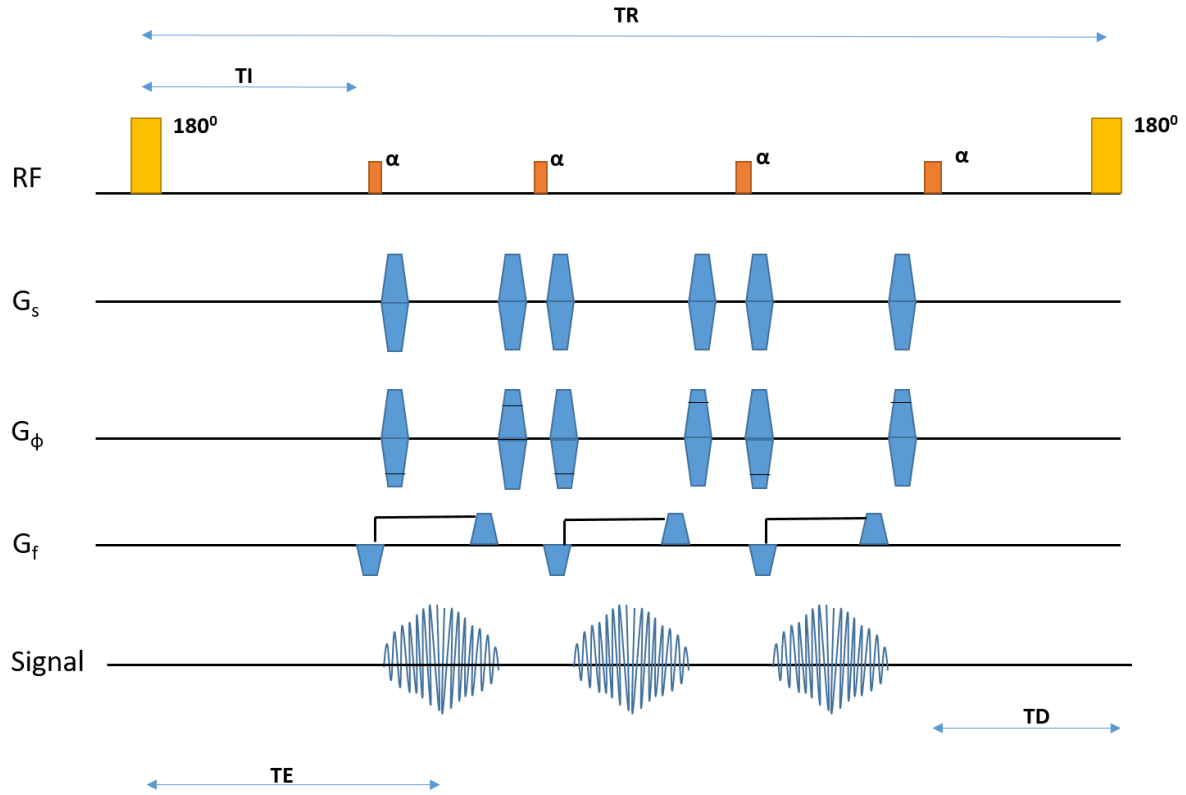


Figure 2.8: A schematic representation of an MPRAGE imaging sequence with spoiler gradrient

The MPRAGE sequence uses a 180° inversion pulse to invert the magnetization of the object, aiding the inversion of the magnetization from the positive to the negative z-direction. The magnetization recovers differently for different tissues, allowing the acquisition of a set of k-space lines after a specific inversion time (TI). These acquisitions are repeated until the full set of k-space data has been acquired, and a T_1-weighted image can then be formed. The MPRAGE sequence provides high-resolution images with excellent contrast between grey matter, white matter, and CSF.

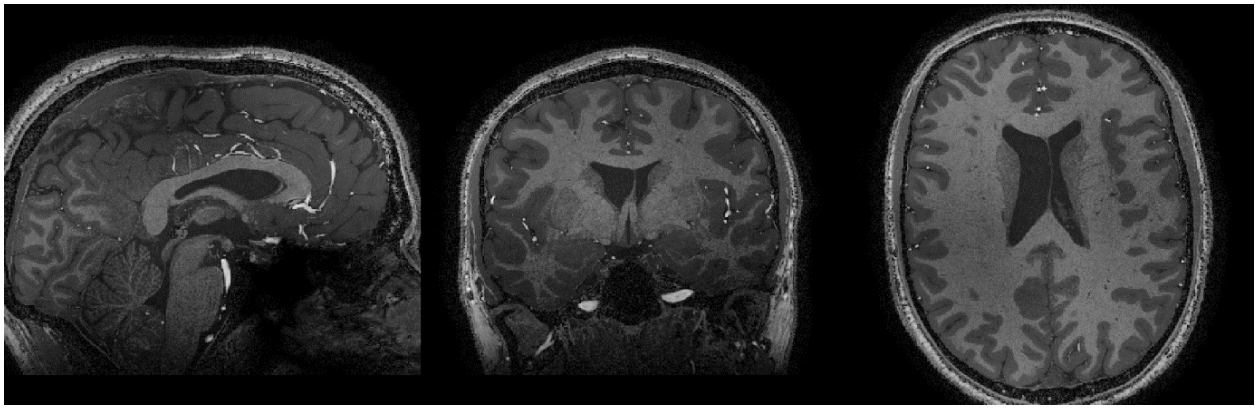


Figure 2. 9: T_1 weighted image in Sagittal, coronal and Axial views

Sometimes, contrast agents (usually gadolinium-based) are administered to improve the contrast of T_1 weighted images. Also, fat suppression is often performed in T_1 weighted sequences to suppress the bright signal from fat. T_1 weighted images can be viewed in the sagittal, coronal, and axial planes, as shown in Fig 2.10.

In the T_1 weighted image shown above,

- The grey matter appears gray
- The white matter appears bright
- The CSF appears black

T_1 weighted images are an essential part of clinical MRI protocols, providing important information about the brain's structure and function.

2.5.5.2 T_2 WEIGHTED IMAGING

Another very common scan used in this thesis is the T_2 weighted scan. This sequences are important in the detection of disease since many diseased tissues have high T_2. When obtaining a T_2 weighted scan, a spin echo sequence with a long TR is used to avoid the influence of T_1 contrast by minimizing the T_1 recovery difference, and a long echo time (TE) to amplify the T_2 decay difference. This sequence is less influenced by the inhomogeneities in the magnetic field, which highlight the effect of T_2*.

For this research work, the Fast Spin Echo/Turbo Spin Echo (FSE/TSE) sequence was used to acquire the image shown in Fig 2.12. In this sequence, the echo train and filling of other k-space lines are achieved in time intervals after the first echo. By doing so, k-space is filled up faster due to the reduced repetition time (TR), and the acquisition time is reduced.

This is done by applying a series of 180^0 pulses to produce an echo train. After each echo, the phase-encoding is cancelled, and a different phase-encoding is applied to the following echo.

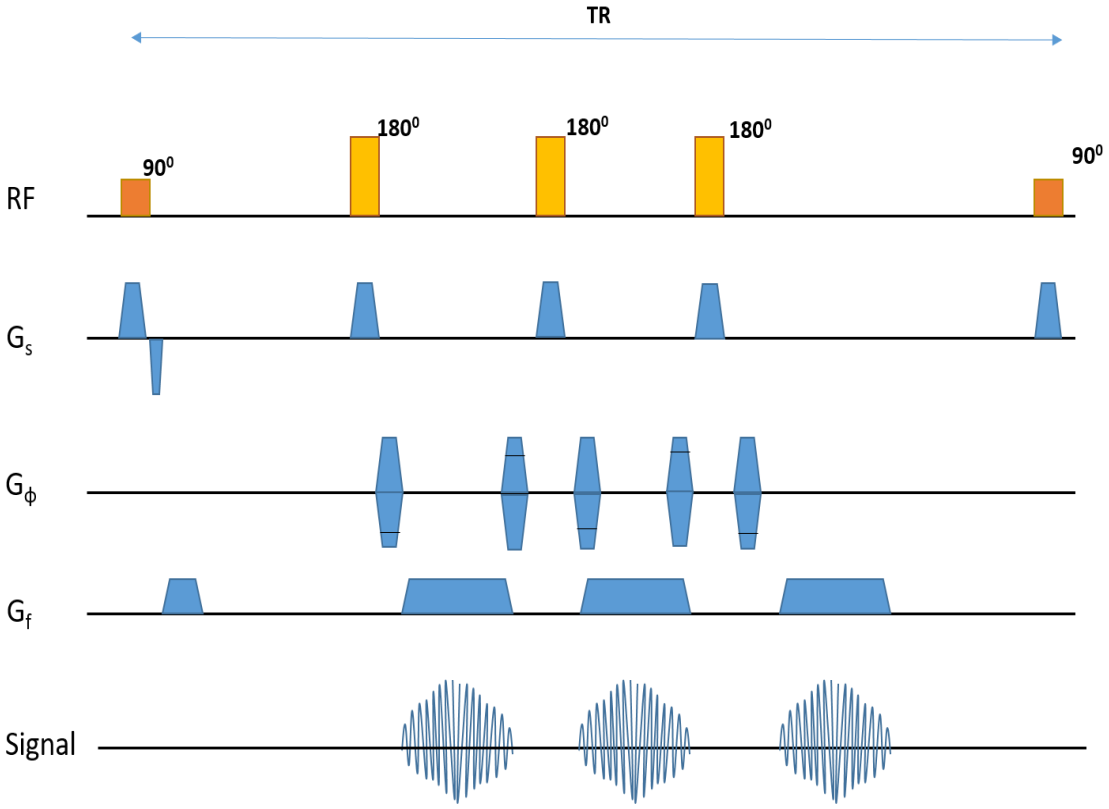


Figure 2. 10: shows a schematic representation of the Fast Spin Echo/Turbo Spin Echo (FSE/TSE) sequence.

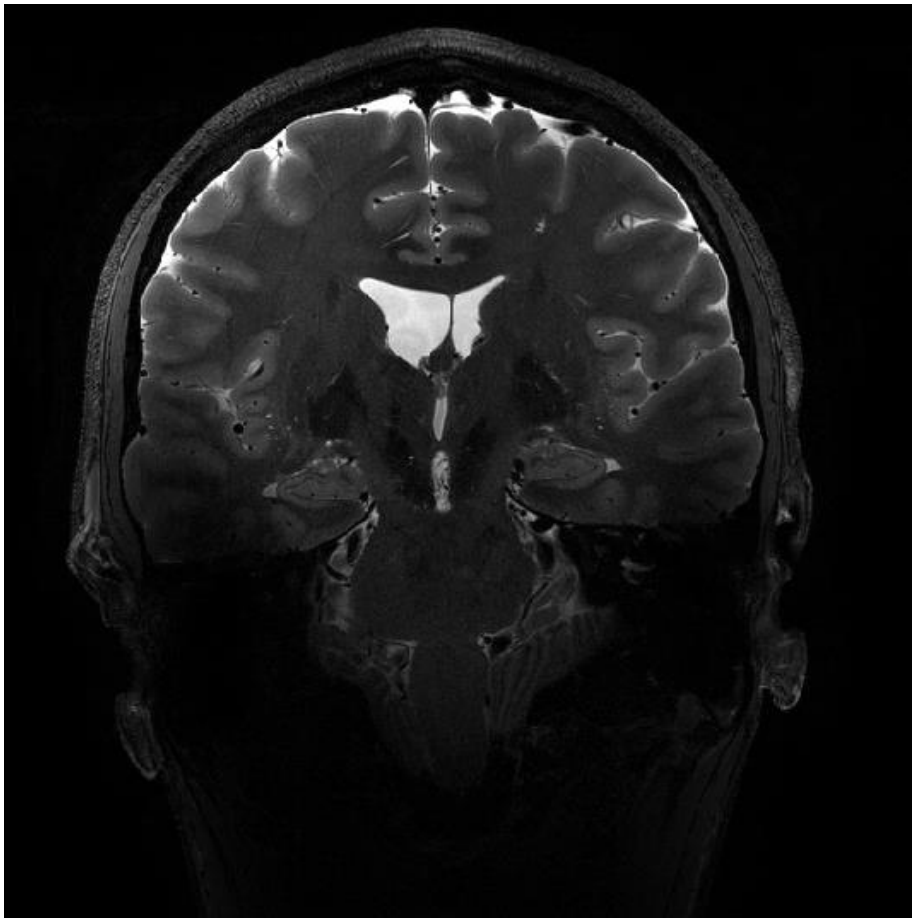


Figure 2.11: shows a T_2 weighted image obtained using the FSE/TSE sequence

In T_2 weighted images, the intensity of different tissues is as follows:

- The grey matter appears gray in color (intermediate signal intensity).
- The white matter appears dark (hypo intensity).
- The CSF appears bright (hyper intensity).

Chemical fat saturation or STIR can be used to suppress the signal from fat to allow fluids, which are of high intensity, to stand out in the image.

2.5.5.2.1 FLAIR (FLuid Attenuated Inversion Recovery)

FLAIR produces T_2 weighted images in which the signal from fluids with long T_1 values, such as CSF, has been suppressed. They are most used in this research for clinical analysis, especially for the detection/identification of white matter hyperintensities.

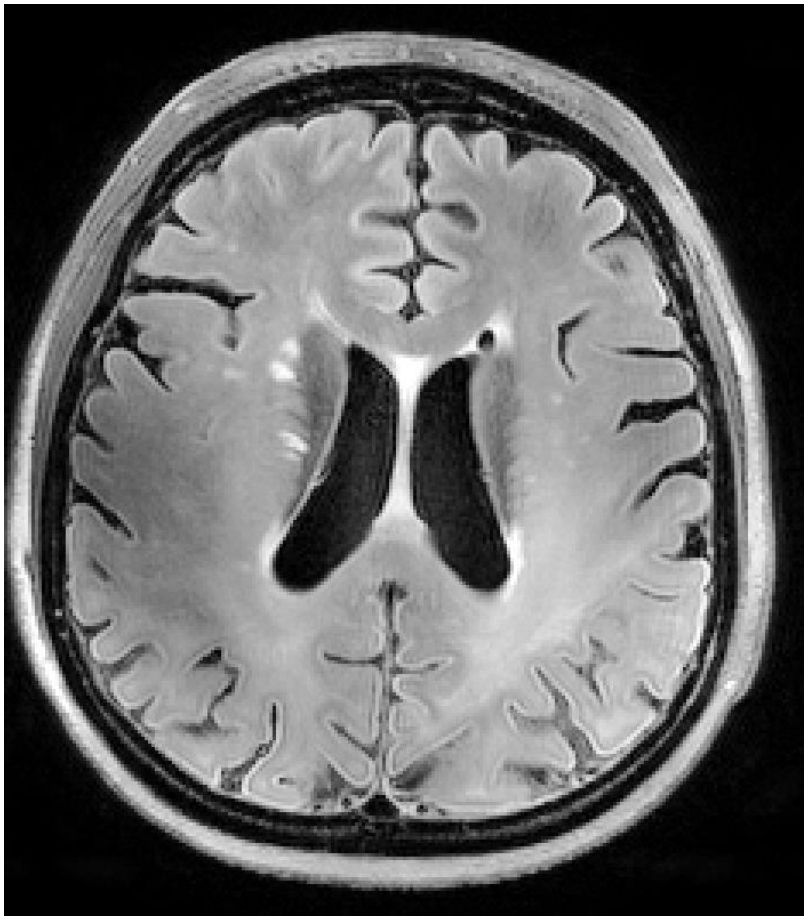


Figure 2.12: FLAIR image

FLAIR uses both T_1 and T_2 weighted imaging to suppress the CSF signal but give good contrast between grey and white matter. The elimination of the CSF in FLAIR images helps to reveal lesions such as cerebral cortical lesions that are in close proximity to CSF (Bakshi et al., 2001). CSF is made to appear dark in FLAIR images by using an inversion recovery sequence in which the inversion time (TI) is chosen to null the CSF signal.

$$TI = \ln(2) \cdot T_1 \qquad [2.27]$$

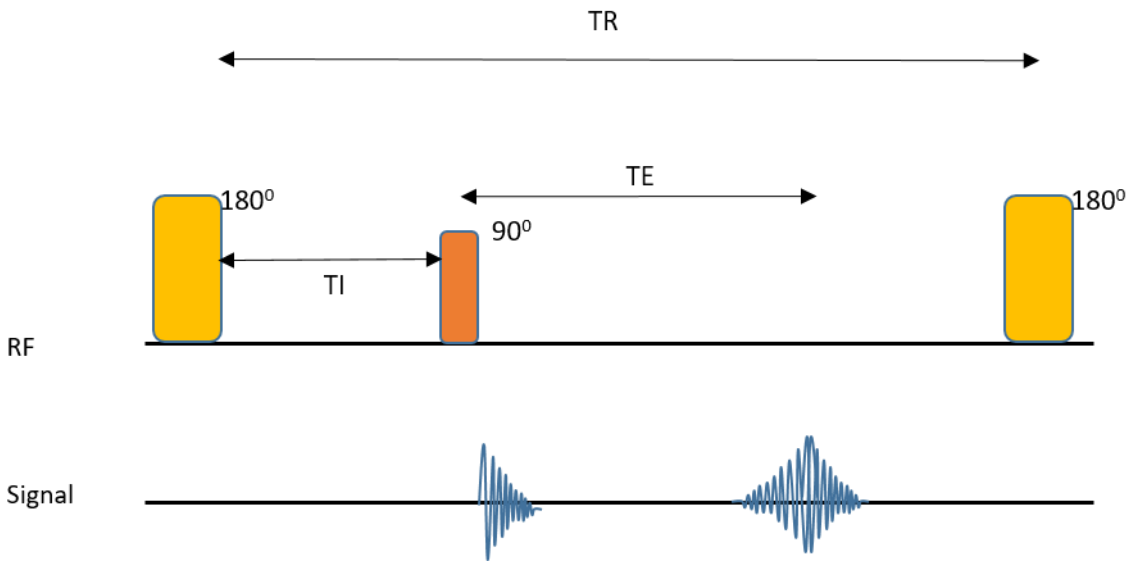


Figure 2.13: The FLAIR sequence

By applying the readout pulse (90^0) at exactly the point in time when the longitudinal magnetization of the CSF reaches the null point, the signal from the CSF is suppressed.

2.5.5.2.2 T_2*-WEIGHTED (GRADIENT ECHO) SEQUENCES

Gradient echo images are naturally T_2* weighted and the signal magnitude at echo time TE varies as $e^{-\frac{TE}{T_2^*}}$. T_2* weighted images appear dark in regions where the magnetic field varies rapidly with spatial position. This makes such images sensitive to regions where the magnetic susceptibility is different from the surrounding tissue (e.g. due to the presence of venous blood vessels or due to small bleeds). The phase of gradient echo images is also sensitive to the variation of magnetic susceptibility across tissues and forms the basis of Quantitative Susceptibility Mapping (QSM) is discussed in detail in Chapter 4).

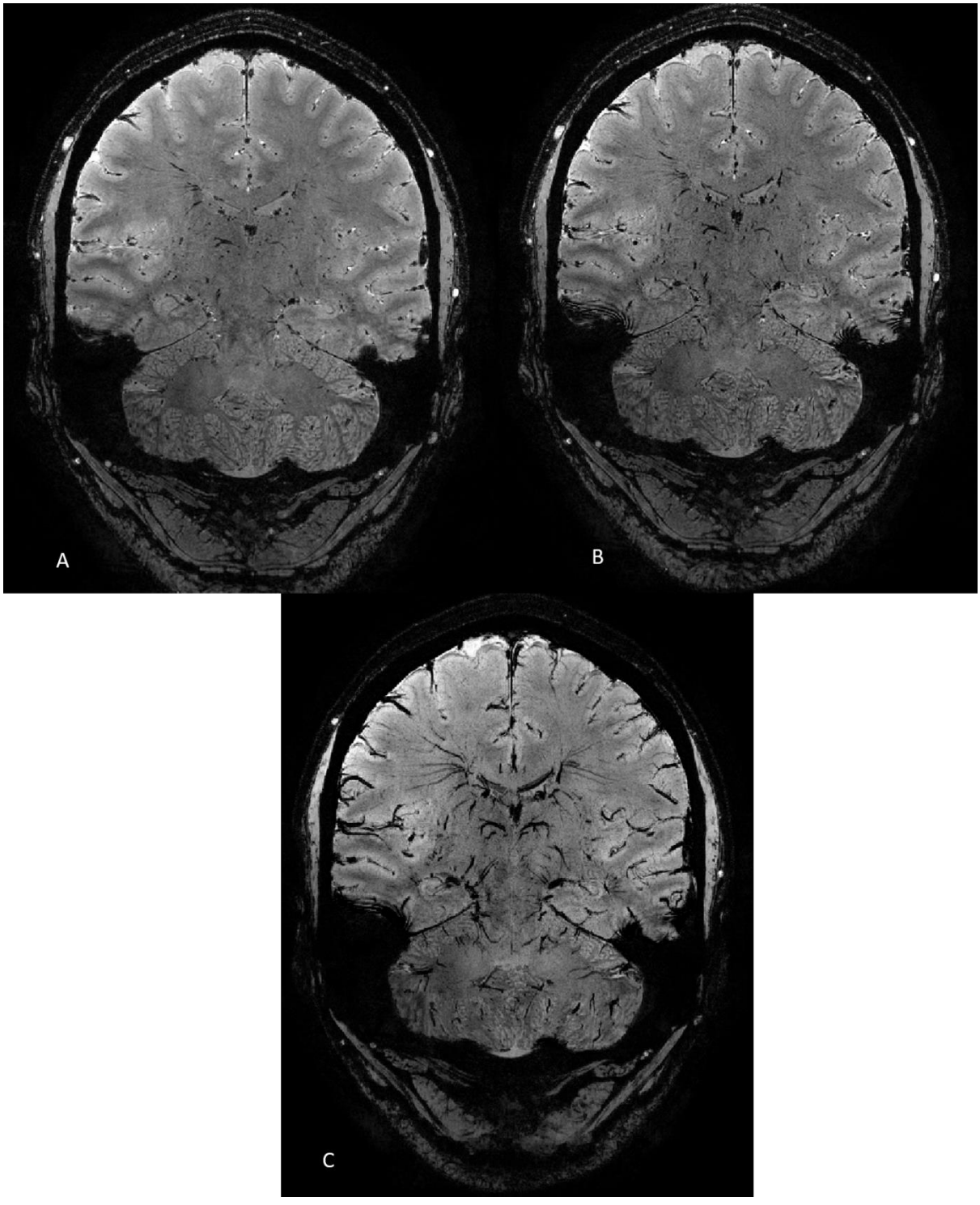


Figure 2.14: A) showing a T_2 (Gradient Echo) image, B) showing SWI (Susceptibility Weighted image) and C) the minimum intensity projection of the SWI*

The gradient echo images shown in Fig. 2.15 were acquired with a quite short echo time of 20ms and uses quite a long TR to avoid the influence of T_1 contrast.

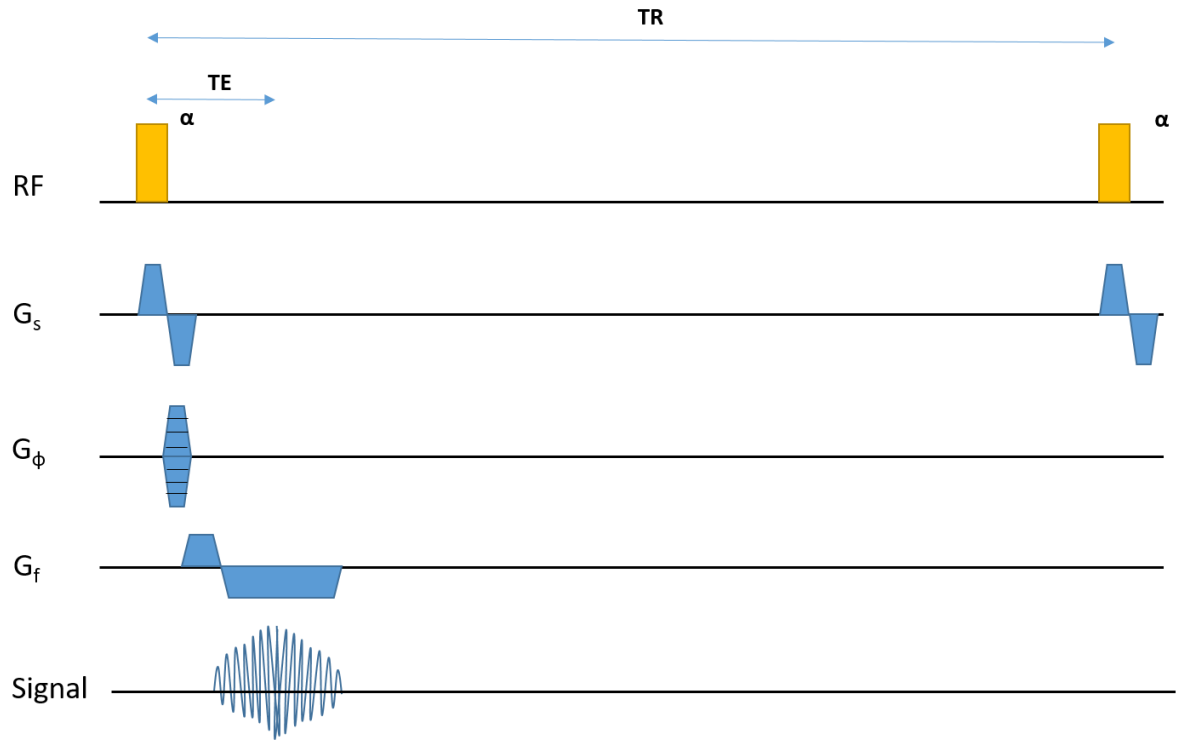


Figure 2.15: The GRE sequence

In general the T_2* weighted imaging sequence works like that of the normal T_2-weighted sequence but were T_2-weighting uses the 180^0 refocusing pulse to get rid of the effect of fields inhomogeneity, T_2* weighted imaging does not use 180^0 refocusing pulses on pulses but to reserves the field gradient to generate gradient echo.(Tang et al., 2014). T_2* transverse decay which arises as a result of the combination of the T_2 effect and the inhomogeneity of the main magnetic field. The T_2* can be represented by

$$\frac{1}{T2^*} = \frac{1}{T2} + \gamma \cdot \Delta B_{inhom} \qquad [2.28]$$

Where γ is the gyromagnetic ratio and ΔB_{inhom} describes the variation in the magnetic field over the voxel.

2.5.5.3 FLOW SENSITIVE SEQUENCES

Flow-sensitive MRI sequences are highly valuable for investigating the flow dynamics of fluids like blood in vivo. Time of flight (TOF) is one of the most commonly used flow-sensitive

techniques in MRI, which exploits the inflow of blood into the selected area or slice being measured to produce contrast between the stationary tissue and the flowing blood. We utilise this sequence in the work described in Chapter 5.

TOF imaging utilizes the difference in magnetization between moving and stationary spins. The magnetization of moving spins is larger than that of the stationary spins, resulting in a bright signal from the flowing blood compared to the surrounding stationary tissues. This effect is achieved by applying repeated excitation pulses, which saturate the stationary spins and expose the inflowing blood spins to a minimal number of excitation pulses.

To optimize the TOF image quality, the thickness of the imaging slab, and the repetition time (TR) should be carefully chosen taking into consideration the velocity of the blood flow. A thin slab perpendicular to the direction of the inflowing blood, with a short TR, ensures that the blood remains unsaturated during imaging, producing a maximum signal throughout the acquisition while minimizing the number of excitation pulses.

Even small changes in slice thickness can significantly impact the performance of TOF imaging.

In brain imaging, SWI (susceptibility-weighted imaging) is commonly used to study veins in the brain, while MRA (Magnetic Resonance Angiography) is used to study the arteries of the brain. SWI is discussed in more detail in Chapter 5 (see Fig 2.15 above).

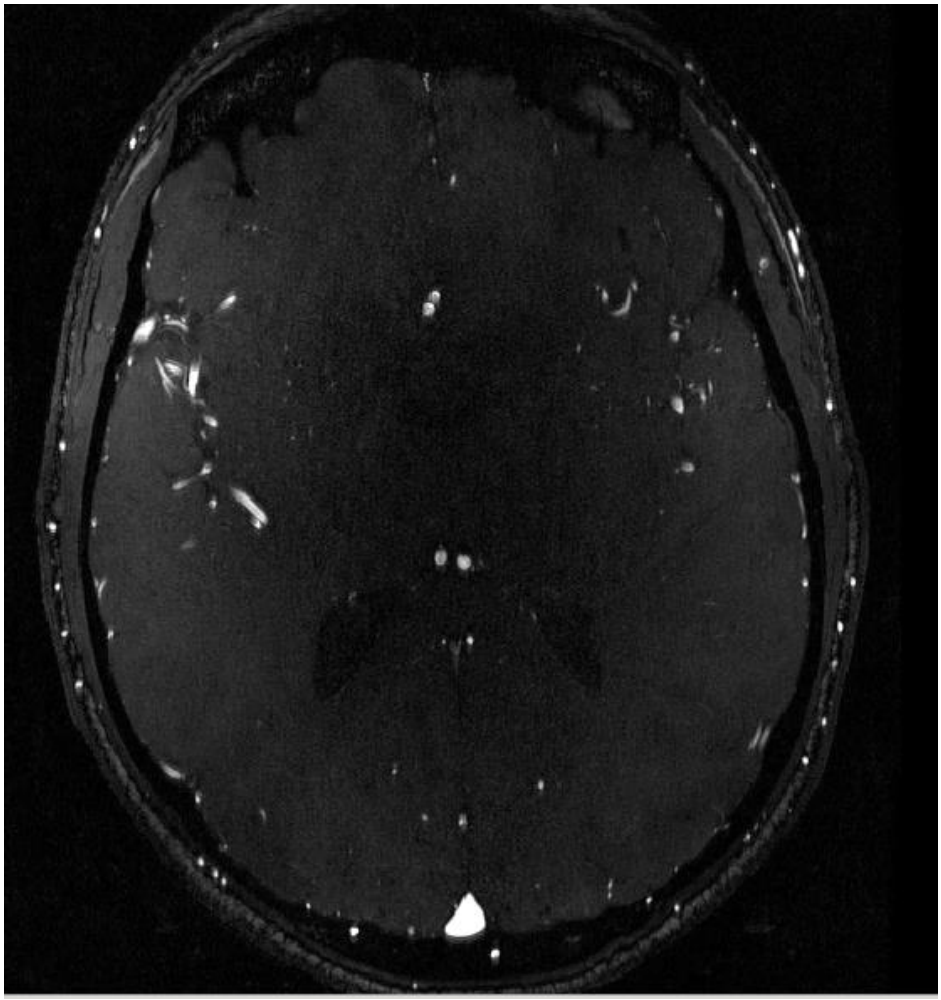


Figure 2.16: shows an example of TOF image with 0.38 mm isotropic resolution 7:23min acquisition time, TR= 14 TE= 4.5 FA=22 multi-chunk with 4 chunks each of thickness 8.36 mm.

2.5.5.4 EFFECT OF HIGHER FIELD

The use of higher field strengths, such as 7T MRI, for Time-of-Flight (TOF) scans can have several effects on the imaging process and the resulting images. Here are the effects of higher field 7T on TOF scans:

1. Improved Signal-to-Noise Ratio (SNR): One of the primary advantages of using 7T MRI is the increased SNR (Van Der Kolk et al., 2013). Higher SNR allows for better visualization of blood vessels and improved image quality. This enhancement is particularly beneficial for small vessels and fine vascular details, which may be challenging to visualize at lower field strengths.

2. Enhanced Spatial Resolution: 7T MRI provides higher spatial resolution compared to lower field strengths. The increased spatial resolution allows for better delineation of blood vessel boundaries and more accurate characterization of vascular pathologies and abnormalities.
3. Improved Vascular Contrast: Higher field strengths at 7T can enhance the vascular contrast in TOF scans (Kang et al., 2010). This enhancement allows for better differentiation between blood vessels and surrounding tissues, leading to improved image quality and more accurate diagnosis of vascular conditions.
4. Reduced Scan Time: With the increased SNR and sensitivity at 7T, TOF scans can be performed with shorter acquisition times while maintaining image quality (Vaughan et al., 2001). Reduced scan time is beneficial for both patient comfort and reducing motion artefacts during image acquisition.
5. Enhanced Visualization of Small Vessels: The improved spatial resolution and SNR at 7T allow for better visualization of small vessels and microvasculature (Heverhagen et al., 2008, Kang et al., 2009). This capability is valuable for studying cerebral perfusion and microcirculation in various neurological conditions.

2.6 MRI SAFETY

Ensuring MRI safety is of paramount importance throughout the entire scanning process, encompassing pre-scan preparations, the scanning procedure itself, and post-scan activities. Despite its effectiveness as a diagnostic tool, MRI employs powerful magnetic fields and radiofrequency energy, which necessitates diligent attention to potential hazards for both patients and operators. Consequently, the implementation of rigorous safety protocols is imperative to mitigate any potential risks inherent to MRI scans. This section describes the various hazards linked to MRI scanning, particularly focusing on the unique considerations

pertinent to 7T MRI systems, and also mentioms the strategies available to effectively manage and mitigate these risks.

2.6.1 PROJECTILE EFFECT

One of the primary risks associated with MRI is the Projectile Effect, which refers to the potential danger of ferromagnetic objects or materials becoming projectiles when exposed to the strong magnetic field of the scanner. MRI systems generate powerful magnetic fields, and any ferromagnetic object close to the scanner can be drawn towards the magnetic field with considerable force.

The severity of the Projectile Effect is directly linked to the strength of the static magnetic field (B_0) and the mass of the ferromagnetic object, while inversely related to the cube of the distance from the magnet (Panych & Madore, 2018, Tsai et al., 2015). This effect becomes more pronounced at higher field strengths, such as 7T, where the magnetic field is stronger. Consequently, even small ferromagnetic objects can rapidly and forcefully move towards the scanner, posing serious risks to patients, staff, and individuals nearby. These risks can lead to severe injuries if adequate safety measures are not observed.

To ensure safety, it is imperative to thoroughly screen all personnel and participants for any ferromagnetic materials before they enter the scanner room. This screening process may include a comprehensive questionnaire, physical examination, and the use of metal detectors. Moreover, it is essential to establish well-defined protocols for handling ferromagnetic objects and materials within the MRI facility. Proper training in MRI safety procedures for all staff members is vital to prevent incidents related to the Projectile Effect.

By strictly adhering to these precautions, the potential risks associated with the Projectile Effect can be significantly reduced, enhancing the safety of both patients and personnel involved in MRI procedures.

2.6.2 VERTIGO

Vertigo refers to a sensation of spinning or dizziness, often described as a feeling that you or your surroundings are moving when they are not (Glover et al., 2007). In the context of a 7T MRI scanner, vertigo can potentially occur due to various factors associated with the strong magnetic field and the scanning environment.

The main factors contributing to vertigo in a 7T MRI scanner are:

Magnetic Field Strength: The higher magnetic field strength of a 7T MRI scanner can interact with the inner ear's balance organs, which are responsible for detecting head movement and orientation. This interaction might lead to a sensation of vertigo in some individuals.

Gradients and Motion: The rapid switching of gradients during the scan can induce small movements or vibrations in the body, which might affect the inner ear and trigger vertigo-like symptoms.

Constricted Space: MRI scanners, including those with higher field strengths, typically have a confined space where the patient lies during the scan. Some individuals might experience claustrophobia or anxiety due to the tight space, which can lead to sensations of vertigo or dizziness.

Noise: The intense acoustic noise produced by the MRI scanner, especially at higher field strengths, can be unsettling for some individuals and contribute to a feeling of vertigo or discomfort.

Individual Sensitivity: People vary in their sensitivity to magnetic fields, motion, and the MRI environment. Some individuals may be more prone to experiencing vertigo than others.

It's important to note that not everyone will experience vertigo in a 7T MRI scanner, and many individuals can tolerate the scanning procedure without any issues. However, for those who are concerned about potential vertigo or discomfort, it's advisable to communicate these

concerns with the medical staff before the scan. They can provide guidance, offer reassurance, and take appropriate measures to ensure a safe and comfortable scanning experience

2.6.3 SAR (Specific Absorption Rate)

During MRI scanning, the amount of energy that is absorbed by the participant's body is measured in watts per kilogram (W/kg), which is known as the Specific Absorption Rate (SAR). One of the risks associated with RF power deposition is the potential for heating of the body tissues, which can cause burns or other health complications (Lancaster, 2011, Isbrucker et al., 2006). The 7T MRI systems offer unparalleled imaging capabilities, enabling enhanced spatial resolution and increased sensitivity to subtle anatomical and functional changes. However, these benefits come with the trade-off of increased SAR levels. The design of MRI pulse sequences significantly impacts SAR. Complex and advanced imaging sequences may lead to higher SAR levels. To prevent these risks, SAR limits have been established by the International Commission on Non-Ionizing Radiation Protection (ICNIRP) in 2004. The SAR limit for normal clinical procedures should not result in more than a $1^{o}C$ rise in temperature for the whole body, which is equivalent to about 2 W/kg. For other procedures, the SAR limit is set at 4 W/kg.

To ensure patient safety during scanning especially at 7T, it is crucial to strike a balance between the desire for detailed images and SAR considerations when developing imaging protocols. This involves carefully managing the trade-off between exploiting the advantages of higher field strengths and ensuring patient well-being. Additionally, patients should undergo thorough screening to assess any potential increased risk for SAR-related health complications.

2.6.4 THERMAL INJURY

Although rare, thermal injury from MR imaging can occur and should not be ignored. Between 2000 and 2010 in the United States, 419 cases of thermal injury were reported (Tsai et al., 2015). Burns from MR imaging can be severe, life-threatening, and difficult to predict.

Most RF burns in MR imaging occur due to contact with extraneous electrical conductors, such as metal implants, ECG leads, and RF coil leads. Close contact with the RF coils and conduction loops set up through the skin, such as allowing skin of the shins or thighs to touch, can also result in RF burns (Tsai et al., 2015). Therefore, it is essential to take extra care to avoid excess contact with electrical conductors in the scanner.

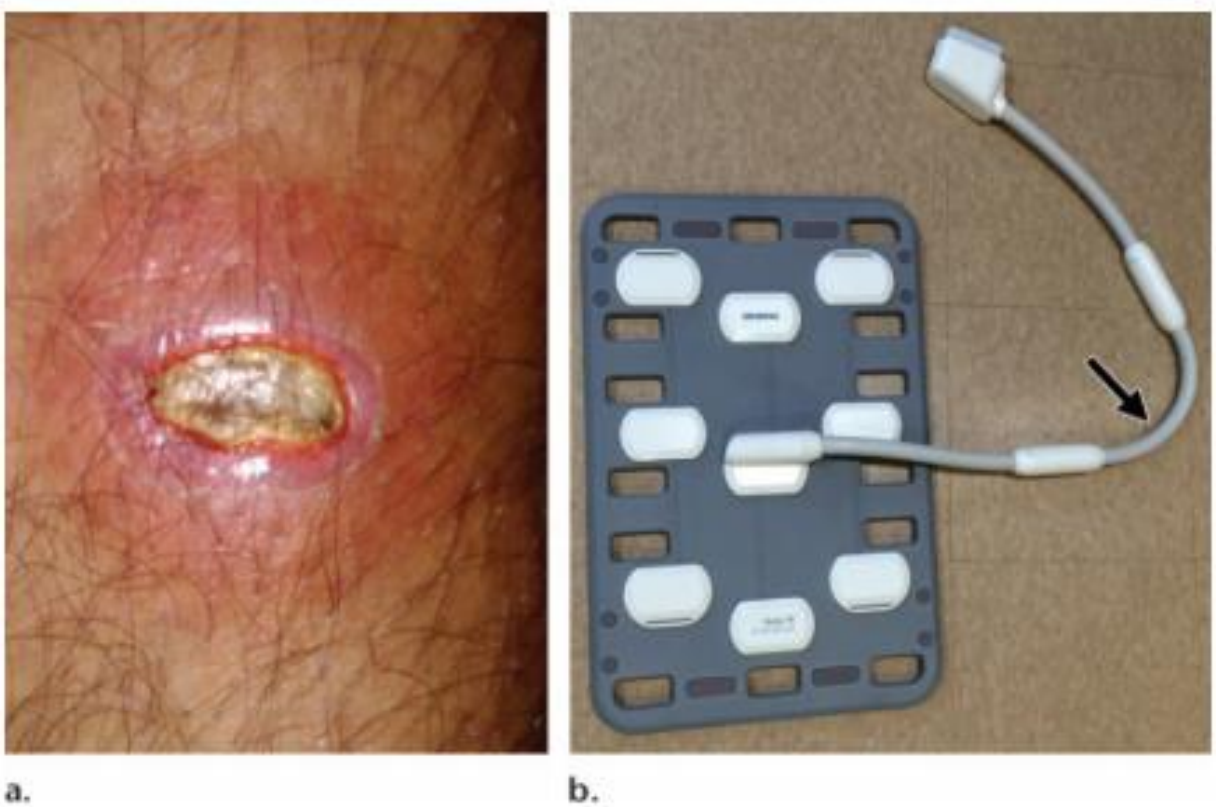


Figure 2.17: Direct contact burn (a) Photograph shows a third-degree burn on a patient's calf, which was pressed against the cable of the radiofrequency coil. (b) Photograph shows a phased array coil similar to the one involved in the incident. The coil cable showed no indication of a burn. The arrow indicates the approximate contact point (Tsai et al., 2015).

2.6.5 ACOUSTIC NOISE

Magnetic Resonance Imaging (MRI) generates a considerable amount of unwanted acoustic noise emanating from the gradient system. The rapid fluctuations in current within the gradient coils, occurring in the presence of a magnetic field, induce movement in the gradient coils themselves, thereby producing noise (McJury, 2022).

The intensity of scanner noise tends to be heightened at higher field strengths, such as 7T, when compared to lower field scanners. This heightened noise level is predominantly attributed to the stronger magnetic fields associated with higher field strengths, leading to increased vibrations and motion within the scanner's components. These vibrations and movements significantly contribute to the noise generation, a phenomenon accentuated at higher field strengths. Furthermore, the interaction between the magnetic field and the electrical currents utilized during the imaging process can also contribute to the overall noise output. Consequently, individuals, including patients and researchers, working with 7T scanners may encounter more pronounced and potentially disruptive scanner noise compared to those using lower field scanners.

To further elaborate, the acoustic noise generated during an MRI scan can be as loud as a rock concert, with levels ranging from 80 to 130 decibels (dB) (McJury, 2022). Exposure to this level of noise can lead to hearing damage or loss, as well as increased stress and anxiety for both patients and healthcare workers. Therefore, it is important to take measures to reduce the level of noise exposure during MRI scanning.

In addition to providing ear protection for patients, efforts to reduce the noise generated by MRI machines include using special gradient coils with lower acoustic noise levels, and implementing soundproofing measures in the scanning room. Researchers are also exploring alternative techniques such as silent MRI, which uses different imaging methods that produce little to no noise (Ljungberg et al., 2021). By addressing the issue of acoustic noise, we can improve the safety and comfort of MRI scanning for both patients and healthcare workers.

This is one of great challenges face by MR scientist and pose minimal risk, but great care should be taken in reducing the exposure of staff and participant to safe limit of acoustic noise. This is achieved by providing participant with ear protection (like ear plugs and pads) and limiting mechanical coupling to the bed with pads.

2.7 STUDYING THE BRAIN WITH 7T MRI: SUSCEPTIBILITY STUDIES AND HIPPOCAMPAL SEGMENTATION

Magnetic Resonance Imaging (MRI) has revolutionized our understanding of the human brain, enabling non-invasive visualization and analysis of its intricate structures and functions. As technology advances, higher magnetic field strengths have become available, offering researchers the opportunity to delve deeper into the brain's mysteries. Among these advancements, 7 Tesla (7T) MRI has emerged as a cutting-edge tool for investigating brain susceptibility and hippocampal segmentation with unprecedented detail and sensitivity. In this section, we explore the reasons why we opted for 7T MRI over traditional 3 Tesla (3T) systems for exploring brain susceptibility and segmenting the hippocampus.

3T MRI has been extensively used for susceptibility-based imaging and research in the brain (Lin et al., 2015, Yoo et al., 2020, Nair et al., 2010). It has provided valuable insights into the brain's microstructure, iron content, and various pathological processes. However, 7T MRI shows better prospects for brain susceptibility and segmentation of brain structure (Spincemaille et al., 2020) research due to several key advantages which largely arise from the increase in NMR sensitivity with field strength:

1. Improved Signal-to-Noise Ratio (SNR): Higher SNR can be used to provide better image quality and enhanced sensitivity to variations in tissue contrast. Segmentation and Neurodegeneration Studies: 7T MRI's improved contrast and resolution have proven particularly advantageous for hippocampal segmentation (Wisse et al., 2014), allowing the delineation of hippocampal subfields with higher precision. This capability is crucial for investigating neurodegenerative diseases like Alzheimer's, where hippocampal subfield changes are associated with disease progression. Similarly certain brain nuclei are relatively small and challenging to study with lower field strengths. 7T MRI enhances the visibility of these nuclei, enabling in-depth investigation of their functions and connections within the brain.

2. Enhanced Spatial Resolution is made possible by the increase in available SNR (which scales with the inverse of the volume of the voxel). This is especially important for visualizing fine anatomical details in the brain, and for precise mapping of susceptibility variations within small regions of interest. Various brain pathologies, such as multiple sclerosis (Kister et al., 2016) and traumatic brain injury (Sun & Jiang, 2008), are associated with susceptibility changes. 7T MRI's higher sensitivity enables more accurate detection and characterization of these changes, potentially leading to improved diagnosis and treatment monitoring.
3. Enhanced Tissue Contrast: Magnetic susceptibility contrast increases directly with magnetic field strength, as tissue magnetism effects including susceptibility and chemical shift induced by the main field are proportional to B_0 (Wang Y., 2012): .

$$B = \mu_0(H + M) = \mu_0(1 + \chi_v)H \qquad [2.29]$$

where B is the magnetic induction, μ_0 is the vacuum permeability, H is the magnetic field strength, M is the magnetization and χ_v is the volume magnetic susceptibility.

This is crucial for studying small structures, such as hippocampal subfields, and detecting susceptibility changes related to neurodegenerative diseases or brain lesions.
4. Quantitative Susceptibility Mapping (QSM) Accuracy: QSM is a powerful technique providing valuable information about brain iron, myelin, and other microstructural properties (Zhou et al., 2014, Lambrecht et al., 2020). However the processing required to create a QSM map from an image demonstrating susceptibility effects requires post processing which is affected by low SNR. 7T MRI's higher SNR and spatial resolution contribute to more accurate and precise QSM allowing better differentiation of brain tissues.

While 7T MRI offers significant advantages for brain susceptibility research, there are also challenges and considerations related to safety, hardware, and image artefacts that need to be

addressed when working with higher magnetic fields. As technology advances and more experience is gained with 7T MRI, it is likely to become an increasingly valuable tool in neuroscience research, providing deeper insights into brain structure and function, and contributing to advancements in clinical care.

2.8 REFERENCES

Bakshi, R., Ariyaratana, S., Benedict, R. H. B., & Jacobs, L. (2001). Fluid-attenuated inversion recovery magnetic resonance imaging detects cortical and juxtacortical multiple sclerosis lesions. *Archives of Neurology*, *58*(5), 742–748. https://doi.org/10.1001/archneur.58.5.742

Bloch, F., Hansen, W. W., & Packard, M. (1946). The Nuclear Induction Experiment. *Pysical Review*, *70*(5).

Bloembergen, N., Purcell, E. M., & Pound, R. V. (1948). Relaxation effects in nuclear magnetic resonance absorption. *Physical Review*, *73*(7), 679–712. https://doi.org/10.1103/PhysRev.73.679

Caused, M. C. (2018). Quantitative MRI of the Brain. *Quantitative MRI of the Brain*. https://doi.org/10.1201/b21837

Ernst, R. R., Bodenhausen, G., & Wokaun, A. (1987). PRINCIPLES OF NUCLEAR MAGNETIC RESONANCE IN ONE AND TWO DIMENSIONS. *Oxford University Press*, *29*(3), 57–64. https://doi.org/10.3828/mc.29.3.57

Giunta, C. J., & Mainz, V. V. (2020). Discovery of Nuclear Magnetic Resonance: Rabi, Purcell, and Bloch [Chapter]. *ACS Symposium Series*, *1349*, 3–20. https://doi.org/10.1021/bk-2020-1349.ch001

Glover, P. M., Cavin, I., Qian, W., Bowtell, R., & Gowland, P. A. (2007). Magnetic-field-induced vertigo: A theoretical and experimental investigation. *Bioelectromagnetics*, *28*(5), 349–361. https://doi.org/10.1002/bem.20316

Harlow, J., & Pitre, J. (2014). *NMR*. 1–13.

Heverhagen, J. T., Bourekas, E., Sammet, S., Knopp, M. V., & Schmalbrock, P. (2008). Time-of-flight magnetic resonance angiography at 7 tesla. *Investigative Radiology*, *43*(8), 568–573. https://doi.org/10.1097/RLI.0b013e31817e9b2c

Holger Försterling, F. (2009). Spin dynamics: Basics of Nuclear Magnetic Resonance, Second Edition . *Medical Physics*, *37*(1), 406–407. https://doi.org/10.1118/1.3273534

Isbrucker, R. A., Edwards, J. A., Wolz, E., Davidovich, A., & Bausch, J. (2006). Safety studies on epigallocatechin gallate (EGCG) preparations. Part 3: Teratogenicity and reproductive toxicity studies in rats. *Food and Chemical Toxicology*, *44*(5), 651–661. https://doi.org/10.1016/j.fct.2005.11.002

Jung, B. A., & Weigel, M. (2013). Spin echo magnetic resonance imaging. *Journal of Magnetic Resonance Imaging*, *37*(4), 805–817. https://doi.org/10.1002/jmri.24068

Kang, C. K., Park, C. A., Kim, K. N., Hong, S. M., Park, C. W., Kim, Y. B., & Cho, Z. H. (2010). Non-invasive visualization of basilar artery perforators with 7T MR angiography. *Journal of Magnetic Resonance Imaging*, *32*(3), 544–550. https://doi.org/10.1002/jmri.22250

Kang, C. K., Park, C. A., Lee, H., Kim, S. H., Park, C. W., Kim, Y. B., & Cho, Z. H. (2009). Hypertension correlates with lenticulostriate arteries visualized by 7T magnetic resonance angiography. *Hypertension*, *54*(5), 1050–1056. https://doi.org/10.1161/HYPERTENSIONAHA.109.140350

Kister, I., Chawla, S., Wuerfel, J. T., Sinnecker, T., & Paulm, F. (2016). Longitudinal study of MS lesions using multi-parametric ultra-high field (7Tesla) MRI. *Multiple Sclerosis*, *22*(Supplement 3), 240.

Lambrecht, V., Hanspach, J., Hoffmann, A., Seyler, L., Mennecke, A., Straub, S., Marxreiter, F., Bäuerle, T., Laun, F. B., & Winkler, J. (2020). Quantitative susceptibility mapping depicts severe myelin deficit and iron deposition in a transgenic model of multiple system atrophy. *Experimental Neurology*, *329*. https://doi.org/10.1016/j.expneurol.2020.113314

Lancaster, P. A. L. (2011). Causes of birth defects: Lessons from history. *Congenital Anomalies*, *51*(1), 2–5. https://doi.org/10.1111/j.1741-4520.2010.00311.x

Lauterbur, P. . (1973). © 1973 Nature Publishing Group. *Nat. Phys. Sci.*, *22*, 190–191. https://www.nature.com/articles/242190a0

Lauzon, M. (2020). *A Beginner's Guide to Bloch Equation Simulations of Magnetic Resonance Imaging Sequences*. http://arxiv.org/abs/2009.02789

Levitt, M. H., Suter, D., & Ernst, R. R. (1986). Spin dynamics and thermodynamics in solid-state NMR cross polarization. *The Journal of Chemical Physics*, *84*(8), 4243–4255. https://doi.org/10.1063/1.450046

Lin, P. Y., Chao, T. C., & Wu, M. L. (2015). Quantitative susceptibility mapping of human brain at 3T: A multisite reproducibility study. *American Journal of Neuroradiology*, *36*(3), 467–474. https://doi.org/10.3174/ajnr.A4137

Ljungberg, E., Damestani, N. L., Wood, T. C., Lythgoe, D. J., Zelaya, F., Williams, S. C. R., Solana, A. B., Barker, G. J., & Wiesinger, F. (2021). Silent zero TE MR neuroimaging: Current state-of-the-art and future directions. *Progress in Nuclear Magnetic Resonance Spectroscopy*, *123*, 73–93. https://doi.org/10.1016/j.pnmrs.2021.03.002

Mansfield, P. (1977). Multi-planar image formation using NMR spin echoes. *Journal of Physics C: Solid State Physics*, *10*(3). https://doi.org/10.1088/0022-3719/10/3/004

Mansfield, Peter, & Grannell, P. K. (1973). NMR'diffraction'in solids? *Journal of Physics C: Solid State Physics*, *6*(22), L422. http://iopscience.iop.org/0022-3719/6/22/007%5Cnpapers3://publication/uuid/6D65ACD7-E390-443C-865E-64ED39749B76

McJury, M. J. (2022). Acoustic Noise and Magnetic Resonance Imaging: A Narrative/Descriptive Review. *Journal of Magnetic Resonance Imaging*, *55*(2), 337–346. https://doi.org/10.1002/jmri.27525

McRobbie, D. W., Moore, E. A., Graves, M. J., & Prince, M. R. (2009). Spaced out: spatial encoding. In *MRI From Picture to Proton* (pp. 108–136). https://doi.org/10.1017/cbo9780511545405.007

Nair, J. R., Van Hecke, W., De Belder, F., Venstermans, C., Van Den Hauwe, L., Van Goethem, J., & Parizel, P. M. (2010). High-resolution susceptibility-weighted imaging at 3 T with a 32-channel head coil: Technique and clinical applications. *American Journal of Roentgenology*, *195*(4), 1007–1014. https://doi.org/10.2214/AJR.10.4218

Panych, L. P., & Madore, B. (2018). The physics of MRI safety. *Journal of Magnetic Resonance Imaging*, *47*(1), 28–43. https://doi.org/10.1002/jmri.25761

Purcell, E. M. (1946). Resonance Absorption by Nuclear Magnetic Moments in a Solid. *Phys. Rev*, *69*(681), 681.

Rabi, I. I. (1937). Space quantization in a gyrating magnetic field. *Physical Review*, *51*(8), 652–654. https://doi.org/10.1103/PhysRev.51.652

Rooney, W. D., Johnson, G., Li, X., Cohen, E. R., Kim, S. G., Ugurbil, K., & Springer, C. S. (2007). Magnetic field and tissue dependencies of human brain longitudinal 1H2O relaxation in vivo. *Magnetic Resonance in Medicine*, *57*(2), 308–318. https://doi.org/10.1002/mrm.21122

Spincemaille, P., Anderson, J., Wu, G., Yang, B., Fung, M., Li, K., Li, S., Kovanlikaya, I., Gupta, A., Kelley, D., Benhamo, N., & Wang, Y. (2020). Quantitative Susceptibility Mapping: MRI at 7T versus 3T. *Journal of Neuroimaging*, *30*(1), 65–75. https://doi.org/10.1111/jon.12669

Stanisz, G. J., Odrobina, E. E., Pun, J., Escaravage, M., Graham, S. J., Bronskill, M. J., & Henkelman, R. M. (2005). T1, T2 relaxation and magnetization transfer in tissue at 3T. *Magnetic Resonance in Medicine*, *54*(3), 507–512. https://doi.org/10.1002/mrm.20605

Stig, L. (1983). A simple graphical representation of fourier-based imaging methods. *Journal*

of Magnetic Resonance, *54*, 338–343.

Sun, X. C., & Jiang, Y. (2008). Genetic susceptibility to traumatic brain injury and apolipoprotein E gene. *Chinese Journal of Traumatology - English Edition*, *11*(4), 247–252. https://doi.org/10.1016/S1008-1275(08)60051-6

Tang, M. Y., Chen, T. W., Zhang, X. M., & Huang, X. H. (2014). GRE T2* -weighted MRI: Principles and clinical applications. *BioMed Research International*, *2014*. https://doi.org/10.1155/2014/312142

Tsai, L. L., Grant, A. K., Mortele, K. J., Kung, J. W., & Smith, M. P. (2015). A practical guide to MR imaging safety: What radiologists need to know. *Radiographics*, *35*(6), 1722–1737. https://doi.org/10.1148/rg.2015150108

Van Der Kolk, A. G., Hendrikse, J., Zwanenburg, J. J. M., Visser, F., & Luijten, P. R. (2013). Clinical applications of 7 T MRI in the brain. *European Journal of Radiology*, *82*(5), 708–718. https://doi.org/10.1016/j.ejrad.2011.07.007

Vaughan, J. T., Garwood, M., Collins, C. M., Liu, W., Delabarre, L., Adriany, G., Andersen, P., Merkle, H., Goebel, R., Smith, M. B., & Ugurbil, K. (2001). 7T vs. 4T: RF power, homogeneity, and signal-to-noise comparison in head images. *Magnetic Resonance in Medicine*, *46*(1), 24–30. https://doi.org/10.1002/mrm.1156

Wang Y. (2012). *Principles of Magnetic Resonance Imaging: Physics concepts, Pulse Sequences, & Biomedical Applications.* Independent Publishing Platform.

Wisse, L. E. M., Biessels, G. J., Heringa, S. M., Kuijf, H. J., Koek, D. L., Luijten, P. R., & Geerlings, M. I. (2014). Hippocampal subfield volumes at 7T in early Alzheimer's disease and normal aging. *Neurobiology of Aging*, *35*(9), 2039–2045. https://doi.org/10.1016/j.neurobiolaging.2014.02.021

Yoo, S., Kim, J. won, Schenck, J. F., & Lee, S. K. (2020). Magnetic susceptibility imaging of human habenula at 3 T. *Scientific Reports*, *10*(1), 1–15. https://doi.org/10.1038/s41598-

020-75733-y

Zhou, D., Liu, T., Spincemaille, P., & Wang, Y. (2014). Background field removal by solving the Laplacian boundary value problem. *NMR in Biomedicine*, *27*(3), 312–319. https://doi.org/10.1002/nbm.3064

CHAPTER THREE

3.0 REPRODUCIBILITY OF 7T MEASUREMENTS OF THE SUSCEPTIBILITY AND VOLUME OF HIPPOCAMPAL SUBFIELDS

3.1 OUTLINE

This chapter focuses on the reproducibility of measurements of the magnetic susceptibility and volume of the hippocampal subfields in ten healthy participants. The data for this study was obtained from a travelling heads study carried out by the UK7T network, before I commenced my PhD programme. In this travelling heads study each participant underwent six scans - five at their home site and one at each of the other four sites (Clarke et al., 2020).

The imaging protocol included acquiring high-resolution, 3D, single-echo gradient echo images for calculating quantitative susceptibility maps. Additionally, MPRAGE and TSE data were acquired for hippocampal segmentation, where the ASHS (Automatic Segmentation of Hippocampal Subfields) method was used (Yushkevich et al., 2015). Furthermore, susceptibility maps of the whole brain were calculated using QSMbox (Acosta-Cabronero et al., 2018).

The reproducibility of the measurements of the average susceptibility and volume of each hippocampal subfield was analysed using the five data sets acquired on each subject at their home site. This analysis allowed the determination of the expected level of variability in repeated measurements of the magnetic susceptibility and volume of hippocampal sub-fields at 7T. The results are important for planning longitudinal studies aimed at tracking changes in the hippocampus, especially in Alzheimer's disease research.

In summary, this chapter describes the methodology and analysis used to investigate the reproducibility of measurements of the magnetic susceptibility and volume of the hippocampal

subfields. The results provide valuable insights into the expected variability in these measurements, which is crucial for future research in this field.

3.2 INTRODUCTION

Iron is a crucial element in the development of the brain, as it plays a vital role in various neural processes. These processes include oxygen transportation, respiration, DNA synthesis, myelin production, and the synthesis and metabolism of neurotransmitters (Pinero and Connor 2000). Recent advances in neuroimaging techniques have made it possible to study brain iron concentration at the sub-millimeter level. Quantitative susceptibility mapping (QSM) at 7T provides a powerful approach for characterizing iron concentration in the brain (Betts et al., 2016, Rua et al. 2020). Several studies, including post mortem and in vivo human studies, have reported abnormal brain iron deposition in neurodegenerative diseases such as Alzheimer's disease (AD) and Parkinson's disease (PD). For instance, studies have found increased iron accumulation in the hippocampus and other brain regions in AD patients (Cornett et al. 1998; Bartzokis et al. 2000). Similarly, studies have reported elevated iron levels in the substantia nigra and other brain regions in PD patients (Bartzokis et al. 1999; Bunzeck et al. 2013; Sofic et al. 1991).

Overall, the ability to accurately measure brain iron concentration using QSM has led to significant advancements in our understanding of the role of iron in neurodegenerative diseases. These findings have important implications for the development of new diagnostic and therapeutic strategies for these debilitating conditions.

The hippocampus is an important brain structure located deep in the medial temporal lobes on both sides of the brainstem near to the cerebellum. It is involved in many brain functions such as memory and spatial reasoning (Manjon et al., 2020). The hippocampus, and in particular the CA1 sub-region (CA = cornu ammonis), is vulnerable to metabolic stress, a process which can

be observed in acute neurological disorders such as ischaemia, limbic encephalitis, hypoglycaemic encephalopathy, epilepsy, multiple sclerosis, and transient global amnesia. (Thorsten, 2012). Alzheimer's disease (AD) is a neurodegenerative disease which shows early degeneration of the hippocampus (Braak & Braak, 1991). Furthermore, estimation of the volume of the hippocampus is considered a valuable tool for follow-up and treatment adjustment (Jack et al., 2005). Magnetic resonance imaging has become an important imaging technique for the in vivo analysis and mapping of brain iron (Birkl et al., 2020). Magnetic susceptibility describes the magnetizability of a material when exposed to an applied magnetic field and represents an important parameter in the field of MRI (Deistung et al., 2017b). Several MRI techniques have been used for the analysis of the iron content of the brain (Birkl et al., 2020). These techniques include relaxation time mapping (Haacke et al., 2005), Susceptibility Weighted Imaging (SWI) (Mittal et al., 2009), phase imaging (Hopp et al., 2010), Quantitative Susceptibility Mapping (QSM) (Haacke et al., 2015;Nguyen et al., 2020; Wang and Liu 2015), and direct saturation imaging (Smith et al., 2009), among others. Quantitative Susceptibility Mapping (QSM) was used for brain iron mapping in this study. The QSM analysis was carried out using a Bayesian QSM algorithm, named Multi-Scale Dipole Inversion (MSDI) (Acosta-Cabronero et al., 2018) .

In this study, we have characterised the reproducibility of high-resolution 7T susceptibility measurements in the sub-fields of the hippocampus, specifically focusing upon the Cornu Ammonis (CA), the tail of the hippocampus (TAIL), the dentate gyrus (DG), the subiculum (SUB) and the entorhinal cortex (ERC). The UK7T travelling head study data set (Clarke et al., 2020) was used for this study, which was carried out in preparation for measurements of longitudinal changes in the hippocampal sub-fields in Alzheimer's disease.

3.2.1 MAGNETIC SUSCEPTIBILITY MAPPING

The total net magnetization $\boldsymbol{M}$ of tissue exposed to magnetic field $\boldsymbol{H}$ is

$$\boldsymbol{M} = \chi \boldsymbol{H} \qquad [3.1]$$

where χ is a dimensionless proportionality constant known as the volume magnetic susceptibility. The magnetic susceptibility depends on magnetic effects of electrons, rather than the nuclei, in materials. Materials can be classified into different groups depending on the degree to which they are magnetised. *Paramagnetic* materials have susceptibility values greater than zero ($\chi > 0$), and they usually contain atoms or molecules with a magnetic moment. *Diamagnetic* materials have susceptibility values that are less than zero ($\chi < 0$), and their dipole moment is induced in the presence of an external field. *Ferromagnetic* materials, have large positive susceptibility values ($\chi \gg 1$) and can remain magnetised in the absence of an applied magnetic field.

The susceptibility of brain tissue is slightly diamagnetic since water is the main component (about 70-85%)(Ravanfar et al., 2021) and the overall magnetization is zero in the absence of an external field (Acosta-Cabronero et al., 2013). Susceptibility values are slightly different for each tissue or substance in the brain due to differences in tissue composition. For example, variation in the content of paramagnetic deoxyhemoglobin in venous blood or of the concentration of ferritin in tissue changes the susceptibility, and density variation effects the diamagnetic susceptibility – e.g. hard bone has a more negative susceptibility than soft tissue, while air-filled sinuses have a less negative susceptibility. The sensitivity to iron content means that mapping the susceptibility values in the brain is very important especially when dealing with neurodegenerative diseases such as Alzheimer's disease (AD), Parkinson's Disease or multiple sclerosis, as these diseases have shown abnormal deposition of iron (Cornett et al. 1998; Bartzokis et al. 2000; Bartzokis et al. 1999; Bunzeck et al. 2013; Sofic et al. 1991).

3.2.2 MAGNETIC SUSCEPTIBILITY MEASUREMENT

Spatial variation of the magnetic susceptibility causes changes in the local magnetic field, ΔB_z, which also produce small changes in the resonance frequency $\Delta\omega = \gamma \Delta B_z$. These changes

can be detected by evaluating the phase $\Delta\phi$ of gradient echo measurements. In a measurement with echo time TE the phase is given by

$$\Delta\phi = -\gamma \Delta B_z TE \qquad [3.2]$$

We can see from Eq. 3.2 that phase measurements can potentially be used to determine the magnetic properties of tissue.

3.2.3 QUANTITATIVE SUSCEPTIBILITY MAPPING

In this research we used quantitative susceptibility mapping (QSM) to investigate the susceptibility differences in the brain using the magnitude and phase data from gradient echo scans. QSM involves solving the complex field-to-source inversion problem so as to produce quantitative maps of the magnetic susceptibility variation in tissue from gradient echo phase data (Haacke et al., 2015).

In this study we used single echo gradient echo data for QSM and the pipeline for processing this data to obtain the susceptibility maps is explained as follows. (i) The single echo GE phase and magnitude data are acquired. (ii) Since the phase data are defined between (-π, π) it is necessary to unwrap the phase maps to produce maps of the variation of the local field ΔB_z. In this work we used a Laplacian-based method for phase unwrapping (Deistung et al., 2017a) as shown in Fig 3.0.

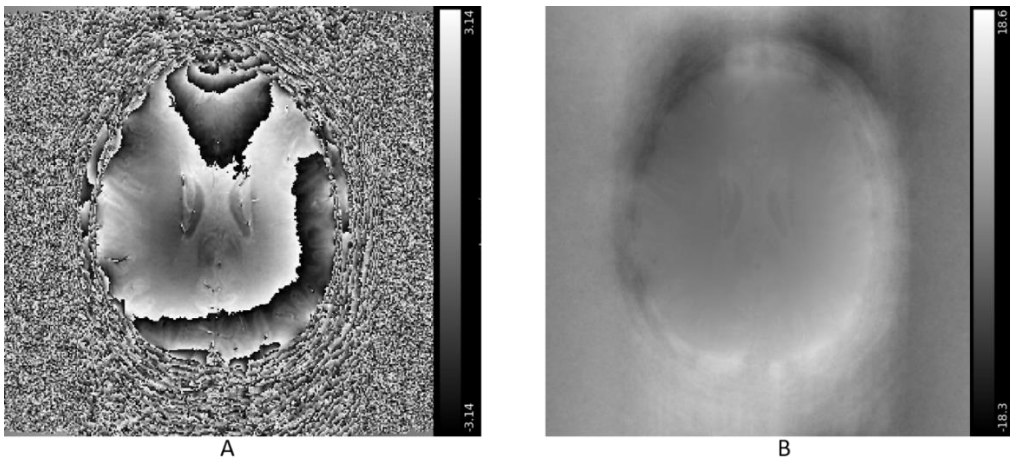


Figure 3.0: A) showing the raw phase data in one axial slice of a single echo GE scan and B) the unwrapped phase in the same slice that was produced using the Laplacian-based method (Deistung et al., 2017a).

(iii) The measured magnetic field is made up of two contributions

$$\Delta B_z = \Delta B_{int} + \Delta B_{bkg} \quad . \quad [3.3]$$

ΔB_{int} is the field perturbation produced by magnetic susceptibility variation from within the target or volume of interest (VOI) while ΔB_{bkg} is the background field produced by field sources outside the VOI. Such sources can include air-tissue interfaces at the surface of the head and the rest of the body and field variation from shim coils. It is necessary to perform background field removal so that subsequent analysis is only applied to the field perturbation from magnetic susceptibility variation in the VOI. This was achieved by solving the Laplacian-equation using the spherical mean value property of the background field and using the SHARP (Sophisticated Harmonics Artefact Reduction in Phase data) method which convolves the estimated magnetic field perturbation together with a spherical kernel, and then deconvolves and masks the image obtained (Acosta-Cabronero et al. 2018; Deistung et al. 2017b).The relationship between the background field-corrected field map and the magnetic susceptibility distribution is given as

$$\Delta B_{int}(\vec{r}) = B_0 \cdot \int_{VOI} \chi(\overrightarrow{r'}) \cdot d_z(\vec{r} - \vec{r}')d^3\,\vec{r}' \quad [3.4]$$

where χ is the magnetic susceptibility and d_z is the dipole field

$$d_z(\vec{r}) = \frac{(3cos^2\theta - 1)}{4\pi|\vec{r}|^3} \quad [3.5]$$

and $cos\ \theta = \vec{r}.\hat{z}$ where $\hat{z}$ is a unit vector in the z-direction.

Fourier transformation of Eq. 3.4 and use of the convolution theorem gives

$$\frac{\Delta B_z(\vec{k})}{B_0} = \left[\frac{1}{3} - \frac{{k_z}^2}{|\vec{k}|^2}\right]\chi(\vec{k}) \quad [3.6]$$

where $k_z = \vec{k}.\hat{z}$. This equation can be rearranged to give the Fourier transform of the susceptibility in terms of the field.

$$\chi(\vec{k}) = \frac{\Delta B_z(\vec{k})}{B_0\left[\frac{1}{3} - \frac{{k_z}^2}{|\vec{k}|^2}\right]} \qquad [3.7]$$

These equations show that we can deconvolve the dipole field from the background field-corrected field perturbation to obtain the bulk magnetic susceptibility distribution in the VOI. However, Eq. [3.7] shows that the inverse problem is ill-posed because the Fourier transform of the dipole field which appears in the denominator goes to zero over two conical surfaces in the Fourier domain. Many different methods have been used to solve the ill-posed inverse problem, but in this study we used a novel Bayesian QSM algorithm called Multi-Scale Dipole Inversion (MSDI) (Acosta-Cabronero et al., 2018).

3.3 METHODS

The data used in this study was obtained from the UK7T data repository, and its acquisition in the UK7T travelling heads study predates the commencement of my PhD studies. Therefore, the primary responsibility for data acquisition, quality assurance, and ethical considerations lies with the original data collectors. The UK7T dataset comprises MRI data acquired using 7 T magnetic resonance imaging (MRI) scanners, which offer higher field strength compared to standard clinical scanners.

The primary objective of my study is to leverage the valuable information available in the UK7T dataset to address specific research questions related to the segmentation of hippocampal subfields and the quantification of both their volume and susceptibility. The access to the comprehensive UK7T dataset was instrumental in facilitating in-depth analyses and deriving meaningful conclusions that contribute to the advancement of knowledge in this area of research. It has allowed for the exploration of research questions that would have been challenging to address solely within the scope of my PhD program given the effect of the

COVID lock-down. To the best of our knowledge, no previous work has specifically explored susceptibility mapping of hippocampal subfields at this high field strength.

While susceptibility-based imaging and quantitative susceptibility mapping (QSM) have previously been used to investigate the whole hippocampus and other brain structures (Möller et al., 2019, Schweser et al., 2011, Rua et al., 2020, Ravanfar et al., 2021), exploring the hippocampal subfields poses unique challenges due to their small size and complex anatomy. The high spatial resolution of 7T MRI provides an unprecedented opportunity to address these challenges and explore susceptibility-related phenomena within the hippocampal subfields in greater detail.

3.3.1 IMAGING PROTOCOL

Ten healthy volunteers (age 32 ± 6 years) were scanned with informed consent and ethics approval for a multi-site study. Two participants were scanned at each site: subj01 and subj02 were scanned at the Wolfson Brain Imaging Centre, University of Cambridge, subj03 and subj04 at the Cardiff University Brain Research Imaging Centre, Cardiff University, subj05 and subj06 at the Imaging Centre of Excellence, University of Glasgow, subj07 and subj08 at the Sir Peter Mansfield Imaging Centre, University of Nottingham and subj09 and subj10 at the Wellcome Centre for Integrative Neuroimaging (FMRIB), University of Oxford. Each subject was scanned five times at their "home" site using the scanners shown in Table 3.1 below.

Table 3.1: Scanner systems used at each site for data acquisition in the UK7T travelling head study.

	Location	Vendor	model	Software
1	Wellcome Centre for Integrative Neuroimaging (FMRIB), University of Oxford	Siemens	Magnetom 7T	VB17A
2	Cardiff University Brain Research Imaging Centre, Cardiff University	Siemens	Magnetom 7T	VB17A
3	Sir Peter Mansfield Imaging Centre, University of Nottingham	Philips	Achieva 7T	R5.1.7.0

4	Wolfson Brain Imaging Centre, University of Cambridge	Siemens	Magnetom Terra	VE11U
5	Imaging Centre of Excellence, University of Glasgow	Siemens	Magnetom Terra	VE11U

All scanners used in the data acquisition were equipped with a Nova Medical (Wilmington MA, USA) single-channel transmit, 32-channel receive (1Tx; 32Rx) head coil. All protocols were optimised for use with this coil.

The image acquisition used for QSM was a whole-brain, 3D, single-echo GE sequence with an echo time of 20 ms. Additional imaging parameters were: repetition time (TR)=43 ms; Field of view 224 × 224 × 224 mm^3, voxel size, 0.7 ×0.7 ×0.7 mm^3, and frequency per pixel of 70 Hz. The data acquisition time for this sequence was 12:38 minutes (Clarke et al., 2020).

A T_1-weighted 3D-MP2RAGE image data set was also acquired for each subject. The following acquisition parameters were used: inversion times of 725/2150 ms; echo time (TE) of 2.64 ms; TR= 3500 ms; Field of view 224 × 224 × 224 mm^3; 0.8 × 0.8 ×0.8 mm^3 voxel size; receiver bandwidth of 300 Hz; the total time for this scan was 7:51 minutes, as described in (Clarke et al., 2020).

T_2-weighted images spanning the hippocampus were also acquired from each subject. The acquisition parameters were as follows: partial brain TSE sequence, with a resolution of 0.4 × 0.4 ×1.0 mm^3; field of view of 224 × 224 × 55 mm^3 ; TR = 8020ms; TE = 76 ms and a bandwidth per pixel of 155 Hz. The acquisition time for this sequence was 4:32 minutes. (Clarke et al., 2020). The slice orientation was chosen so that the slices ran orthogonal to the longest axis of the hippocampus.

3.3.2 PREVIOUS WORK ON UK7T DATA FOR QSM REPRODUCIBILITY

In previous work, (Rua, et al., 2020) used the same UK7T travelling heads data set to evaluate the reproducibility of quantitative susceptibility mapping (QSM) and R_2^* measurements made

in the human brain using 7T MRI. The primary objective of the previous study was to assess the reliability and consistency of QSM and R_2^* measurements in different brain regions acquired across five different sites operating at 7T. This was made possible by the use of T2*-weighted sequences which had been harmonised across the three different scanner platforms from two different vendors that were used in this study (Clarke et al., 2020). Two different protocols were compared: a single-echo 0.7mm isotropic-resolution T2*-weighted scan and a 1.5mm isotropic resolution multi-echo T2*-weighted scan. The main focus of the analysis was the sub-cortical grey matter regions (globus pallidus, caudate nucleus, substantia nigra, red nucleus and putamen). These regions have large positive susceptibility values and high relaxation rates compared to other brain structures due to their high iron content. Cortical grey matter regions were also considered in the analysis, but the reliability of susceptibility measurements in the hippocampus was not specifically considered in Rua's analysis (Rua, et al., 2020).

In their work, Rua *et al* found a 2.0-5.3 fold decrease in the within-site standard deviation and a 2.1-4.8 decrease in cross-site standard deviation for 7T QSM compared to previous 3T studies (Rua, et al., 2020). For R2*, there was an improvement of approximately 3-fold in within-site and cross-site reproducibility at 7T compared to 3T. The study also found higher cross-site than within-site variability, possibly due to differences in gradient systems and in distortion correction and shimming approaches across different scanner platforms. They also found that the single-echo high-resolution QSM showed significantly lower variability than multi-echo low-resolution QSM, most likely due to a reduction in partial volume effects at higher resolution. Rua *et al* also evaluated different approaches for referencing the zero value of susceptibility in the QSM measurements. By analysis of the standard deviation of repeated measurements a whole-brain referencing approach was found to be better than using a CSF mask or a manually positioned ROI in the ventricles.

Overall, Rua et al's work provided valuable insights into the performance and consistency of 7T QSM and R2* measurements across different centres and vendors, showing that ultra-high field 7T MRI showed improved reproducibility in QSM and R2* measurements compared to lower field strengths.

The findings from this study suggested that the single-echo data should be employed for analysis of the susceptibility of hippocampal subfields. This is mainly because the single-echo data has higher spatial resolution than the multi-echo data (0.7mm versus 1.4 mm). Higher resolution helps to reduce partial volume effects, leading to more accurate susceptibility measurements within small structures like the hippocampal subfields.

3.3.3 QSM RECONSTRUCTION

Susceptibility mapping of the brain was conducted using the Multi-Scale Dipole Inversion (MSDI) technique, as implemented in QSMbox v2.0, specifically tailored for single-echo, coil-combined data (Acosta-Cabronero et al., 2018). This innovative approach is an extension of the nonlinear Morphology-Enabled Dipole Inversion (nMEDI) framework proposed by (J. Liu et al., 2012), incorporating a scale-wise implementation of morphological priors. The primary objective of MSDI is to enhance the fidelity of susceptibility data by mitigating the impact of various confounding factors such as flow effects, limited signal-to-noise ratio, and other data inconsistencies that can give rise to undesirable streaking and shadowing artefacts (Acosta-Cabronero et al., 2018).

In essence, MSDI optimizes susceptibility mapping by addressing the challenges posed by these confounding factors, thus yielding more accurate and reliable results. This method holds potential for improving the quality and interpretability of susceptibility maps, which is crucial for extracting meaningful information from neuroimaging data. As depicted in Fig 3.1, a representative axial slice from each subject's susceptibility map highlights the method's effectiveness. These slices showcase distinctive susceptibility patterns, illustrating the elevated

susceptibility values in deep grey matter regions and the contrasting reduced susceptibility values in the optic radiations.

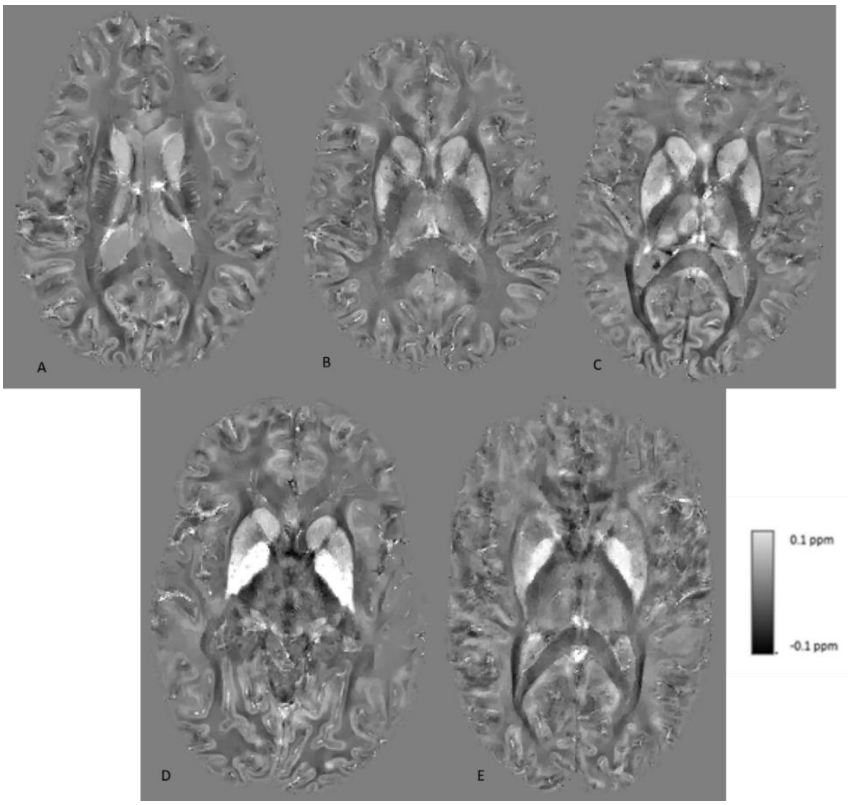


Figure 3.1: Axial slices at the level of the globus pallidus and optic radiations taken from the QSM maps of one participant from each of the 5 sites in this study (A) Subj01 (B) Subj03 (C) Subj05 (D) Subj07 and (E) Subj09.

3.3.4 AUTOMATIC SEGMENTATION OF HIPPOCAMPAL SUBFIELDS (ASHS)

The segmentation of the hippocampus was accomplished through the utilization of the open-source Automatic Segmentation of Hippocampal Subfields (ASHS) software, as developed by Yushkevich and colleagues in 2015 (Yushkevich et al., 2015). The ASHS methodology employs a sophisticated pipeline that amalgamates multi-atlas label fusion with learning-based error correction techniques, creating a robust and accurate approach for hippocampal subfield segmentation (Wisse et al. 2014; Yushkevich et al. 2015).

The ASHS software delineates a comprehensive set of hippocampal subfields, which encompass the Cornu Ammonis (CA) areas including CA1, CA2, and CA3, the hippocampal tail (TAIL), Dentate Gyrus (DG), Subiculum (SUB), CYST, and Entorhinal Cortex (ERC).

Each subfield's susceptibility (measured in ppm) and volume (measured in mm^3) were quantified for every scan. However, it is worth noting that due to the small volumes of the CA2 and CA3 regions the susceptibility values from these regions were highly variable. Consequently, the values of CA1-3 were amalgamated into a single CA measurement, ensuring more consistent results. Furthermore, the CYST compartment, corresponding to fluid-filled cysts, was notably absent in all images, which aligns with expectations for a cohort of young, normal volunteers. As a result, this particular region of interest (ROI) was excluded from the study's scope.

To provide visual context, Fig 3.2 serves as an illustrative representation of the ASHS segmentation process. Specifically, the ASHS-derived segmentation outcomes are superimposed onto TSE (Turbo Spin Echo) image data, offering a visualization of the delineation of hippocampal subfields.

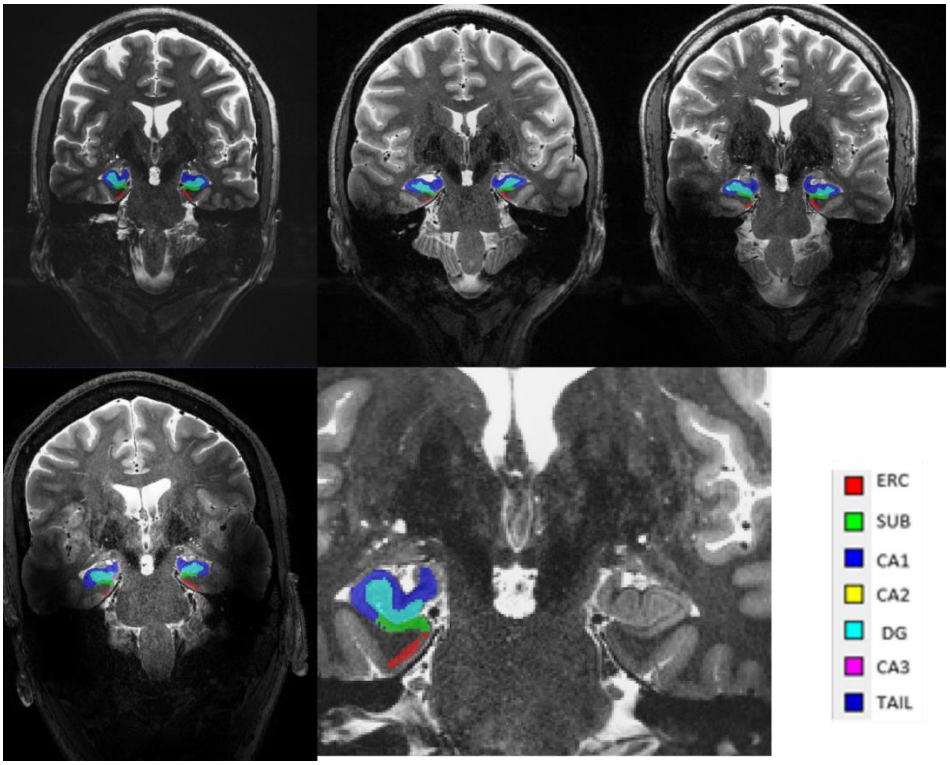


Figure 3.2: TSE images showing the segmented subfields of the hippocampus of one participant from each of the 5 sites in this study (A) Subj01 (B) Subj03 (C) Subj05 (D) Subj07 and (E) Subj09.

3.4 RESULTS

In this analysis, a total of 50 datasets were considered, corresponding to the five repeat measurements acquired on 10 subjects at the 5 different UK7T sites in the travelling head study. Figure 3.3 shows exemplar, high-quality QSM data obtained by applying the MSDI approach to the 0.7mm isotropic resolution GE data, with the segmentation of the hippocampus data overlaid. Segmentation of the hippocampal subfields using the ASHS software took about 3 hours for each participant's data.

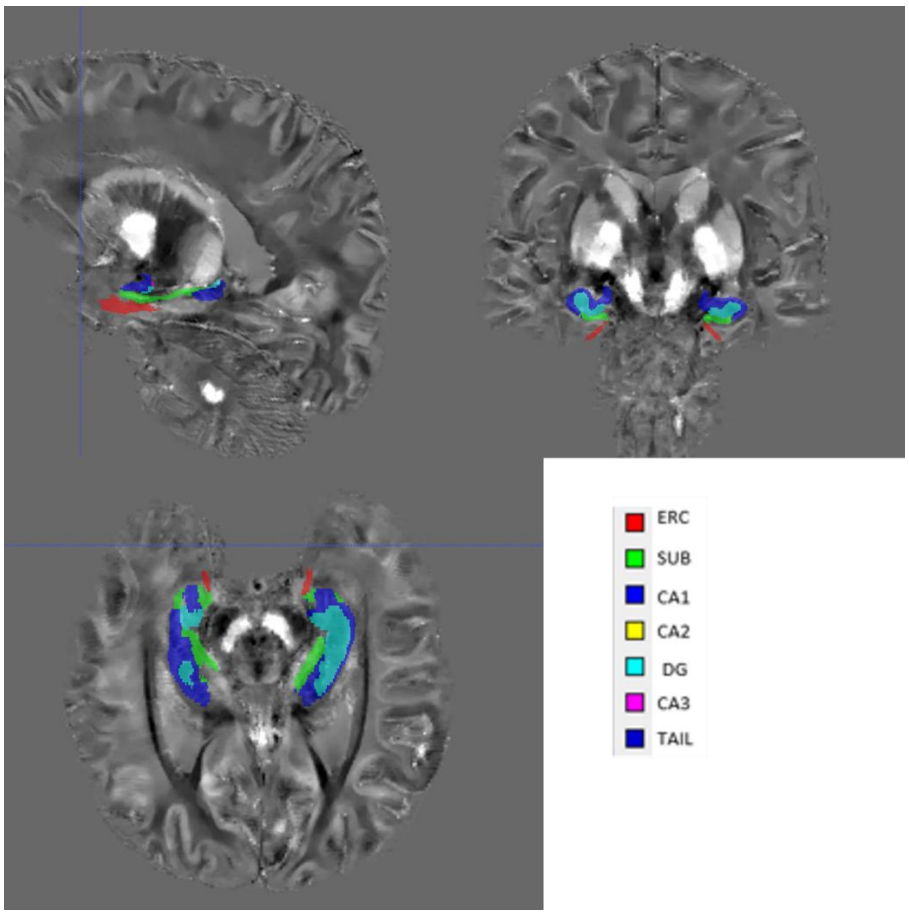


Figure 3. 3: shows a three-plane view of 0.7 mm resolution susceptibility map of one of the subjects, with an overlay of the ASHS segmentation of the hippocampus. This figure provides a visual representation of the segmentation of the hippocampus and the distribution of magnetic susceptibility across the subfields.

3.4.1 REFERENCING THE QSM

Quantitative Susceptibility Mapping (QSM) is a robust technique for assessing relative magnetic susceptibility values (Deistung et al., 2017a). These values are typically referenced

to the average susceptibility within the analysed brain volume. Nevertheless, the choice of reference region holds the potential to influence QSM measurements' accuracy and reproducibility (Birkl et al., 2018). Here we compared the use of two different reference regions, which were the whole brain or a manually defined region of interest (ROI) in the CSF of the lateral ventricles. Figure 3.4 illustrates an example of the positioning of the CSF ROI. The impact of referencing to CSF on QSM measurement reliability was evaluated by computing the average standard deviation of susceptibility across five repeated scans for each participant. In parallel, the same procedure was conducted without CSF referencing, as demonstrated in Fig 3.5. Our findings echoed previous research (Rua, et al., 2020), confirming that referencing to a manually defined region of CSF led to an increase in the standard deviation of measured susceptibility. Consequently, for subsequent analyses, we opted to employ data referenced to the entire brain.



Figure 3. 4: illustrates an example of the manually defined region of interest (ROI) for cerebrospinal fluid (CSF) in red, overlaid on the T2-weighted image. These ROIs were used to measure the susceptibility values of CSF, which were then subtracted from the susceptibility values of other regions of interest to obtain a value of susceptibility referenced to CSF. This referencing method was compared to the default referencing to the average susceptibility in the whole brain volume considered in the analysis.

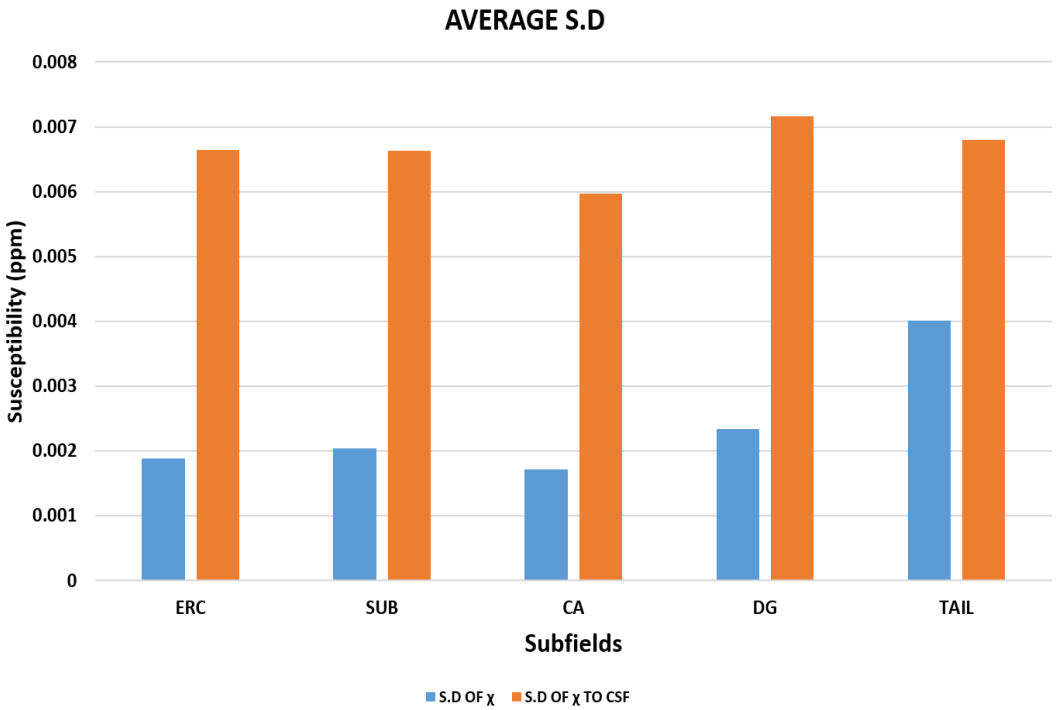


Figure 3. 5: The average across the 10 participants of the value of the standard deviation of the five susceptibility measurements in ppm, with and without referencing to the CSF.

3.4.2 ANALYSIS OF THE REAPEATED MEASUREMENTS

The results of the analysis of the data from all 10 subjects are shown in Figs. 3.6 and 3.7. Figure 3.6 shows the plots of the variation of the susceptibility and absolute volume of each hippocampal sub-field, along with the volumes scaled by the total intra-cranial volume (TIV) (%) for the 10 participants. The associated error bars show the standard deviations over repeated measurements. This plot provides an insight into the distribution of magnetic susceptibility and volume across the different hippocampal subfields.

Fig. 3.7 shows the average over the 10 subjects of the values of the susceptibility, absolute volumes and TIV-corrected volume for each subfield. The error bars show the values of standard deviation of the measurements across subjects.

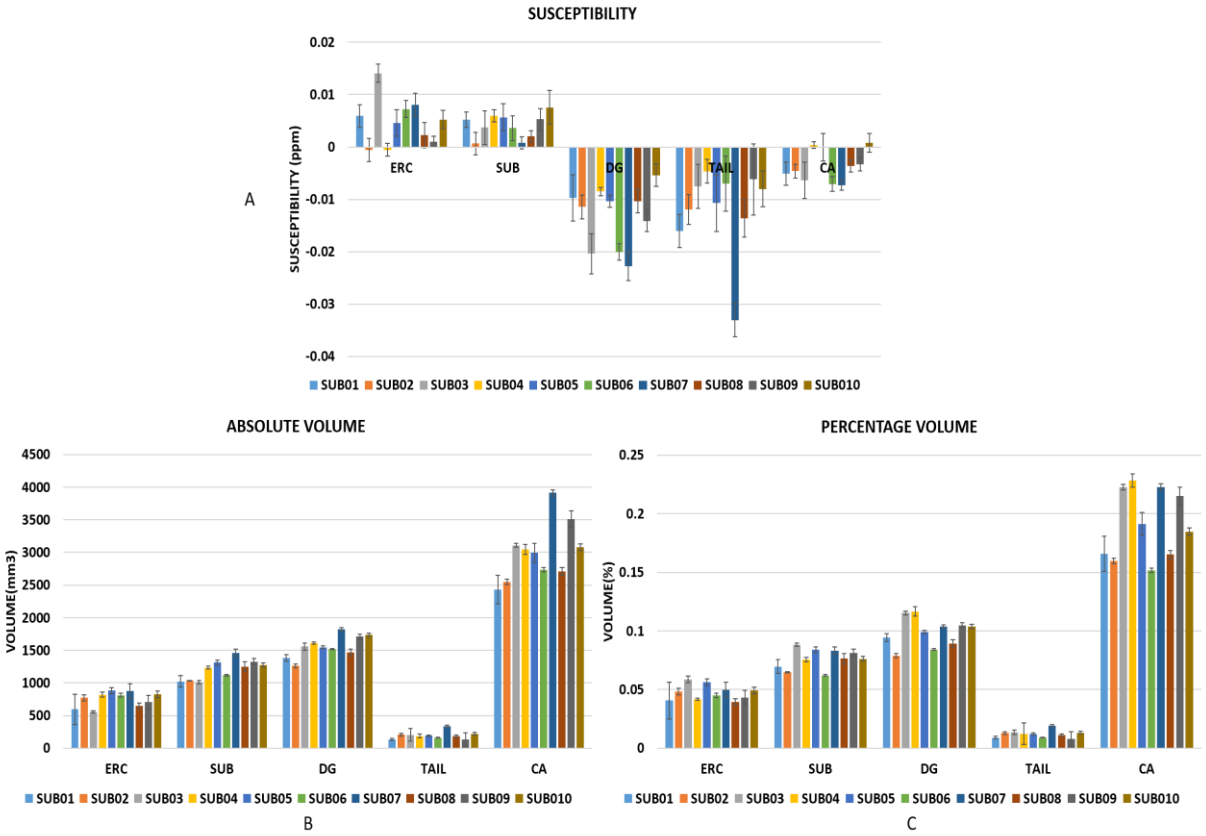


Figure 3. 6: Plots showing the A) susceptibility (ppm), B) Absolute volume (mm^3) and C) Percentage volume (%) averaged over the five repeat measurements of the subfields of the hippocampus for the 10 different subjects. Error bars show the standard deviation across repeated measurements.

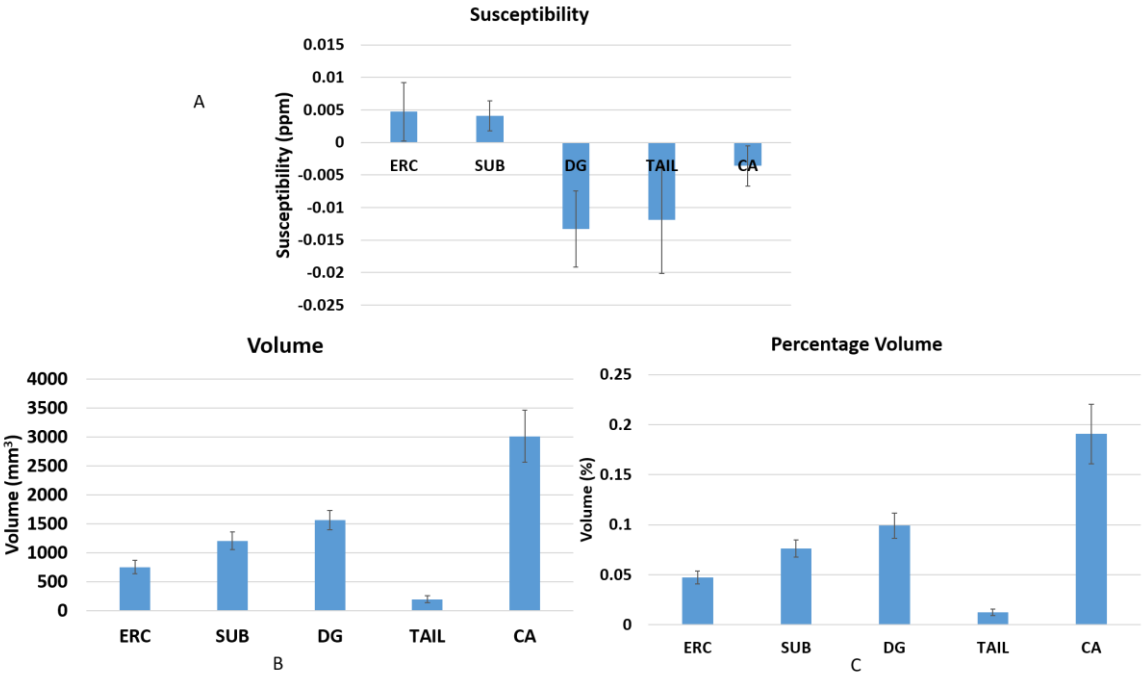


Figure 3. 7: shows the average values of A) susceptibility B) Absolute volume and C) TIV-scaled percentage volume in the different subfields of the hippocampus for the ten participants. The error bars indicate the standard deviation across participants.

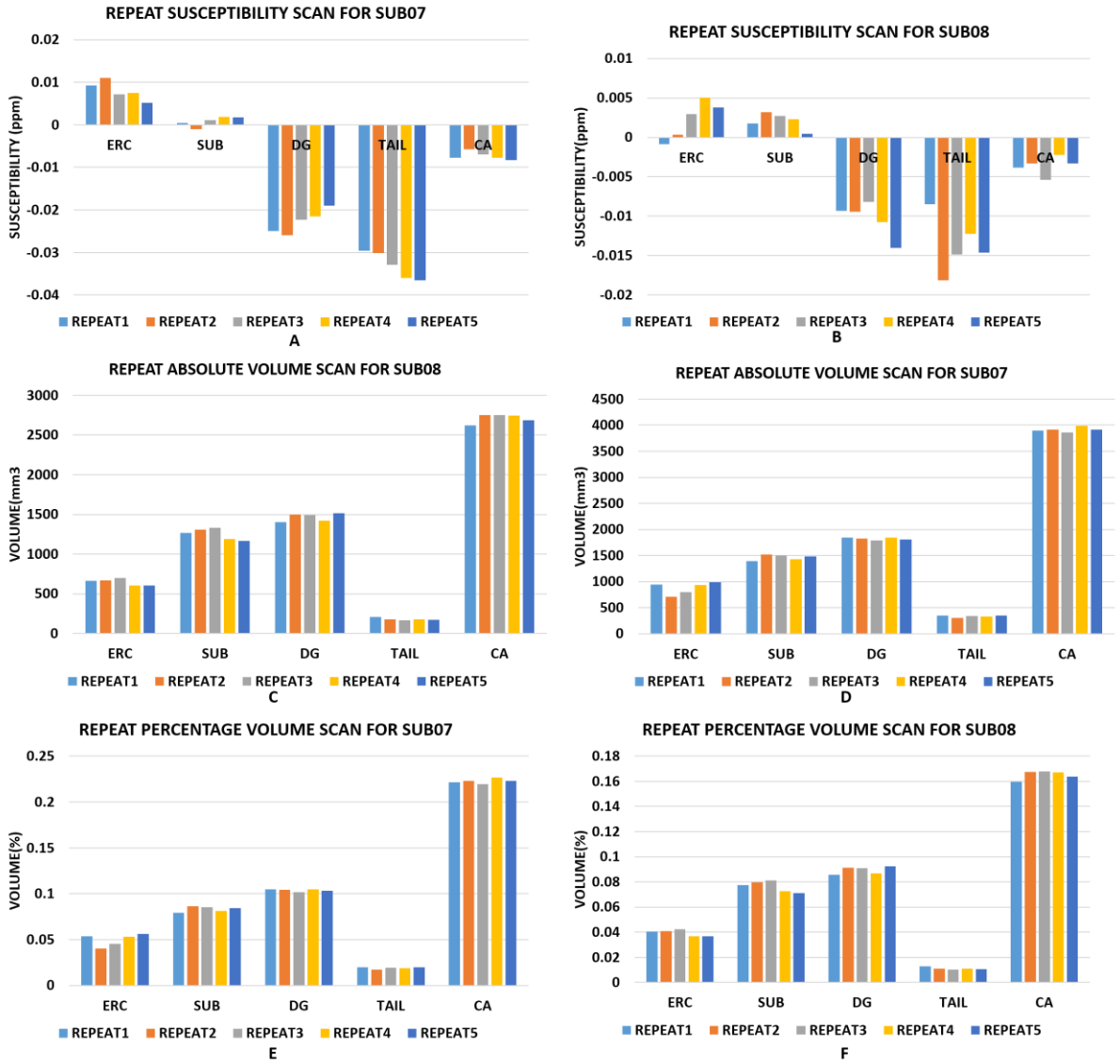


Figure 3. 8: Values of (A) susceptibility for sub07 (B) susceptibility for sub08 (C) volume of sub07 (D) volume for sub08 (E) TIV-scaled volume for sub07 (F) TIV-scaled volume for sub08, for the five repeated measurements at the Nottingham site.

SEGMENT	Susceptibility (ppm)			Absolute Volume (mm^3)			Percentage Volume (%)		
	MEAN	S.D. across subjects	Average of S.D. across repeats	MEAN	S.D. across subjects	Average of S.D. across repeats	MEAN	S.D. across subjects	Average of S.D. across repeats
ERC	0.0047	0.0045	0.0019	748	116	71	0.0472	0.0065	0.0045
SUB	0.0041	0.0023	0.002	1204	153	40	0.0761	0.0085	0.0025
DG	-0.0133	0.0058	0.0023	1561	168	33	0.099	0.0124	0.0021
TAIL	-0.0119	0.0082	0.004	194	57	33	0.012	0.0031	0.0024
CA	-0.0036	0.0031	0.0017	3008	448	83	0.1907	0.0296	0.0054

Table 3. 2: Average value of the susceptibility, absolute volume and percentage volume across the 10 participants and the respective standard deviations across subjects and the average of the standard deviation over repeats across all participants.

Absolute Volume (mm3)		Percentage Volume (%)	
COV-Across Subjects	COV-Across Repeats	COV-Across Subjects	COV-Across Repeats
0.16	0.095	0.14	0.096
0.13	0.033	0.11	0.033
0.11	0.021	0.13	0.022
0.29	0.170	0.26	0.202
0.15	0.028	0.15	0.028

Table 3. 3: coefficient of variation analysis of the absolute volume and TIV corrected volume for standard deviation across subjects and that across the repeated scans

	SUSCEPTIBILITY		ABSOLUTE VOLUME		PERCENTAGE VOLUME	
SEGMENT	SUB07	SUB08	SUB07	SUB08	SUB07	SUB08
ERC	0.276	0.393	0.130	0.064	0.130	0.064
SUB	0.592	0.503	0.037	0.057	0.037	0.057
DG	-0.122	-0.188	0.013	0.034	0.013	0.034
TAIL	-0.320	-0.262	0.048	0.090	0.048	0.090
CA	-0.097	-0.118	0.012	0.021	0.012	0.021

Table 3. 4 Coefficient of variation (COV) analysis for segmented hippocampal subfields in participants sub07 and sub08 from the UK7T study, COV calculated as the standard deviation over repeated measurements divided by the mean.

The standard deviation of the susceptibility value measured over subjects was approximately twice as large as the average of the standard deviation across repeated measurements in most sub-regions (except in SUB, where the two values were similar). The results show that the differences in susceptibility values between subjects are generally larger than the repeat measurement error in individual subjects, indicating that the small differences in regional

susceptibility values between individuals can be characterised. The volume measurements show similar behaviour with the standard deviation of the average values over subjects being more than 1.6 times as large as the standard deviation over repeated measurements for all ROIs.

3.5 DISCUSSION

This study has characterised the reproducibility of hippocampal subfield volume and susceptibility, which is important information to know before embarking on longitudinal studies involving individuals with Alzheimer's disease. By utilizing high-resolution GE scans from five different 7T scanners and implementing ASHS for precise subfield segmentation, the research quantified hippocampal subfield volume and susceptibility with a reasonable degree of consistency across various sites.

A previous study (Rua, et al., 2020) on UK7T data demonstrated favourable reproducibility for QSM using single-echo data, with within-subject standard deviations ranging from 0.001 ppm to 0.005 ppm for manually defined subcortical and cortical regions of interest (substantia nigra, red nucleus, caudate nucleus, putamen, and globus pallidus).

The study described here identified certain limitations in ASHS segmentation, particularly in smaller structures like CA2, CA3, and CYST. To mitigate this, the study combined some of these structures to derive more reliable susceptibility and volume values. For instance, CA1-3 values were amalgamated into a single CA measurement, while the CYST compartment, largely absent in young, normal volunteers, was excluded. Additionally, combining left and right subfield values added stability to the presented results. Addressing the potential limitation of uncertain susceptibility values for the CSF could involve pulse sequence modifications to incorporate flow compensation for all echoes (Lin, Chao, and Wu 2015; Gilbert et al. 2012; Liu et al. 2013).

A notable finding of this research is the consistent pattern of susceptibility variation across hippocampal sub-regions, ranging from -33 to 14 ppb, as depicted in Fig 3.6. The ERC and

SUB regions exhibited negative susceptibility values, whereas DG, TAIL, and CA generally displayed consistent negative susceptibility.

Furthermore, the study's results indicated that differences in susceptibility values between individuals (10 participants) were typically larger than the repeat measurement error within participants. This suggests that QSM is sufficiently sensitive to capture subtle differences in regional susceptibility values between subjects, thereby facilitating individual characterization and potential early detection of neurological disorders.

Statistical analysis of susceptibility using one-way repeated measure ANOVA, with a computational alpha of 0.05, revealed no statistically significant differences within repeats for subfields CA, SUB, ERC, DG, and TAIL ($p \geq 0.38$). The standard deviation of susceptibility within each site's repeat ranged from 0.001 ppm to 0.004 ppm (Table 3.2), with the tail exhibiting the highest values. This trend is also evident in Table 3.4 and Figure 3.8, where the coefficient of variation (COV) and the five-repeat plot were computed, showcasing the highest COV values in the TAIL and SUB. Generally, smaller subfields exhibit a greater potential for errors in identification from ASHS. Variability in susceptibility values across repeats may arise from noise and artefacts, including motion artefacts or magnetic field inconsistencies (Llera et al., 2019, Graham et al., 2017). Participant positioning during scans can also contribute to susceptibility variability (Yoo, Kim, et al., 2020, Yoo, Song, et al., 2020, Rua et al., 2020).

The variability in susceptibility values observed in Figure 3.6 for each participant and segmented subfields may stem from a combination of factors related to individual differences and technical considerations. Factors such as genetic variability, physiological differences, iron content, myelin content, and brain anatomy can contribute to susceptibility value variations (Hagemeier et al., 2018, An et al., 2011, Yablonskiy et al., 2013, Mudd et al., 2018, Bartzokis et al., 2004, Yao et al., 2017, Van Der Weijden et al., 2023, Papadaki et al., 2019, Mancini et

al., 2020, Duyn & Schenck, 2017, Llera et al., 2019). These factors collectively lead to the observed variability in susceptibility values among participants of the same age group.

Our results show that the choice of a reference region in QSM analysis has significant implications for interpretation of measurements. While CSF is commonly used, other reference regions like white matter or a combination of CSF and white matter have been proposed (Birkl et al., 2018). The selection of the reference region should align with the specific research question and the anticipated susceptibility contrast between regions of interest and the selected reference region. This consideration ensures the accuracy and consistency of QSM outcomes, aligning with the study's overarching objectives. In this study, referencing QSM values to CSF is chosen; however, referencing to CSF, as shown in Figure 3.4, increases result variability. This may arise from the effects of the choroid plexus, composed of a network of blood vessels covered by specialized cells that actively transport substances into the CSF and regulate its composition (MacAulay et al., 2022).

Regarding volume, there was substantial reproducibility in subfield segmentation of hippocampus, as evidenced by Table 3.3, which reports COV values for volume measurements using both the standard deviation across subjects and the average standard deviation across repeat measurements. It is evident from these values that the average standard deviation across repeat measurements is smaller than the standard deviation across subjects, showing that differences in the hippocampal volumes across subjects can be characterised. The COV values found by using the standard deviation across subjects are similar when using the absolute volume or the TIV-scaled volume, indicating that scaling the volumes of the hippocampal sub-field volumes by total intracranial volume does not significantly reduce the variance of measurements across the group of 10 subjects. The homogeneity in morphology and the overall health of the participants may have led to relatively uniform brain structures, including the hippocampus, resulting in minimal variations between absolute and TIV-corrected volume

measurements. This further supports the reliability of our findings and suggests that the TIV correction did not introduce significant differences in the volume calculations for these participants.

Statistical analysis of volume using one-way repeated measure ANOVA, with a computational alpha of 0.05, demonstrated no statistically significant differences within repeats for all subfields CA, SUB, ERC, DG, and TAIL ($p \geq 0.8$). This confirms the consistency of results across participants in repeated measures.

3.6 CONCLUSION

In summary, this study's findings underscore the critical role of studying hippocampal subfield susceptibility and volume reproducibility when planning longitudinal studies. The ability to explore microstructural changes, comprehend brain function, detect neurological disorders early, and devise personalized treatment approaches underscores the significance of this research. By contributing to neuroimaging advancement and offering potential subfield-specific therapeutics, this study introduces new prospects for precision medicine and enhanced diagnosis and management of neurological conditions. Ultimately, the insights garnered from this research could have profound implications for our understanding of brain health and function.

3.7 REFERENCES

Acosta-Cabronero, J., Milovic, C., Mattern, H., Tejos, C., Speck, O., & Callaghan, M. F. (2018). A robust multi-scale approach to quantitative susceptibility mapping. *NeuroImage*, *183*, 7–24. https://doi.org/10.1016/j.neuroimage.2018.07.065

Acosta-Cabronero, J., Williams, G. B., Cardenas-Blanco, A., Arnold, R. J., Lupson, V., & Nestor, P. J. (2013). In vivo quantitative susceptibility mapping (QSM) in Alzheimer's disease. *PLoS ONE*, *8*(11). https://doi.org/10.1371/journal.pone.0081093

An, H., Liu, Q., Eldeniz, C., & Lin, W. (2011). Absolute Oxygenation Metabolism Measurements Using Magnetic Resonance Imaging. *The Open Neuroimaging Journal*, *5*(Suppl 1), 120–135. https://doi.org/10.2174/1874440001105010120

Bartzokis, G., Cummings, J. L., Markham, C. H., Marmarelis, P. Z., Treciokas, L. J., Tishler, T. A., Marder, S. R., & Mintz, J. (1999). MRI evaluation of brain iron in earlier- and later-onset Parkinson's disease and normal subjects. *Magnetic Resonance Imaging*, *17*(2), 213–222. https://doi.org/10.1016/S0730-725X(98)00155-6

Bartzokis, G., Sultzer, D., Cummings, J., Holt, L. E., Hance, D. B., Henderson, V. W., & Mintz, J. (2000). In vivo evaluation of brain iron in Alzheimer disease using magnetic resonance imaging. *Archives of General Psychiatry*, *57*(1), 47–53. https://doi.org/10.1001/archpsyc.57.1.47

Bartzokis, G., Tishler, T. A., Shin, I. S., Lu, P. H., & Cummings, J. L. (2004). Brain ferritin iron as a risk factor for age at onset in neurodegenerative diseases. *Annals of the New York Academy of Sciences*, *1012*, 224–236. https://doi.org/10.1196/annals.1306.019

Betts, M. J., Acosta-Cabronero, J., Cardenas-Blanco, A., Nestor, P. J., & Düzel, E. (2016). High-resolution characterisation of the aging brain using simultaneous quantitative susceptibility mapping (QSM) and R2* measurements at 7 T. *NeuroImage*, *138*, 43–63. https://doi.org/10.1016/j.neuroimage.2016.05.024

Birkl, C., Birkl-Toeglhofer, A. M., Kames, C., Goessler, W., Haybaeck, J., Fazekas, F., Ropele, S., & Rauscher, A. (2020). The influence of iron oxidation state on quantitative MRI parameters in post mortem human brain. *NeuroImage*, 117080. https://doi.org/10.1016/j.neuroimage.2020.117080

Birkl, C., Carassiti, D., Hussain, F., Langkammer, C., Enzinger, C., Fazekas, F., Schmierer, K., & Ropele, S. (2018). Assessment of ferritin content in multiple sclerosis brains using temperature-induced R* 2 changes. *Magnetic Resonance in Medicine*, *79*(3), 1609–1615. https://doi.org/10.1002/mrm.26780

Braak, H., & Braak, E. (1991). Acta H ' pathologica Neuropathological stageing of Alzheimer-related changes. In *Acta Neuropathol* (Vol. 82).

Bunzeck, N., Singh-Curry, V., Eckart, C., Weiskopf, N., Perry, R. J., Bain, P. G., Düzel, E., & Husain, M. (2013). Motor phenotype and magnetic resonance measures of basal ganglia iron levels in Parkinson's disease. *Parkinsonism and Related Disorders*, *19*(12), 1136–1142. https://doi.org/10.1016/j.parkreldis.2013.08.011

Clarke, W. T., Mougin, O., Driver, I. D., Rua, C., Morgan, A. T., Asghar, M., Clare, S., Francis, S., Wise, R. G., Rodgers, C. T., Carpenter, A., Muir, K., & Bowtell, R. (2020). Multi-site harmonization of 7 tesla MRI neuroimaging protocols. *NeuroImage*, *206*. https://doi.org/10.1016/j.neuroimage.2019.116335

Cornett, C. R., Ehmann, W. D., Wekstein, D. R., & Markesbery, W. R. (1998). Trace elements in Alzheimer's disease pituitary glands. *Biological Trace Element Research*, *62*(1–2), 107–114. https://doi.org/10.1007/BF02820026

Deistung, A., Schweser, F., & Reichenbach, J. R. (2017a). Overview of quantitative susceptibility mapping. *NMR in Biomedicine*, *30*(4). https://doi.org/10.1002/nbm.3569

Deistung, A., Schweser, F., & Reichenbach, J. R. (2017b). Overview of quantitative susceptibility mapping. *NMR in Biomedicine*, *30*(4), e3569.

https://doi.org/10.1002/nbm.3569

Duyn, J. H., & Schenck, J. (2017). Contributions to magnetic susceptibility of brain tissue. *NMR in Biomedicine*, *30*(4), 1–37. https://doi.org/10.1002/nbm.3546

Gilbert, G., Savard, G., Bard, C., & Beaudoin, G. (2012). Quantitative comparison between a multiecho sequence and a single-echo sequence for susceptibility-weighted phase imaging. *Magnetic Resonance Imaging*, *30*(5), 722–730. https://doi.org/10.1016/j.mri.2012.02.008

Graham, M. S., Drobnjak, I., Jenkinson, M., & Zhang, H. (2017). Quantitative assessment of the susceptibility artefact and its interaction with motion in diffusion MRI. *PLoS ONE*, *12*(10), 1–25. https://doi.org/10.1371/journal.pone.0185647

Haacke, E. M., Cheng, N. Y. C., House, M. J., Liu, Q., Neelavalli, J., Ogg, R. J., Khan, A., Ayaz, M., Kirsch, W., & Obenaus, A. (2005). Imaging iron stores in the brain using magnetic resonance imaging. *Magnetic Resonance Imaging*, *23*(1), 1–25. https://doi.org/10.1016/j.mri.2004.10.001

Haacke, E. M., Liu, S., Buch, S., Zheng, W., Wu, D., & Ye, Y. (2015). Quantitative susceptibility mapping: Current status and future directions. In *Magnetic Resonance Imaging* (Vol. 33, Issue 1, pp. 1–25). Elsevier Inc. https://doi.org/10.1016/j.mri.2014.09.004

Hagemeier, J., Ramanathan, M., Schweser, F., Dwyer, M. G., Lin, F., Bergsland, N., Weinstock-Guttman, B., & Zivadinov, R. (2018). Iron-related gene variants and brain iron in multiple sclerosis and healthy individuals. *NeuroImage: Clinical*, *17*(August 2017), 530–540. https://doi.org/10.1016/j.nicl.2017.11.003

Hopp, K., Popescu, B. F. G., McCrea, R. P. E., Harder, S. L., Robinson, C. A., Haacke, M. E., Rajput, A. H., Rajput, A., & Nichol, H. (2010). Brain iron detected by SWI high pass filtered phase calibrated with synchrotron X-ray fluorescence. *Journal of Magnetic*

Resonance Imaging, *31*(6), 1346–1354. https://doi.org/10.1002/jmri.22201

Jack, C. R., Wengenack, T. M., Reyes, D. A., Garwood, M., Curran, G. L., Borowski, B. J., Lin, J., Preboske, G. M., Holasek, S. S., Adriany, G., & Poduslo, J. F. (2005). *Neurobiology of Disease In Vivo Magnetic Resonance Microimaging of Individual Amyloid Plaques in Alzheimer's Transgenic Mice*. https://doi.org/10.1523/JNEUROSCI.2588-05.2005

Lin, P. Y., Chao, T. C., & Wu, M. L. (2015). Quantitative susceptibility mapping of human brain at 3T: A multisite reproducibility study. *American Journal of Neuroradiology*, *36*(3), 467–474. https://doi.org/10.3174/ajnr.A4137

Liu, J., Liu, T., De Rochefort, L., Ledoux, J., Khalidov, I., Chen, W., Tsiouris, A. J., Wisnieff, C., Spincemaille, P., Prince, M. R., & Wang, Y. (2012). Morphology enabled dipole inversion for quantitative susceptibility mapping using structural consistency between the magnitude image and the susceptibility map. *NeuroImage*, *59*(3), 2560–2568. https://doi.org/10.1016/j.neuroimage.2011.08.082

Liu, T., Wisnieff, C., Lou, M., Chen, W., Spincemaille, P., & Wang, Y. (2013). Nonlinear formulation of the magnetic field to source relationship for robust quantitative susceptibility mapping. *Magnetic Resonance in Medicine*, *69*(2), 467–476. https://doi.org/10.1002/mrm.24272

Llera, A., Wolfers, T., Mulders, P., & Beckmann, C. F. (2019). Inter-individual differences in human brain structure and morphology link to variation in demographics and behavior. *ELife*, *8*, 1–20. https://doi.org/10.7554/eLife.44443

MacAulay, N., Keep, R. F., & Zeuthen, T. (2022). Cerebrospinal fluid production by the choroid plexus: a century of barrier research revisited. *Fluids and Barriers of the CNS*, *19*(1), 1–18. https://doi.org/10.1186/s12987-022-00323-1

Mancini, M., Karakuzu, A., Cohen-Adad, J., Cercignani, M., Nichols, T. E., & Stikov, N.

(2020). An interactive meta-analysis of MRI biomarkers of Myelin. *ELife*, *9*, 1–23. https://doi.org/10.7554/eLife.61523

Manjon, J. V., Romero, J. E., & Coupe, P. (2020). *DeepHIPS: A novel Deep Learning based Hippocampus Subfield Segmentation method*. *February*. http://arxiv.org/abs/2001.11789

Mittal, S., Wu, Z., Neelavalli, J., & Haacke, E. M. (2009). Susceptibility-weighted imaging: Technical aspects and clinical applications, part 2. In *American Journal of Neuroradiology* (Vol. 30, Issue 2, pp. 232–252). https://doi.org/10.3174/ajnr.A1461

Möller, H. E., Bossoni, L., Connor, J. R., Crichton, R. R., Does, M. D., Ward, R. J., Zecca, L., Zucca, F. A., & Ronen, I. (2019). Iron, Myelin, and the Brain: Neuroimaging Meets Neurobiology. In *Trends in Neurosciences* (Vol. 42, Issue 6, pp. 384–401). Elsevier Ltd. https://doi.org/10.1016/j.tins.2019.03.009

Mudd, A. T., Fil, J. E., Knight, L. C., Lam, F., Liang, Z. P., & Dilger, R. N. (2018). Early-life iron deficiency reduces brain iron content and alters brain tissue composition despite iron repletion: A neuroimaging assessment. *Nutrients*, *10*(2). https://doi.org/10.3390/nu10020135

Nguyen, T. D., Wen, Y., Du, J., Liu, Z., Gillen, K., Spincemaille, P., Gupta, A., Yang, Q., & Wang, Y. (2020). Quantitative susceptibility mapping of carotid plaques using nonlinear total field inversion: Initial experience in patients with significant carotid stenosis. *Magnetic Resonance in Medicine*. https://doi.org/10.1002/mrm.28227

Papadaki, E., Kavroulakis, E., Kalaitzakis, G., Karageorgou, D., Makrakis, D., Maris, T. G., & Simos, P. G. (2019). Age-related deep white matter changes in myelin and water content: A T2 relaxometry study. *Journal of Magnetic Resonance Imaging*, *50*(5), 1393–1404. https://doi.org/10.1002/jmri.26707

Ravanfar, P., Loi, S. M., Syeda, W. T., Van Rheenen, T. E., Bush, A. I., Desmond, P., Cropley, V. L., Lane, D. J. R., Opazo, C. M., Moffat, B. A., Velakoulis, D., & Pantelis, C. (2021).

Systematic Review: Quantitative Susceptibility Mapping (QSM) of Brain Iron Profile in Neurodegenerative Diseases. *Frontiers in Neuroscience*, *15*(February). https://doi.org/10.3389/fnins.2021.618435

Rua, C., Clarke, W. T., Driver, I. D., Mougin, O., Morgan, A. T., Clare, S., Francis, S., Muir, K., Porter, D., Wise, R., Carpenter, A., Williams, G., Rowe, J. B., Bowtell, R., & Rodgers, C. T. (2020). Multi-centre, multi-vendor reproducibility of 7T QSM and R_2* in the human brain: results from the UK7T study. *BioRxiv*, 2020.04.22.055624. https://doi.org/10.1101/2020.04.22.055624

Rua, C., Clarke, W. T., Driver, I. D., Mougin, O., Morgan, A. T., Clare, S., Francis, S., Muir, K. W., Wise, R. G., Carpenter, T. A., Williams, G. B., Rowe, J. B., Bowtell, R., & Rodgers, C. T. (2020). Multi-centre, multi-vendor reproducibility of 7T QSM and R2* in the human brain: Results from the UK7T study. *NeuroImage*, *223*(April), 117358. https://doi.org/10.1016/j.neuroimage.2020.117358

Schweser, F., Deistung, A., Lehr, B. W., & Reichenbach, J. R. (2011). Quantitative imaging of intrinsic magnetic tissue properties using MRI signal phase: An approach to in vivo brain iron metabolism? *NeuroImage*, *54*(4), 2789–2807. https://doi.org/10.1016/j.neuroimage.2010.10.070

Smith, S. A., Bulte, J. W. M., & Van Zijl, P. C. M. (2009). Direct saturation MRI: Theory and application to imaging brain iron. *Magnetic Resonance in Medicine*. https://doi.org/10.1002/mrm.21980

Sofic, E., Paulus, W., Jellinger, K., Riederer, P., & Youdim, M. B. H. (1991). Selective Increase of Iron in Substantia Nigra Zona Compacta of Parkinsonian Brains. *Journal of Neurochemistry*, *56*(3), 978–982. https://doi.org/10.1111/j.1471-4159.1991.tb02017.x

Van Der Weijden, C. W. J., Biondetti, E., Gutmann, I. W., Dijkstra, H., Mckerchar, R., De Paula Faria, D., De Vries, E. F. J., Meilof, J. F., Dierckx, R. A. J. O., Prevost, V. H., &

Rauscher, A. (2023). Quantitative myelin imaging with MRI and PET: an overview of techniques and their validation status. *Brain*, *146*(4), 1243–1266. https://doi.org/10.1093/brain/awac436

Wang, Y., & Liu, T. (2015). Quantitative susceptibility mapping (QSM): Decoding MRI data for a tissue magnetic biomarker. *Magnetic Resonance in Medicine*, *73*(1), 82–101. https://doi.org/10.1002/mrm.25358

Wisse, L. E. M., Biessels, G. J., Heringa, S. M., Kuijf, H. J., Koek, D. L., Luijten, P. R., & Geerlings, M. I. (2014). Hippocampal subfield volumes at 7T in early Alzheimer's disease and normal aging. *Neurobiology of Aging*, *35*(9), 2039–2045. https://doi.org/10.1016/j.neurobiolaging.2014.02.021

Yablonskiy, D. A., Sukstanskii, A. L., & He, X. (2013). BOLD-based Techniques for Quantifying Brain Haemodynamic and Metabolic Properties - Theoretical models and Experimental Approaches. *NMR Biomed*, *26*(8), 963–986. https://doi.org/10.1002/nbm.2839.BOLD-based

Yao, S., Zhong, Y., Xu, Y., Qin, J., Zhang, N., Zhu, X., & Li, Y. (2017). Quantitative susceptibility mapping reveals an association between brain iron load and depression severity. *Frontiers in Human Neuroscience*, *11*(August), 1–8. https://doi.org/10.3389/fnhum.2017.00442

Yoo, S., Kim, J. won, Schenck, J. F., & Lee, S. K. (2020). Magnetic susceptibility imaging of human habenula at 3 T. *Scientific Reports*, *10*(1), 1–15. https://doi.org/10.1038/s41598-020-75733-y

Yoo, S., Song, H., Kim, S. G., Shim, W. M., & Lee, S. K. (2020). Feasibility of head-tilted brain scan to reduce susceptibility-induced signal loss in the prefrontal cortex in gradient echo-based imaging. *NeuroImage*, *223*(July), 117265. https://doi.org/10.1016/j.neuroimage.2020.117265

Yushkevich, P. A., Pluta, J. B., Wang, H., Xie, L., Ding, S. L., Gertje, E. C., Mancuso, L., Kliot, D., Das, S. R., & Wolk, D. A. (2015). Automated volumetry and regional thickness analysis of hippocampal subfields and medial temporal cortical structures in mild cognitive impairment. *Human Brain Mapping*, *36*(1), 258–287. https://doi.org/10.1002/hbm.22627

CHAPTER FOUR

4.0 MEASUREMENT OF THE SUSCEPTIBILITY AND VOLUME OF HIPPOCAMPAL SUBFIELDS IN ALZHEIMER'S DISEASE PATIENTS

4.1 OUTLINE

In Chapter 3, we established that the susceptibility and volume of the hippocampal subfields can be measured with some degree of reproducibility. Therefore, in this chapter, we aim to translate those findings to the study of Alzheimer's disease (AD), with a focus on detecting changes in the volume and susceptibility of the hippocampus and the whole brain in AD. Our ultimate objective is to determine whether high-resolution volumetry and quantitative susceptibility mapping (QSM) can be utilized as reliable biomarkers for early detection of AD by detecting atrophy and changes in the iron levels of the hippocampal subfields.

In addition to these objectives, we investigate the association between the hippocampal subfields and the concentration of the abnormal proteins Amyloid $Beta_{(1-42)}$ in cerebrospinal fluid and the MoCA score for AD participants.

Previous studies have investigated the correlation between overall hippocampal volume changes in Alzheimer's disease (AD) in comparison to healthy controls (HC) (Olsen et al., 2019, Susanne G. Mueller et al., 2010). Additionally, research has examined alterations in the entire hippocampal susceptibility between AD and HC (Acosta-Cabronero et al., 2013, Schenck et al., 2006, Ates et al., 2019). While previous investigations have explored the dynamics of abnormal cerebrospinal fluid (CSF) proteins (Amyloidβ, tau and phosphor-tau) in individuals with AD (Graham et al., 2017, Stricker et al., 2012) to the best of my knowledge, no prior studies have evaluated changes in the susceptibility and volume of the hippocampal subfields, nor have they related these changes to abnormal CSF protein levels. This area remains understudied, and investigating subfield-specific alterations in the hippocampus could

provide valuable insights into the pathophysiological mechanisms underlying AD and their potential association with CSF biomarkers. Therefore, the present study aims to examining the susceptibility and volume changes within specific hippocampal subfields and their potential correlation with abnormal CSF protein measurements.

To achieve these goals, this chapter first provides an overview of what is known about the development of Alzheimer's disease. We then describe our study, which involved 14 AD patients and 11 healthy controls, and the methods utilized to collect and analyse data.

4.2 DEMENTIA

Dementia is a devastating condition that entails a progressive decline in cognitive or behavioural function, often characterized by the decline in one or more functions, such as short- and long-term memory, abstract thinking, executive processes, language, attention and concentration, and visual processing, or personality changes. This decline usually occurs over years but is eventually severe enough to interfere with day-to-day functioning (American Psychiatric Association, 2000).

Currently, there are approximately 47 million people worldwide living with dementia, and this figure may increase to 131 million by 2050 (Arvanitakis et al., 2019). This chronic and incurable condition has numerous socioeconomic ramifications for patients, their families, caregivers, and society as a whole. As a result, it is critical to identify biomarkers that can help diagnose and monitor the progression of dementia, particularly Alzheimer's disease, which accounts for approximately 60-70% of all cases (Alzheimer's Association, 2021).

4.2.1 CLASSIFICATION OF DEMENTIA

Dementia is a complex and heterogeneous condition that can be classified in various ways. One way to classify dementia is based on its underlying histologic or neuropathological features. For instance, Alzheimer's disease is characterized by the accumulation of beta-amyloid plaques

and tau protein tangles in the brain, while frontotemporal dementia (Brayne et al., 1995, Dening & Sandilyan, 2015). is characterized by the degeneration of the frontal and temporal lobes of the brain (Tiwari et al., 2019).

Another way to classify dementia is by its causal risk factors. Various risk factors have been associated with an increased risk of developing dementia, including cardiovascular disease, genetics, infection, traumatic brain injury, and lifestyle factors such as diet, exercise, and social engagement (Stuss & Levine, 1996, Dening & Sandilyan, 2015).

Dementia can also be classified based on the regions of the brain involved. Different types of dementia affect different areas of the brain, leading to distinct patterns of cognitive impairment and behavioural symptoms. For example, Alzheimer's disease primarily affects the hippocampus and temporal lobes, while frontotemporal dementia primarily affects the frontal and temporal lobes (Brayne et al., 1995, Dening & Sandilyan, 2015)..

Finally, dementia can be classified based on its clinical profile. This approach takes into account the clinical features of dementia, including the type and severity of cognitive impairment, behavioural symptoms, and functional abilities. Different types of dementia may have distinct clinical profiles, which can help clinicians make a more accurate diagnosis and develop appropriate treatment strategies (Brayne et al., 1995).

Overall, understanding the different ways in which dementia can be classified is important for accurate diagnosis and management of the condition. While Alzheimer's disease is the most common cause of dementia, other types of dementia also have distinct features that should be considered in clinical practice. Continued research into the underlying mechanisms of dementia and its subtypes is needed to improve diagnosis, treatment, and prevention strategies for this complex and challenging condition.

4.3 ALZHEIMER'S DISEASE

Alzheimer's disease is a protein-conformational disease (PCD) that is accompanied by progressive neurodegeneration, the presence of neurofibrillary tangles and the accumulation of amyloid plaques.(Tiwari et al., 2019). Post mortem studies have shown that AD damages the para-hippocampal regions which are responsible for forming new memories and the pathology subsequently spreads from that region, eventually causing cortical atrophy and ventricular enlargement, thereby reducing the size of the brain by almost 35% (Farfara et al., 2008, Alves et al., 2012).

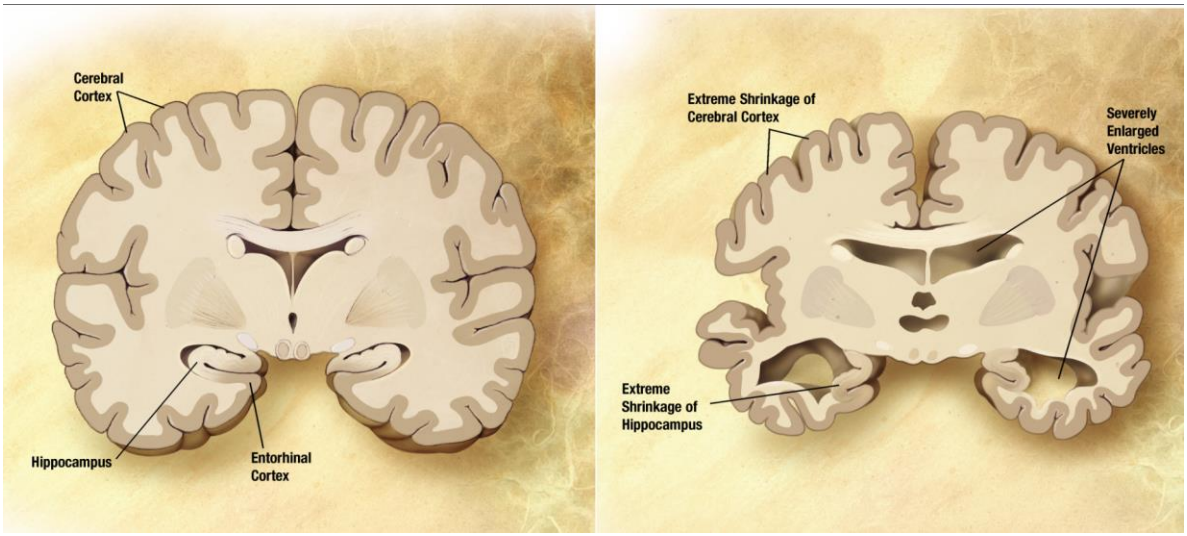


Figure 4.1: Comparison between a healthy brain and a brain with Alzheimer's disease. In AD the cortex shrinks, especially in the hippocampal region which is responsible for forming new memories. The ventricles which are fluid filled cavities in the brain, consequently enlarge. Taken from https://commons.wikimedia.org/wiki/File:Alzheimer%27s_disease_brain_comparison.jpg

As stated above, AD is one of the most common causes of dementia in the world. In 2021 there were over 900,000 people with dementia in the UK (Alzheimer's Society, 2023), meaning that 1 in every 14 people over the age of 65 has AD-related dementia and by the year 2040, that figure will rise to 1.6 million if no solution is found to reduce this rate (Alzheimer's Society, 2023). In the United States, more that 6 million people have dementia caused by AD and it is ranked as the seventh leading cause of death in the United States (Alzheimer's Association, 2023).

AD has various cognitive symptoms, including loss of memory, difficulties in learning, changes in behaviour, which affect the day to day activity of the patient, ultimately making them dependent on others to carry out their tasks, putting a financial and psychological burden on their family or community (Merriam et al., 1988)(El-Hayek et al., 2019). Therefore, there are many benefits associated with early diagnosis of AD: it assists the patient, their family and carers in advanced planning of health and financial matters, and an early diagnosis and early implementation of therapy (intervention), can modify the course of the disease before neurodegeneration/irreversible damage occurs. Therefore, it is important to find a biomarker for early diagnosis, to provide an opportunity to modify the course of the disease, improve the patient's life and reduce the socioeconomic stress experienced by their carers.

4.4 MRI AS A BIOMAKER FOR EARLY ALZHEIMER'S DISEASE

The importance of clinical and neuropsychological assessment of AD cannot be overemphasized in determining the prognosis of patient at the chronic stage of the disease before it becomes full-blown dementia. Recently Amyloidβ, tau-pathology and neurodegeneration (ATN categories) have been use to classify AD into stages (Jellinger A, 2018, Grøntvedt et al., 2020). So far Amyloidβ and tau-pathology measurements in the cerebrospinal fluid (CSF) give the greatest accuracy in the diagnosis of AD, though they do not directly reflect the loss in neurons (Gulisano et al., 2018). Furthermore, these Amyloidβ and tau examinations involve invasive lumbar punctures, or utilisation of nuclear medicine imaging that is very expensive. Hence there is a need for a less expensive, non-invasive imaging technique for diagnosis of this destructive disease: magnetic resonance imaging has the potential to provide early diagnosis of AD.

The deposition of iron has been implicated in many neurological disorders and diseases. Ferritin and neuromelanin are usually responsible for the accumulation of iron in the ageing

process in different brain regions, with possible neurotoxic consequences, such as oxidative damage and cell death (Betts et al., 2016). We cannot conclude that the iron is the primary cause of AD, but the disease-specific proteins, Amyloidβ and tau, are known to be associated with elevated iron content, hence it is suggested that an overload of iron might lead to the aggregation and neurotoxicity of Amyloidβ (Taniguchi et al., 2014). Studies have shown that there is an increase in the level of ferritin in the CSF, which can affect AD progression (Ayton et al., 2015, Kuiper et al., 1994). Therefore, the measurement of iron in the hippocampus (the brain region most affected by AD in the brain) should be investigated as a potential diagnostic tool and biomarker for AD.

At high field (7T and above) MRI can provide images of high contrast and high spatial resolution, particularly for magnetic susceptibility measurements (Wharton & Bowtell, 2010, Zeineh et al., 2015). Here, we therefore exploit the sensitivity of 7T MRI in measuring the effect of AD on the volume and susceptibility of the subfields of the hippocampus.

4.5 METHODS

4.5.1 STAFF ROLE AND PARTICIPANTS

As the MRI physicist responsible for the neuroimaging aspects of this study, my role was to ensure the successful acquisition and analysis of the MRI data that was used in investigating the hippocampus and its subfields. I took on the responsibility of overseeing the entire process of image acquisition, ensuring that it adhered to the best of my ability the highest standards of quality and consistency.

The process of image-acquisition required precise positioning of participants and selection of parameter settings to obtain high-resolution images of the brain structures of interest. The image analysis phase was equally critical in unravelling the structural and microstructural properties of the hippocampus. Using image analysis software, I processed the MRI data to

delineate the hippocampus and its subfields. This involved segmenting the hippocampus into its various subfields and then evaluating the volume and magnetic susceptibility of each subfield.

While my role focused on the neuroimaging aspects, I also worked closely with study team at NUH to complement the imaging with cognitive assessments, blood tests, questionnaires, and physical examinations. The team, consisting of Trained Assistant Psychologists, Research Practitioners, Clinical Fellows, and Consultant Neurologists, played an integral role in evaluating participants' cognitive function, health status, and relevant clinical parameters.

De-identification of data was carried out to safeguard the confidentiality and privacy of the participants. The de-identified data was securely shared across the collaborating study sites, facilitating comprehensive data analysis.

24 participants (13 AD patients and 11 healthy controls of which 2 AD patients were excluded due to motion) aged between 40 and 74 years, were recruited. All participants provided informed consent prior to the study, which was a requirement to be included in the study. All Alzheimer's disease participants had been clinically diagnosed with the disease according to the National Institute on Aging and Alzheimer's Association (NIA-AA) criteria (Jack et al., 2018) and the healthy controls were within 1.5 standard deviations of normal in all tests. Participants were excluded if they lacked the mental capacity to provide consent, did not speak English before age 5 years (because of the language components of some of the cognitive tests), took prescribed medicine that could affect their cognition or had a learning disability, major depression, schizophrenia, a concentration span of less than 30 minutes, a medical implant or other factor not compatible with MRI, or if they were pregnant.

The Montreal Cognitive Assessment (MoCA) was administered by a trained Assistant Psychologist. This assessment includes a variety of cognitive tests assessing memory (immediate/delayed recall, un-cued/cued recall, and recognition), attention, language and

visuospatial abilities. The MoCA was divided into the cognitive domains: orientation, language, executive function, visuospatial ability and memory (uncued, recognition, category cue).

It provides a vast amount of information regarding an individual's cognition, as it incorporates domain specific tasks. The MoCA was developed as a brief screening tool for Mild Cognitive Impairment (MCI) (Nasreddine et al., 2005). MoCA is a valuable screening tool because it can assess performance across various cognitive domains, providing insights into potential specific dementia syndromes. The cognitive domains covered by the MoCA include memory, visuospatial abilities, executive function, attention, language, and orientation, which are similar to the domains assessed by the Uniform Data Set (UDS). A cutoff score of 26 on the MoCA has demonstrated good specificity for mild cognitive impairment (MCI) and good sensitivity for differentiating between MCI, Alzheimer's disease, and healthy controls (Nasreddine et al., 2005).

In addition to the MoCA test, all AD patients had CSF drawn via lumbar puncture as part of their clinical assessment. The concentration of the 42 amino acid form of β amyloid in CSF (CSF Amyloidβ1-42), which is a biochemical marker for Alzheimer's disease (AD), was assessed to confirm the diagnosis of AD. The assessment of CSF Amyloidβ1-42 concentration is useful for differentiating AD from other forms of dementia, as the decrease in CSF Amyloidβ1-42 concentration is specific to AD and is thought to reflect the deposition of amyloid plaques in the brain.

The CSF measurement cut off for the levels of Amyloidβ1-42, total tau, and Thr181-phosphorylated tau in this study were established based on reference laboratory ranges, which are widely accepted as standards for the diagnosis and management of neurological conditions. Specifically, the CSF Amyloidβ1-42 range was 627 – 1322 pg/ml, the total tau range was 146

- 595 pg/ml, and the Thr181-phosphorylated tau range was below 68 pg/ml, as previously reported (Hosseini, 2022).

These cut-off values have been validated in numerous studies, and are used to differentiate between normal and abnormal levels of these proteins in the CSF (Hosseini, 2022

Hampel & Blennow, 2004, Randall et al., 2013). For instance, a decrease in Amyloidβ1-42 levels and an increase in total tau and phosphorylated tau levels are characteristic of Alzheimer's disease and other dementias. Conversely, a decrease in total tau levels and an increase in phosphorylated tau levels can indicate a variety of other neurological conditions, such as traumatic brain injury, stroke, or multiple sclerosis (Siderowf et al., 2010).

Measuring these CSF biomarkers is a critical tool in the diagnosis, prognosis, and monitoring of neurological conditions. However, it is important to note that CSF analysis alone cannot provide a definitive diagnosis, and must be interpreted in the context of clinical symptoms, neuroimaging, and other diagnostic tests.

4.5.2 IMAGING PROTOCOL

The participants were scanned on a whole-body Philips Achieva 7T system with a Nova Medical (Wilmington MA, USA) single-channel transmit, 32-channel receive (1Tx32Rx) head coil at the Sir Peter Mansfield Imaging Centre, University of Nottingham.

The primary image data-set acquired for susceptibility mapping was a whole-brain 3D single-echo GRE scan, with an echo time (TE) of 20 ms, repetition time (TR) of 31 ms, 3D matrix dimensions, 224 × 224 × 157 mm^3 and voxel dimensions of 0.7 ×0.7 ×0.7 mm^3. Data acquisition for this sequence took 9 minutes and 13 seconds

A T_1-weighted PSIR volume data set was also acquired for each subject using the following acquisition parameters: inversion times (TI) of 725/2150 ms; TE= 3.1 ms; TR= 6.9 ms; Field of view 192 × 183 × 157 mm^3; 0.55 × 0.55 ×0.55 mm^3 voxel size; receiver bandwidth of 300 Hz; the total time for this scan was 12:25 minutes

T_2-weighted images spanning the hippocampus were also acquired from the subject. The acquisition parameters were as follows: partial brain TSE sequence, with a resolution of 0.38 × 0.39 ×1.5 mm^3, field of view 224 × 224 × 64 mm^3, TR = 5900ms, TE = 117 ms and receiver bandwidth of 155 Hz. The time for this sequence was 4:43 minutes. The slice orientation was chosen so that the slices ran orthogonal to the hippocampus' longest axis.

4.5.3 IMAGE PROCESSING AND ANALYSIS

The GRE phase and magnitude data were processed using QSMbox, a software tool developed specifically for quantitative susceptibility mapping (QSM) analysis (Acosta-Cabronero et al., 2018). The QSM technique is used to produce a susceptibility map of the entire brain, which can provide valuable insights into the structural and functional changes that occur in different brain regions (Fig 4.2). To ensure the accuracy of the QSM results, the susceptibility measurements were referenced to the average across the scanned volume of the brain, rather than using a tissue or CSF reference, which was shown in Chapter 3 to increase variability in the QSM values in the hippocampal subfields.

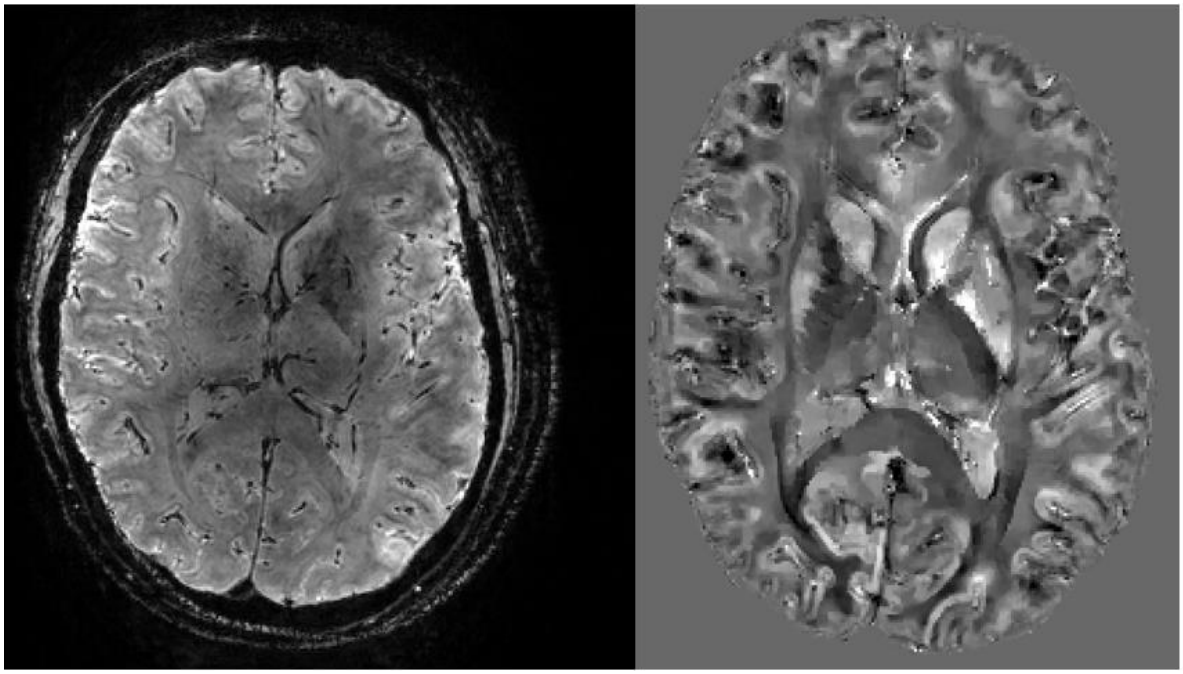


Figure 4.2: T2-weighted image (left) and corresponding quantitative susceptibility map (QSM) (right) obtained for one of the participants in the study. The QSM data was generated using QSMbox (Acosta-Cabronero et al., 2018) to produce a susceptibility map spanning the whole brain*

We utilized the ASHS tool to segment the hippocampus from the PSIR and T2-weighted images, using the ashs_atlas_umcutrecht_7t_20170810 atlas (provided by the NeuroImaging Tools and Resources Collaboratory (NITRC) (Wisse et al., 2016). The atlas segments the hippocampus into eight ROI/subfields, including Cornu Ammonis (CA) areas: CA1, CA2, and CA3, hippocampal tail (TAIL), Dentate Gyrus (DG), Subiculum (SUB), CYST, and Entorhinal Cortex (ERC). We evaluated the average susceptibility (in ppm) and volume (in mm^3) of each subfield for each scan. However, we combined the CA1-3 values into a single CA measurement because the volumes of CA2 and CA3 regions were found to be too small to produce reliable susceptibility values. Additionally, we omitted CYST because its volume was very small and was not detected in almost all of the participants.

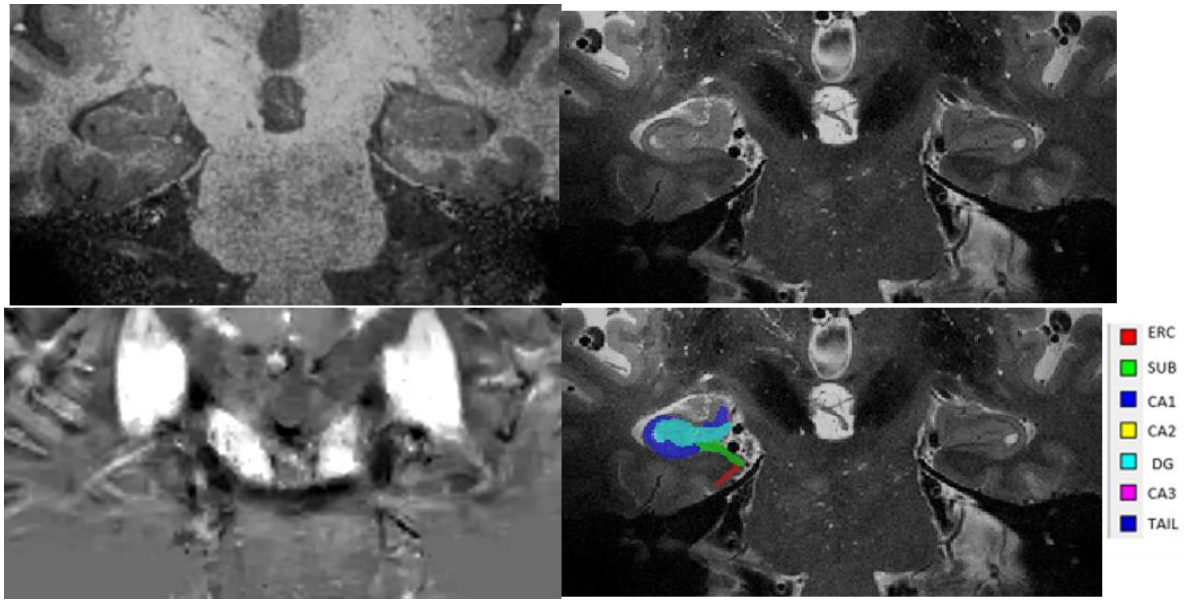


Figure 4.3: Coronal view of MRI images obtained for one of the participants in the study. The images include PSIR, T2-weighted, and QSM images, with the segmentation of the hippocampus overlaid on the T2-weighted image.

4.4.2.1 PERCENTAGE VOLUME OF THE HIPPOCAMPUS SUBFIELDS

To account for individual differences in brain size, we not only reported the raw volumes for each hippocampal subfield but also expressed the volumes as a percentage of the whole brain volume, which we refer to as the relative volume of subfields. This was achieved by extracting

the mask and volume of the whole brain (including the CSF and cerebellum) as shown in Fig 4.4 from the PSIR image. Expressing the volumes as a percentage provided a more reliable result, as the relative volume is largely independent of the size of the brain. This analysis allowed us to investigate whether any specific subfield was disproportionately affected in relation to the rest of the hippocampus.

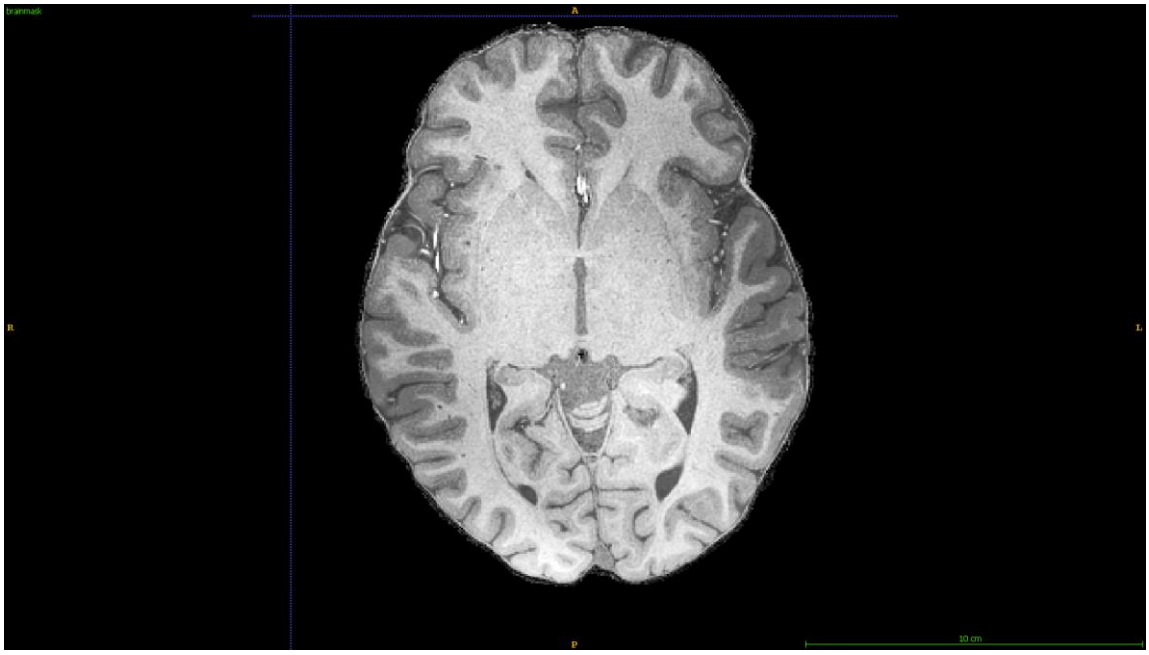


Figure 4.4: Showing the whole brain segmentation of the PSIR image for one slice in an image of one of the participants. Whole brain volume was used for scaling the volume of the hippocampal subfields into a percentage volume.

4.5.3 STATISTICAL ANALYSIS

The statistical analysis was carried out using one-way ANOVA and bivariate correlation analysis in SPSS (version 27) for comparison between the control and AD patients for the subfields CA, ERC, TAIL, DG, and SUB. The analysis aimed to identify any significant differences between the two groups and to find out how the volume and susceptibility in these regions of interest (ROIs) correlate with CSF Amyloidβ1-42 and MoCA scores for the Alzheimer's disease participants. For greater sensitivity, the data from the left and right hippocampus subfields were combined in this analysis. As mentioned earlier, the CA was considered as the combination of the CA1, CA2 and CA3 output of ASHS. The number of

voxels in each combined ROI was taken into account by calculating the weighted average susceptibility for the summed ROI.

Moreover, to assess the relationship between the MoCA scores and hippocampal volume and susceptibility, we performed a correlation analysis within the AD group. The significance level was set at $p < 0.05$ for all statistical tests. The results of the statistical analysis were plotted to visualize the data and trends.

The Bonferroni correction was employed as a statistical method in our analysis. This correction accounts for multiple comparisons by adjusting the significance level to maintain a controlled familywise error rate. By dividing the chosen significance level (alpha) by the number of comparisons conducted, the Bonferroni correction reduces the risk of observing false positives, ensuring that the overall probability of making a type I error remains within acceptable limits. This approach is particularly valuable when conducting numerous statistical tests simultaneously, guarding against the inflation of false positives. In our study, the Bonferroni correction was implemented to enhance the robustness of our findings and provide a more accurate representation of statistically significant results.

4.6 RESULTS

Out of all the participants recruited to this study, one of the AD participants could not be scanned as he was claustrophobic and 2 of the AD participants' scans could not be analysed due to prominent motion artefacts, which led to mis-registration of the hippocampal subfields. Hence, the final results are given for 11 AD patients and 11 controls.

Figure 4.5 compares the average whole brain volumes in the AD group as compared to the healthy controls. The average value is lower for AD patients, but the difference with healthy controls is not significant.

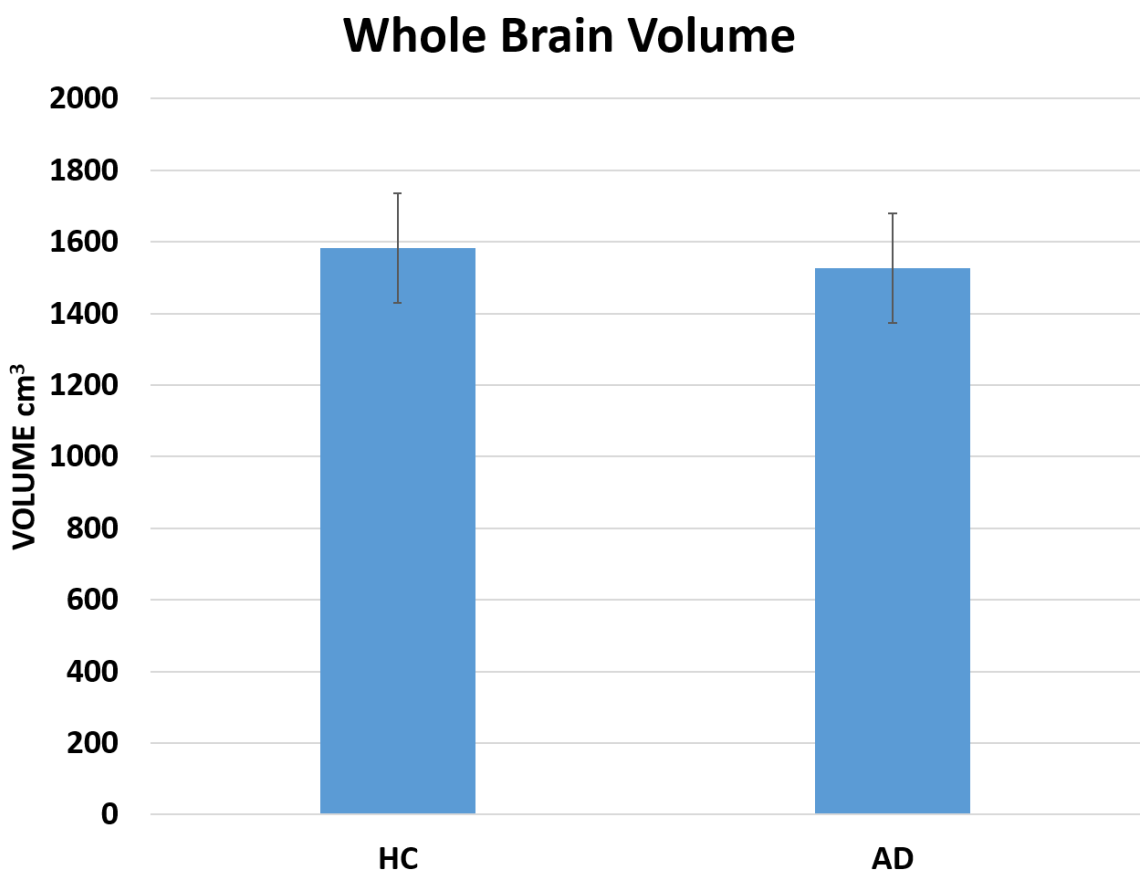


Figure 4.5: Showing the average volume of the whole brain for 11 Alzheimer's disease (AD) participants and 11 healthy controls. Error bars show the standard deviation across participants in each group. The difference in average volume between the AD patients and controls was not statistically significant.

Figure 4.6 shows that there is a significant reduction in the relative volume and the absolute volume of the whole hippocampus for the AD group ($p < 0.001$). The susceptibility for the whole hippocampus was unchanged in the Alzheimer's disease patients.

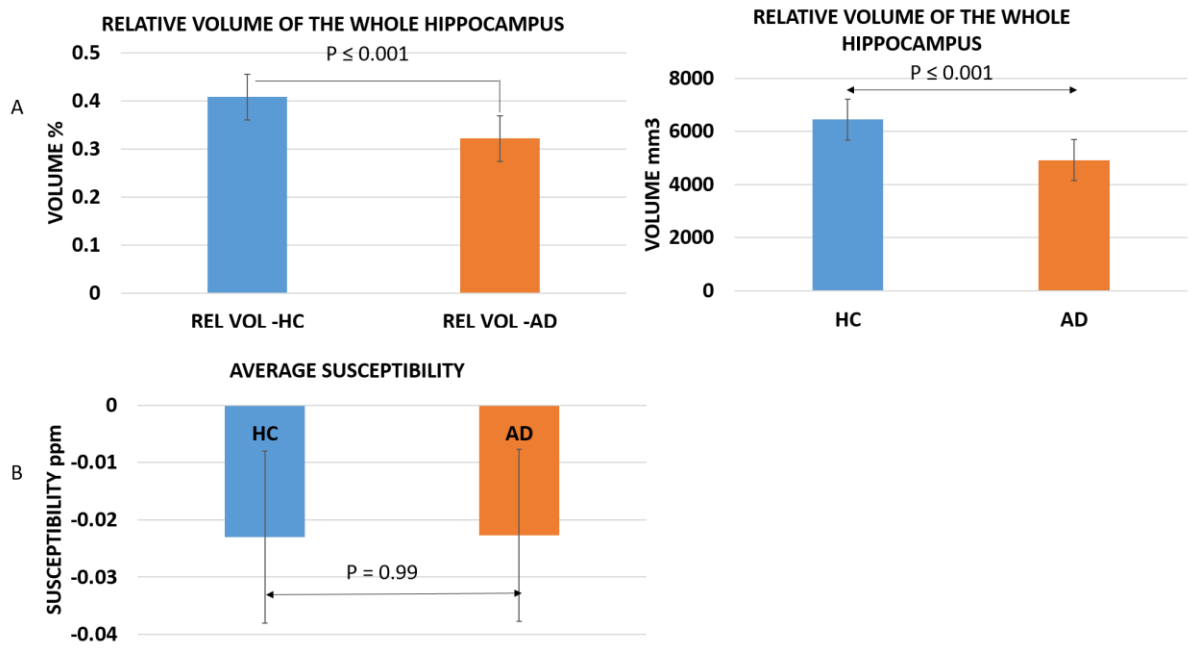


Figure 4. 6: Showing A) the average percentage volume and the absolute volume of the whole hippocampus for AD participants and healthy controls (HC). B) The average susceptibility of the whole hippocampus for AD participants and HCs. There was a statistically significant difference between the AD and controls for the volume of the hippocampus, but no difference statistically for the susceptibility.

Figure 4.7 and Table 4.1 show that there was reduction in the relative volume of all subfields of the hippocampus in AD patients, and this difference was statistically significant ($p < 0.001$) for the ERC, DG and TAIL, and ($p = 0.006$) for the CA (CA1+CA2+CA3), but not for the SUB ($p = 0.252$). A statistically significant difference in the susceptibility was found only in the DG ($p = 0.045$), which was more diamagnetic in AD patients.

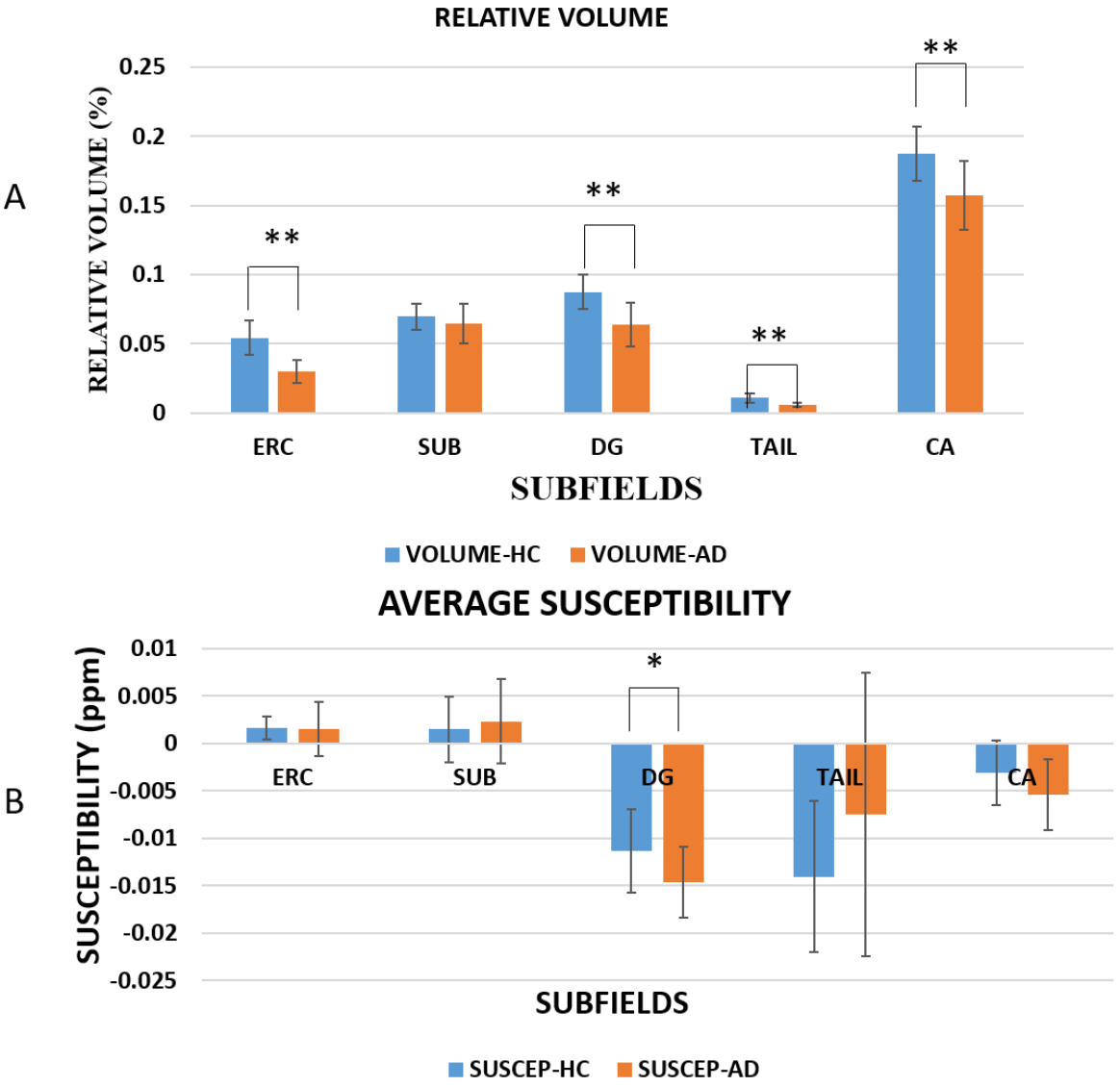


Figure 4.7: A) The average relative volumes of the hippocampal subfields in AD patients and healthy controls (as a percentage of the whole brain volume) B) the average susceptibility values for the AD and HC. The error bars represent the standard deviation of the measurements. means comparison of values for AD and HC yields a statistically significant difference with $p \leq 0.05$, ** means $p < 0.01$ while no sign means that the values are not significantly different.*

			N	Mean	Std. Deviation	Std. Error	F	Sig.
ERC_VOL	AD		11	0.030	0.008	0.002	31.494	0.000
	HC		11	0.054	0.012	0.004		
	Total		22	0.042	0.016	0.003		
SUB_VOL	AD		11	0.065	0.014	0.004	1.392	0.252
	HC		11	0.071	0.009	0.003		
	Total		22	0.068	0.012	0.003		
DG_VOL	AD		11	0.064	0.016	0.005	14.107	0.001
	HC		11	0.087	0.012	0.004		
	Total		22	0.075	0.018	0.004		
TAIL_VOL	AD		11	0.006	0.002	0.001	14.483	0.001
	HC		11	0.010	0.003	0.001		
	Total		22	0.008	0.003	0.001		
CA_VOL	AD		11	0.157	0.025	0.008	9.515	0.006
	HC		11	0.187	0.019	0.006		
	Total		22	0.172	0.026	0.006		
ERC_SUS	AD		11	0.002	0.003	0.001	0.027	0.871
	HC		11	0.001	0.001	0.000		
	Total		22	0.001	0.002	0.000		
SUB_SUS	AD		11	0.002	0.004	0.001	0.09	0.768
	HC		11	0.002	0.003	0.001		
	Total		22	0.002	0.004	0.001		
DG_SUS	AD		11	-0.015	0.004	0.001	4.591	0.045
	HC		11	-0.011	0.004	0.001		
	Total		22	-0.013	0.004	0.001		
TAIL_SUS	AD		11	-0.008	0.015	0.004	0.836	0.371
	HC		11	-0.012	0.009	0.003		
	Total		22	-0.010	0.012	0.003		
CA_SUS	AD		11	-0.005	0.004	0.001	3.426	0.079
	HC		11	-0.002	0.004	0.001		
	Total		22	-0.004	0.004	0.001		

Table 4.1: The results of applying a one-way ANOVA statistical test for differences between AD patients and HC in measurements of the volume and susceptibility of each hippocampal subfield were obtained. It's important to note that the p-values reported in our analysis were subjected to Least Significant Difference (LSD) multiple comparison correction to address the risk of Type I errors. The mean, standard deviation, and standard errors for each measurement are shown for the AD and HC groups, as well as for all 22 participants.

Figure 4.8 and Table 4.2 illustrate the relationship between the absolute volume and the relative volume of the whole hippocampus and either CSF Amyloidβ1-42 concentration or MoCA score. Figure 4.8 shows scatter plots: MoCA score is shown for all subjects while CSF Amyloidβ1-42 values were only measured on the AD participants. In no case did the correlation reach statistical significance.

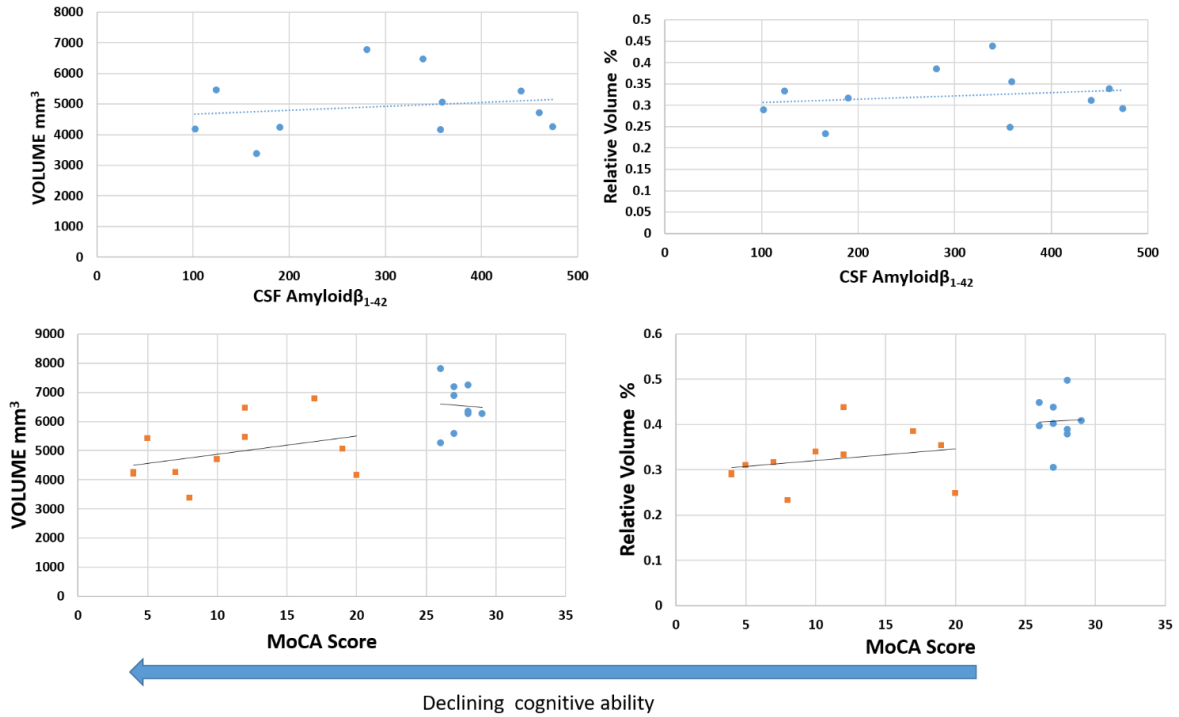


Figure 4. 8: Scatter plots showing the relationship between the absolute volume and relative volume of the whole hippocampus and the concentration of CSF Amyloidβ1-42 or MoCA Score, with the linear relationship on the trend line indicated. Orange circles represent measurements from AD participants, while blue circles show HC values. CSF Amyloidβ1-42 measurements were only made on AD participants.

Correlations of the whole Hippocampus							
		CSF_Amyloidβ	ABSOLUTE-VOLUME	PERCENTAGE-VOLUME	SUSCEPTIBLITY	AGE	MoCA
CSF_Amyloidβ	Correlation Coefficient	1.000	0.145	0.173	0.018	0.257	0.018
	Sig. (2-tailed)		0.670	0.612	0.958	0.446	0.957
	N	11	11	11	11	11	11
ABSOLUTE-VOLUME	Correlation Coefficient	0.145	1.000	.873**	0.336	-0.009	0.279
	Sig. (2-tailed)	0.670		0.000	0.312	0.979	0.407
	N	11	11	11	11	11	11
PERCENTAGE-VOLUME	Correlation Coefficient	0.173	.873**	1.000	0.418	0.321	0.397
	Sig. (2-tailed)	0.612	0.000		0.201	0.336	0.226
	N	11	11	11	11	11	11
SUSCEPTIBLITY	Correlation Coefficient	0.018	0.336	0.418	1.000	0.569	.772**
	Sig. (2-tailed)	0.958	0.312	0.201		0.068	0.005
	N	11	11	11	11	11	11
AGE	Correlation Coefficient	0.257	-0.009	0.321	0.569	1.000	.636*
	Sig. (2-tailed)	0.446	0.979	0.336	0.068		0.035
	N	11	11	11	11	11	11
MoCA	Correlation Coefficient	0.018	0.279	0.397	.772**	0.636	1.000
	Sig. (2-tailed)	0.957	0.407	0.226	0.005	0.335	
	N	11	11	11	11	11	11
**. Correlation is significant at the 0.01 level (2-tailed).							
*. Correlation is significant at the 0.05 level (2-tailed).							

Table 4.2: Linear regression analysis to characterise the correlation between the value of absolute volume, relative volume and susceptibility with CSF Amyloidβ1-42 /MoCA score for AD participants, only with age as covariant. The Pearson correlation is reported for the 11 AD participant

Figure 4.9 and Table 4.2 characterise the relationship between the susceptibility of the whole hippocampus and the CSF Amyloidβ1-42 concentration and MoCA score for the AD patients. The relationship between susceptibility and MoCA score is also shown for the healthy controls in Fig. 4.9. Table 4.2 shows that there was a strong relationship between the average susceptibility of the whole hippocampus and MoCA score in the data from the AD participants, and that this relationship attained statistical significance with a correlation value of $R^2 = 0.77$ and a p-value of 0.006 with the age of the participant as a covariant. There was no significant correlation between susceptibility of the whole hippocampus and the CSF Amyloidβ1-42 concentration.

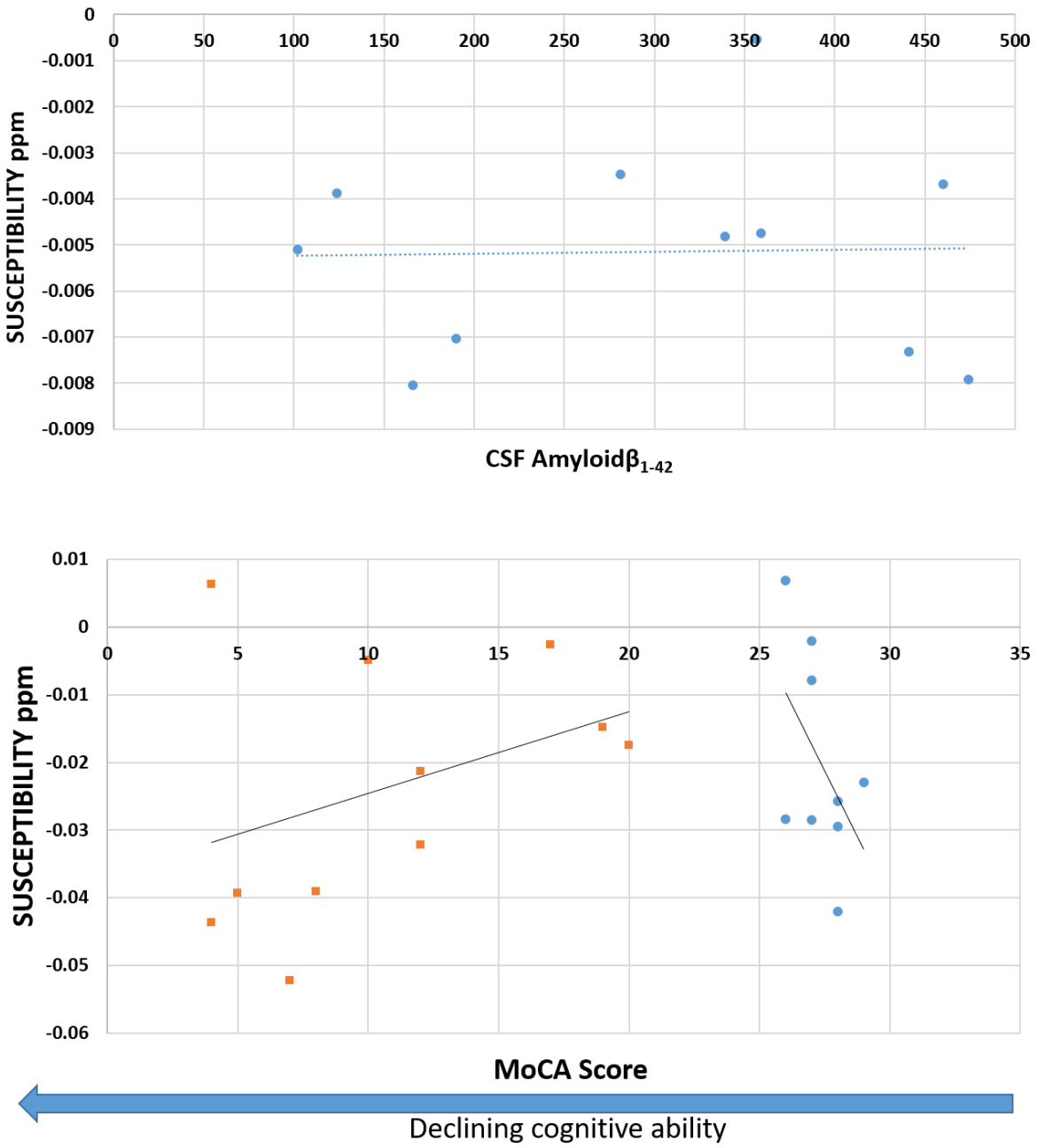


Figure 4 9: (Top) Scatter plot showing the relationship between the susceptibility of the whole hippocampus and CSF Amyloidβ1-42 concentration in AD participants.(Bottom) Scatter plot showing the relationship between the susceptibility of the whole hippocampus the MoCA score in AD participants and healthy controls.. The orange squares represent the values for the AD participants and the blue circles show values for the healthy controls

Fig 4.10 (A and B) and Table 4.3 summarize the relationship between the MoCA score and the relative volume/susceptibility of each sub-field separately in the Alzheimer's disease participants. Similarly Fig 4.11 (A and B) and Table 4.3 summarize the relationship between

the CSF Amyloidβ1-42 concentration and the relative volume/susceptibility of each hippocampal sub-field separately in the Alzheimer's disease participants.

The results show that the subfield volumes generally decrease with decreasing MoCA score and decreasing value of CSF Amyloidβ1-42. For the variation of relative volume with MoCA score, all regions showed $R^2 \geq 0.1$ but only in the TAIL did the trend reach significance (R^2= 0.709 and p =0.014). In the case of CSF Amyloidβ1-42 concentration, only the correlation with the relative volume of Entorhinal Cortex (ERC) and CSF Amyloidβ1-42 was statistically significant R^2= 0.657 and p =0.003.

The relationships between the subfield susceptibility values and CSF Amyloidβ1-42 showed no clear trends but there was a correlation between susceptibility and the MoCA score for the AD patients. This correlation was significant in the DG and CA ($R^2 \geq 0.7$ and $p \leq 0.05$).

Correlations for the hippocampus subfields

		ERC_VOL	SUB_VOL	DG_VOL	TAIL_VOL	CA_VOL	ERC_SUS	SUB_SUS	DG_SUS	TAIL_SUS	CA_SUS	MoCA	CSF
MoCA	Pearson Correlation	0.333	0.137	0.197	.709*	0.238	-0.476	-0.087	.740**	0.225	.734*	1	0.093
	Sig. (2-tailed)	0.316	0.687	0.562	0.014	0.482	0.139	0.800	0.009	0.506	0.010		0.787
	N	11	11	11	11	11	11	11	11	11	11	11	11
CSF Amyloidβ1-42	Pearson Correlation	.788**	0.060	0.150	0.335	0.005	0.068	-0.307	0.257	-0.052	0.003	0.093	1
	Sig. (2-tailed)	0.004	0.861	0.661	0.314	0.988	0.843	0.359	0.446	0.879	0.993	0.787	
	N	11	11	11	11	11	11	11	11	11	11	11	11

*. Correlation is significant at the 0.05 level (2-tailed).

**. Correlation is significant at the 0.01 level (2-tailed).

Table 4.3: Linear correlation analysis of the value of relative volume or susceptibility of each hippocampal subfield with CSF Amyloidβ1-42 concentration or MoCA score for the Alzheimer disease participants. . means that a statistically significant correlation with $p \leq 0.05$ is found, while ** means that $p < 0.01$.*

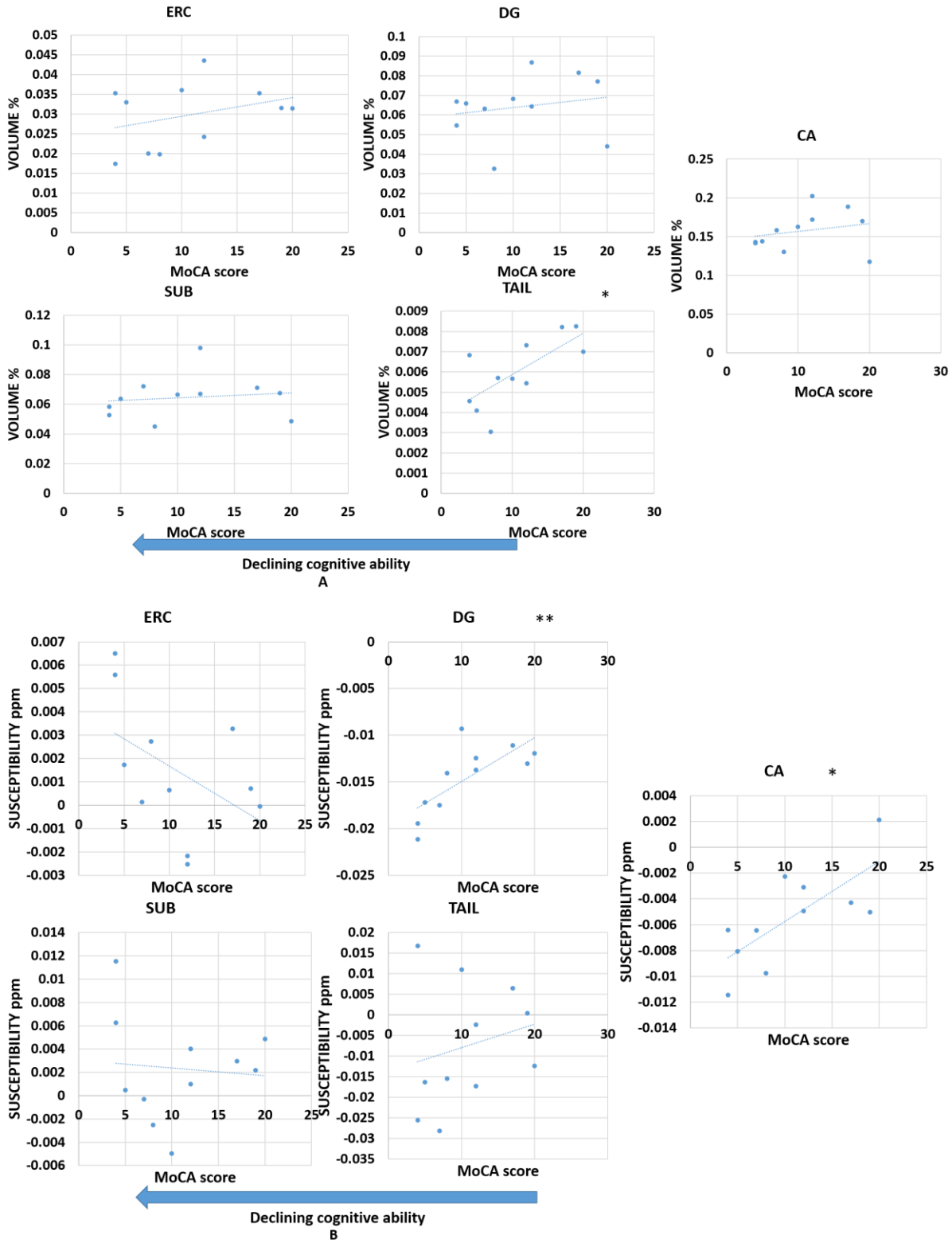


*Figure 4. 10: Scatter plots showing the relationship between (A) relative volume (%) or (B) susceptibility (ppm) of the hippocampal subfields of AD participants and the value of MoCA score. Linear fits are indicated by the trend lines. * means they have $p \leq 0.05$, ** $p < 0.01$ and no sign means they are not significant.*

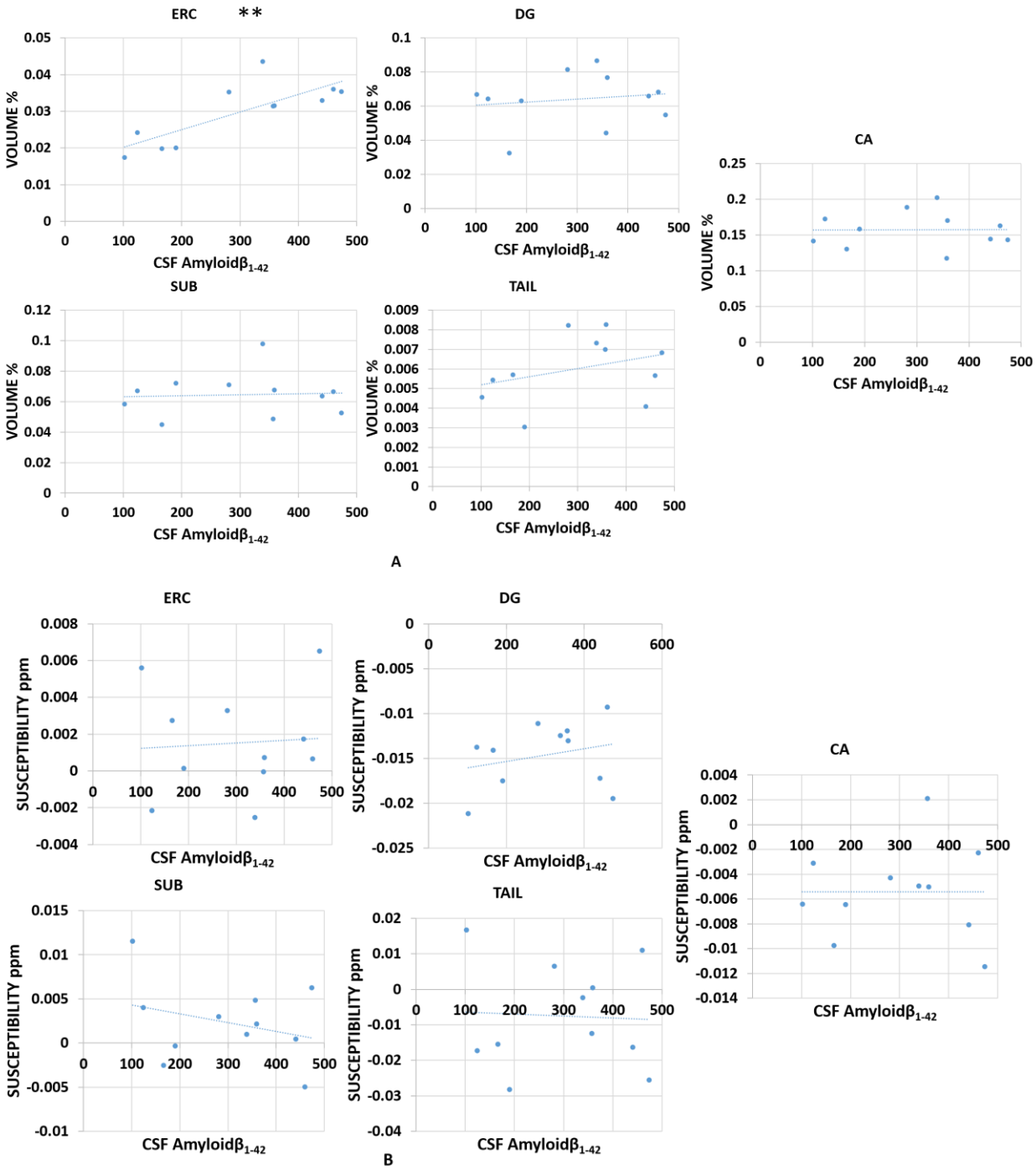


*Figure 4.11: Scatter plots showing the relationship between (A) relative volume (%) or (B) susceptibility (ppm) of the hippocampal subfields of AD participants and the concentration of CSF Amyloidβ1-42. in pg/ml. Linear fits are indicated by the trend lines. * means they have $p \leq 0.05$, ** $p < 0.01$ and no sign means they are not significant.*

4.7 DISCUSSION

In the study, we examined the use of ultra-high field MRI at 7T including PSIR,T_2-Weighted and T2* images in patients with biological Amyloid-status Alzheimer's disease who did not

have evidence of hippocampal atrophy on their clinical MRI at 3T (i.e. met classification of A+T-N- or A+T+N- criteria) (Jack et al., 2018) as a new biomarker for making the diagnosis of AD during the prodromal phase. We measured and assessed the changes in volume/susceptibility of the hippocampus and its subfields at 7T for Alzheimer's disease patient and healthy control also how those changes relate to the levels of Amyloid in the CSF in patients with AD.

In our statistical analysis, in Table 4.2, we used age as a covariate to determine its potential influence on the study outcomes. Our analysis revealed that age did not yield any statistically significant effects on the results. This indicates that age does not impact the measured variables as assessed in our dataset.

Furthermore, we also employed sex as a covariate in our investigation. This consideration was particularly important, given that males typically tend to have larger head and brain sizes compared to their female counterparts. Our findings indicated that sex significantly influenced the absolute volume measurements. However, upon implementing the Total Intracranial Volume (TIV) correction, the previously observed significance of sex was mitigated. As a result, for the majority of our analyses, we primarily relied on the TIV-corrected volume presented in percentage terms.

By accounting for age and sex as covariates and emphasizing the TIV-corrected volume in our analyses, we aimed to enhance the accuracy and reliability of our results, ensuring that any observed variations were attributed to the variables of interest rather than potential confounding factors.

As compared with age-matched controls, we found that there was a significant volume loss involving the all the subfield of the hippocampus except for the SUB. A p-value of $p \leq 0.001$ was observed in ERC, DG, Hippocampus tail and CA subfields. Further, the lower volume of ERC subfield in percipients with prodromal AD had a linear correlation with the measured

value of Amyloid$\beta_{1\text{-}42}$ in the CSF (R^2= 0.542 and p = 0.0011). In this pilot study, the volume loss in the other hippocampal subfields showed a trend towards the correlation with the CSF Amyloid$\beta_{1\text{-}42}$, but did not reach statistical significance. The presented results have undergone Bonferroni correction, to limit the risk of encountering false positive outcomes. This correction plays a crucial role in maintaining the reliability of our findings by reducing the likelihood of identifying significant effects purely by chance.

Absolute hippocampal volume loss in AD has been reported in other neuroimaging studies using standard MRI at 3T and 1.5T (Yushkevich et al., 2015, Schuff et al., 2009, Vijayakumar & Vijayakumar, 2013. Here, we have examined patients with prodromal AD who did not have significant total volume loss of the brain as shown in Fig 4.6 and 4.6, when compared with age-matched healthy controls ($p \leq 0.001$; Figure 4.6). The use of 7T MRI identified the hippocampal volume loss in the absence of total brain volume loss in patients with prodromal AD. This finding supports the superiority of 7T MRI over the standard MRI (at 3 or 1.5T) as a potential biomarker for an early identification of atrophy to aid the diagnosis of AD.

It has been previously reported that the level of CSF Amyloid$\beta_{1\text{-}42}$ declines during the preclinical stage of AD (Haapalinna et al., 2016), and correlates with delays in memory tasks in patients with Mild Cognitive Impairment (MCI) (Haldenwanger et al., 2010). In our study of patients with Amyloid-positive prodromal AD, we have found significant associations between the ERC volume loss and a decrease in the level of CSF Amyloid$\beta_{1\text{-}42}$ Fig 4.11. The ERC is responsible for memory, navigation and perception of time (Tsao et al., 2018, Du et al., 2001). Further, the ERC is the region of the brain where the early histopathological changes of AD occurs before migrating along the hippocampus (Braak & Braak, 1997). An early identification of ERC volume loss in the correct clinical setting may have the potential to be used as a proxy measure of CSF Amyloid$\beta_{1\text{-}42}$ along with the other biomarkers in the correct clinical settings.

People with cognitive impairment are usually assessed using cognitive tests (Folstein et al., 1975). Such assessments include the Montreal Cognitive Assessment (MoCA) (Nasreddine et al., 2005). Here, we found a consistent association between the volume of the hippocampal subfields and the MoCA score for the Alzheimer's disease participants (Fig 4.10 and Table 4.3). For all subfields there was a trend for the volume to increase with MoCA score, suggesting that reduced hippocampal subfield volumes are associated with cognitive impairment, but significance was only achieved in the tail with $R^2 > 0.709$ and $p = 0.014$. A similar relationship was also reported in a 3T study conducted by Ogawa (Ogawa et al., 2019). Previous studies have established the relationship between CA1 volume and cognitive task for individuals with memory problems (S. G. Mueller et al., 2011).

Here, susceptibility was referenced to the average over the whole brain to reduce variability, therefore areas of negative susceptibility will generally represent areas of higher myelination or reduced iron relative to the average over the brain, while areas of positive susceptibility will generally have more iron or reduced myelin (although the exact relationship is multifactorial and complex). Figure 4.6 shows that the susceptibility of the whole hippocampus was negative in agreement with the work of (Acosta-Cabronero et al., 2018) at 3T, and there was no significant change in susceptibility of the whole hippocampus between the AD patients and the healthy controls.

A review paper by (Ravanfar et al., 2021), reports that of six studies of susceptibility changes in the hippocampus in Alzheimer's disease, four show no significant changes in the susceptibility of the hippocampus in AD.

Figure 4.7 and Table 4.1 show that only the DG subfield showed a statistically significant difference in susceptibility between the AD and HC groups with a p-value of 0.045, this result became statistically insignificant when |Bonferroni correction was applied. The smaller regions (e.g. the tail) are unlikely to provide reliable measurements due to their sizes. Fig 4.7

does suggest that regions of positive susceptibility (ERC and SUB) become more positive for the AD patients possibly due to preferential iron deposition in these regions.

Fig. 4.10 shows the correlation between the susceptibility of each subfield and MoCA score for the AD patients. The relationship was negative (i.e. increasing susceptibility with declining MoCA score and cognitive ability) in ERC and SUB, where the net susceptibility of the region was positive, while it was positive in the DG, TAIL and CA where the net susceptibility is mostly negative. The correlation coefficient attained significance ($p \leq 0.05$) only for the DG and CA ($R^2 > 0.7$). Generally for the whole hippocampus the relationship between susceptibility and MoCA score also attained significance with $p = 0.006$ and $R^2 = 0.77$. The negative susceptibility observed for the whole hippocampus is largely due to the effects of the DG and CA, as they make up the largest part of the hippocampus.

In order to use the findings of our study for a clinical translation, a larger sample size should be tested. This study was not aimed to assess the causality of hippocampal subfield atrophy in the early stages of AD and further pathological studies could explore whether there is a direct relationship between the pathological state of CSF in AD and early hippocampal subfield atrophy. Although 7T MRI is less clinically available and more expensive than some other diagnostic modalities, the lack of radiation, non-invasiveness and enhanced sensitivity for direct measurement of early structural changes in the brain means that it has valuable potential for clinical use. If 7T MRI could be used as a proxy for Amyloid-positive AD during the early stages, this neuroimaging modality could provide structural and topographic information on the AD unlike other existing multi-modal MRI methods.

4.8 LIMITATIONS TO THE STUDY

One limitation of this study is the relatively small sample size, with only 11 AD patients and 11 healthy controls included. This limits the statistical power of the study and larger groups of participants would be beneficial to increase the precision of the findings.

Although efforts were made to recruit patients with early onset AD, the challenges associated with studying this population are acknowledged. Despite this, only three AD patients dropped out during the scanning sessions. However, motion artefacts proved to be a significant issue in this study, with data from two AD patients having to be excluded due to this. Further work is needed to reduce the effects of motion artefacts, such as using motion measurements made using a camera to correct data or employing behavioural methods to encourage participants to remain still during scanning.

Another potential limitation of the study is the use of susceptibility referenced to the whole brain, which may attenuate the detection of changes in the hippocampal subfields if there is a global change in susceptibility across the brain.

4.9 CONCLUSION

The results of this study suggest that high resolution MRI, particularly volumetry and susceptibility mapping, may serve as a potential biomarker for early detection of Alzheimer's disease. The association between the volume of the ERC and CSF Amyloidβ1-42 is a promising finding, and warrants further investigation in larger sample sizes.

Moreover, the relationship between the hippocampal subfields and abnormal proteins, such as CSF Amyloidβ1-42, and cognitive measures like MoCA scores, suggests that these measures may also have potential as biomarkers for early detection of AD. However, given the small sample size in this study, further research with larger sample sizes is necessary to fully explore the potential of these measures as biomarkers.

Overall, this study provides important insights into the use of high field, high resolution MRI in the detection and monitoring of Alzheimer's disease.

4.9 REFERENCES

Acosta-Cabronero, J., Milovic, C., Mattern, H., Tejos, C., Speck, O., & Callaghan, M. F. (2018). A robust multi-scale approach to quantitative susceptibility mapping. *NeuroImage*, *183*, 7–24. https://doi.org/10.1016/j.neuroimage.2018.07.065

Acosta-Cabronero, J., Williams, G. B., Cardenas-Blanco, A., Arnold, R. J., Lupson, V., & Nestor, P. J. (2013). In vivo quantitative susceptibility mapping (QSM) in Alzheimer's disease. *PLoS ONE*, *8*(11). https://doi.org/10.1371/journal.pone.0081093

Alves, L., Correia, A. S. A., Miguel, R., Alegria, P., & Bugalho, P. (2012). Alzheimer's disease: A clinical practice-oriented review. *Frontiers in Neurology*, *APR*(April), 1–20. https://doi.org/10.3389/fneur.2012.00063

Alzheimer's Association. (2023). *Alzheimer's Disease Facts and Figures*. https://www.alz.org/alzheimers-dementia/facts-figures

Alzheimer's Society. (2023). *How many people have dementia in the UK?* https://www.alzheimers.org.uk/blog/how-many-people-have-dementia-uk

Arvanitakis, Z., Shah, R. C., & Bennett, D. A. (2019). Diagnosis and Management of Dementia: Review. *JAMA - Journal of the American Medical Association*, *322*(16), 1589–1599. https://doi.org/10.1001/jama.2019.4782

Ates, S., Deistung, A., Schneider, R., Prehn, C., Lukas, C., Reichenbach, J. R., Schneider-Gold, C., & Bellenberg, B. (2019). Characterization of Iron Accumulation in Deep Gray Matter in Myotonic Dystrophy Type 1 and 2 Using Quantitative Susceptibility Mapping and R2* Relaxometry: A Magnetic Resonance Imaging Study at 3 Tesla. *Frontiers in Neurology*, *10*, 1320. https://doi.org/10.3389/fneur.2019.01320

Ayton, S., Faux, N. G., Bush, A. I., Weiner, M. W., Aisen, P., Petersen, R., Jack, C. R., Jagust, W., Trojanowki, J. Q., Toga, A. W., Beckett, L., Green, R. C., Saykin, A. J., Morris, J., Shaw, L. M., Khachaturian, Z., Sorensen, G., Kuller, L., Raichle, M., … Furst, A. J.

(2015). Ferritin levels in the cerebrospinal fluid predict Alzheimer's disease outcomes and are regulated by APOE. *Nature Communications*, *6*(May), 1–9. https://doi.org/10.1038/ncomms7760

Betts, M. J., Acosta-Cabronero, J., Cardenas-Blanco, A., Nestor, P. J., & Düzel, E. (2016). High-resolution characterisation of the aging brain using simultaneous quantitative susceptibility mapping (QSM) and R2* measurements at 7 T. *NeuroImage*, *138*, 43–63. https://doi.org/10.1016/j.neuroimage.2016.05.024

Braak, H., & Braak, E. (1997). Staging of Alzheimer-Related Cortical Destruction. *International Psychogeriatrics*, *9*(S1), 257–261. https://doi.org/10.1017/S1041610297004973

Brayne, C., Gill, C., Huppert, F. A., Barkley, C., Gehlhaar, E., Girling, D. M., O'Connor, D. W., & Paykel, E. S. (1995). Incidence of clinically diagnosed subtypes of dementia in an elderly population: Cambridge project for later life. *British Journal of Psychiatry*, *167*(AUG.), 255–262. https://doi.org/10.1192/bjp.167.2.255

Dening, T., & Sandilyan, M. B. (2015). Dementia: definitions and types. *Nursing Standard (Royal College of Nursing (Great Britain) : 1987)*, *29*(37), 37–42. https://doi.org/10.7748/ns.29.37.37.e9405

Du, A. T., Schuv, N., Amend, D., Laakso, M. P., Hsu, Y. Y., Jagust, W. J., Yave, K., Kramer, J. H., Reed, B., Norman, D., Chui, C., & Weiner, M. W. (2001). Magnetic resonance imaging of the entorhinal cortex and hippocampus in mild cognitive impairment and Alzheimer's disease. *J Neurol Neurosurg Psychiatry*, *71*, 441–447. https://doi.org/10.1136/jnnp.71.4.441

El-Hayek, Y. H., Wiley, R. E., Khoury, C. P., Daya, R. P., Ballard, C., Evans, A. R., Karran, M., Molinuevo, J. L., Norton, M., & Atri, A. (2019). Tip of the Iceberg: Assessing the Global Socioeconomic Costs of Alzheimer's Disease and Related Dementias and

Strategic Implications for Stakeholders. *Journal of Alzheimer's Disease*, *70*(2), 321–339. https://doi.org/10.3233/JAD-190426

Farfara, D., Lifshitz, V., & Frenkel, D. (2008). Neuroprotective and neurotoxic properties of glial cells in the pathogenesis of Alzheimer's disease: Alzheimer's Review Series. *Journal of Cellular and Molecular Medicine*, *12*(3), 762–780. https://doi.org/10.1111/j.1582-4934.2008.00314.x

Folstein, M. F., Folstein, S. E., & McHugh, P. R. (1975). "Mini-mental state". A practical method for grading the cognitive state of patients for the clinician. *Journal of Psychiatric Research*, *12*(3), 189–198. https://doi.org/10.1016/0022-3956(75)90026-6

Graham, M. S., Drobnjak, I., Jenkinson, M., & Zhang, H. (2017). Quantitative assessment of the susceptibility artefact and its interaction with motion in diffusion MRI. *PLoS ONE*, *12*(10), 1–25. https://doi.org/10.1371/journal.pone.0185647

Grøntvedt, G. R., Lauridsen, C., Berge, G., White, L. R., Salvesen, Ø., Bråthen, G., & Sando, S. B. (2020). The Amyloid, Tau, and Neurodegeneration (A/T/N) Classification Applied to a Clinical Research Cohort with Long-Term Follow-Up. *Journal of Alzheimer's Disease*, *74*(3), 829–837. https://doi.org/10.3233/JAD-191227

Gulisano, W., Maugeri, D., Baltrons, M. A., Fà, M., Amato, A., Palmeri, A., D'Adamio, L., Grassi, C., Devanand, D. P., Honig, L. S., Puzzo, D., & Arancio, O. (2018). Role of Amyloid-β and Tau Proteins in Alzheimer's Disease: Confuting the Amyloid Cascade. *Journal of Alzheimer's Disease*, *64*(s1), S611–S631. https://doi.org/10.3233/JAD-179935

Haapalinna, F., Paajanen, T., Penttinen, J., Kokki, H., Kokki, M., Koivisto, A. M., Hartikainen, P., Solje, E., Hänninen, T., Remes, A. M., & Herukka, S. K. (2016). Low Cerebrospinal Fluid Amyloid-Beta Concentration Is Associated with Poorer Delayed Memory Recall in Women. *Dementia and Geriatric Cognitive Disorders Extra*, *6*(2), 303–312. https://doi.org/10.1159/000446425

Haldenwanger, A., Eling, P., Kastrup, A., & Hildebrandt, H. (2010). Correlation between cognitive impairment and CSF biomarkers in amnesic MCI, non-amnesic MCI, and Alzheimer's disease. *Journal of Alzheimer's Disease*, *22*(3), 971–980. https://doi.org/10.3233/JAD-2010-101203

Hampel, H., & Blennow, K. (2004). CSF tau and β-amyloid as biomarkers for mild cognitive impairment. *Dialogues in Clinical Neuroscience*, *6*(4), 379–390. https://doi.org/10.31887/dcns.2004.6.4/hhampel

Hosseini, A. et al. (2022). Clinical Utility of Cerebrospinal Fluid Aβ42 and Tau Measures in Diagnosing Mild Cognitive Impairment in Early Onset Dementia. *Journal of Alzheimer's Disease*, *87*(2), 771–778.

Jack, C. R., Bennett, D. A., Blennow, K., Carrillo, M. C., Dunn, B., Haeberlein, S. B., Holtzman, D. M., Jagust, W., Jessen, F., Karlawish, J., Liu, E., Molinuevo, J. L., Montine, T., Phelps, C., Rankin, K. P., Rowe, C. C., Scheltens, P., Siemers, E., Snyder, H. M., … Silverberg, N. (2018). NIA-AA Research Framework: Toward a biological definition of Alzheimer's disease. *Alzheimer's and Dementia*, *14*(4), 535–562. https://doi.org/10.1016/j.jalz.2018.02.018

Jellinger A, K. (2018). Towards a Biological Definition of Alzheimer Disease. *International Journal of Neurology and Neurotherapy*, *7*(1), 535–562. https://doi.org/10.23937/2378-3001/1410095

Kuiper, M. ., Mulder, C., GJ, van K., P, S., & EC, W. (1994). Cerebrospinal fluid ferritin levels of patients with Parkinson's disease, Alzheimer's disease, and multiple system atrophy. *Journal of Neural Transmission - Parkinson's Disease and Dementia Section*, *2*, 109–114. https://doi.org/10.1007/BF02260965

Merriam, A. E., Aronson, M. K., Gaston, P., Wey, S. -L, & Katz, I. (1988). The Psychiatric Symptoms of Alzheimer's Disease. *Journal of the American Geriatrics Society*, *36*(1), 7–

22. https://doi.org/10.1111/j.1532-5415.1988.tb03427.x

Mueller, S. G., Chao, L. L., Berman, B., & Weiner, M. W. (2011). Evidence for functional specialization of hippocampal subfields detected by MR subfield volumetry on high resolution images at 4T. *NeuroImage*, *56*(3), 851–857. https://doi.org/10.1016/j.neuroimage.2011.03.028

Mueller, Susanne G., Schuff, N., Yaffe, K., Madison, C., Miller, B., & Weiner, M. W. (2010). Hippocampal atrophy patterns in mild cognitive impairment and alzheimer's disease. *Human Brain Mapping*, *31*(9), 1339–1347. https://doi.org/10.1002/hbm.20934

Nasreddine, Z. S., Phillips, N. A., Bédirian, V., Charbonneau, S., Whitehead, V., Collin, I., Cummings, J. L., & Chertkow, H. (2005). The Montreal Cognitive Assessment, MoCA: A brief screening tool for mild cognitive impairment. *Journal of the American Geriatrics Society*, *53*(4), 695–699. https://doi.org/10.1111/j.1532-5415.2005.53221.x

Ogawa, M., Sone, D., Beheshti, I., Maikusa, N., Okita, K., Takano, H., & Matsuda, H. (2019). Association between subfield volumes of the medial temporal lobe and cognitive assessments. *Heliyon*, *5*(6), e01828. https://doi.org/10.1016/j.heliyon.2019.e01828

Olsen, R. K., Carr, V. A., Daugherty, A. M., La Joie, R., Amaral, R. S. C., Amunts, K., Augustinack, J. C., Bakker, A., Bender, A. R., Berron, D., Boccardi, M., Bocchetta, M., Burggren, A. C., Chakravarty, M. M., Chételat, G., de Flores, R., DeKraker, J., Ding, S. L., Geerlings, M. I., … Wisse, L. E. M. (2019). Progress update from the hippocampal subfields group. *Alzheimer's and Dementia: Diagnosis, Assessment and Disease Monitoring*, *11*, 439–449. https://doi.org/10.1016/j.dadm.2019.04.001

Randall, C., Mosconi, L., Leon, M. De, & Glodzik, L. (2013). Cerebrospinal fluid biomarkers of alzheimer's disease in healthy elderly. *Frontiers in Bioscience*, *18*(3), 1150–1173. https://doi.org/10.2741/4170

Ravanfar, P., Loi, S. M., Syeda, W. T., Van Rheenen, T. E., Bush, A. I., Desmond, P., Cropley,

V. L., Lane, D. J. R., Opazo, C. M., Moffat, B. A., Velakoulis, D., & Pantelis, C. (2021). Systematic Review: Quantitative Susceptibility Mapping (QSM) of Brain Iron Profile in Neurodegenerative Diseases. *Frontiers in Neuroscience*, *15*(February). https://doi.org/10.3389/fnins.2021.618435

Schenck, J. F., Zimmerman, E. A., Li, Z., Adak, S., Saha, A., Tandon, R., Fish, K. M., Belden, C., Gillen, R. W., Barba, A., Henderson, D. L., Neil, W., & O'Keefe, T. (2006). High-field magnetic resonance imaging of brain iron in Alzheimer disease. *Topics in Magnetic Resonance Imaging*. https://doi.org/10.1097/01.rmr.0000245455.59912.40

Schuff, N., Woerner, N., Boreta, L., Kornfield, T., Shaw, L. M., Trojanowski, J. Q., Thompson, P. M., Jack, C. R., & Weiner, M. W. (2009). MRI of hippocampal volume loss in early Alzheimers disease in relation to ApoE genotype and biomarkers. *Brain*, *132*(4), 1067–1077. https://doi.org/10.1093/brain/awp007

Siderowf, A., Xie, S. X., Hurtig, H., Weintraub, D., Duda, J., Chen-Plotkin, A., Shaw, L. M., Van Deerlin, V., Trojanowski, J. Q., & Clark, C. (2010). CSF amyloid β 1-42 predicts cognitive decline in Parkinson disease. *Neurology*, *75*(12), 1055–1061. https://doi.org/10.1212/WNL.0b013e3181f39a78

Stricker, N. H., Dodge, H. H., Dowling, N. M., Han, S. D., Erosheva, E. A., & Jagust, W. J. (2012). CSF biomarker associations with change in hippocampal volume and precuneus thickness: Implications for the Alzheimer's pathological cascade. *Brain Imaging and Behavior*, *6*(4), 599–609. https://doi.org/10.1007/s11682-012-9171-6

Stuss, D. T., & Levine, B. (1996). The dementias: Nosological and clinical factors related to diagnosis. *Brain and Cognition*, *31*(2), 99–113. https://doi.org/10.1006/brcg.1996.0036

Taniguchi, A., Sasaki, D., Shiohara, A., Iwatsubo, T., Tomita, T., Sohma, Y., & Kanai, M. (2014). *Angewandte Alzheimer ' s Disease Hot Paper Attenuation of the Aggregation and Neurotoxicity of Amyloid- b Peptides by Catalytic Photooxygenation* **. 1382–1385.

https://doi.org/10.1002/anie.201308001

Tiwari, S., Venkata, A., Kaushik, A., Adriana, Y., & Nair, M. (2019). Alzheimer ' s Disease Diagnostics And Therapeutics Market. *Int J Nanomedicine ., Jul 2019*(14), 5541–5554.

Tsao, A., Sugar, J., Lu, L., Wang, C., Knierim, J. J., Moser, M. B., & Moser, E. I. (2018). Integrating time from experience in the lateral entorhinal cortex. *Nature*, *561*(7721), 57–62. https://doi.org/10.1038/s41586-018-0459-6

Vijayakumar, A., & Vijayakumar, A. (2013). Comparison of Hippocampal Volume in Dementia Subtypes. *ISRN Radiology*, *2013*, 1–5. https://doi.org/10.5402/2013/174524

Wharton, S., & Bowtell, R. (2010). Whole-brain susceptibility mapping at high field: A comparison of multiple- and single-orientation methods. *NeuroImage*, *53*(2), 515–525. https://doi.org/10.1016/j.neuroimage.2010.06.070

Wisse, L. E. M., Kuijf, H. J., Honingh, A. M., Wang, H., Pluta, J. B., Das, S. R., Wolk, D. A., Zwanenburg, J. J. M., Yushkevich, P. A., & Geerlings, M. I. (2016). Automated hippocampal subfield segmentation at 7T MRI. *American Journal of Neuroradiology*, *37*(6), 1050–1057. https://doi.org/10.3174/ajnr.A4659

Yushkevich, P. A., Pluta, J. B., Wang, H., Xie, L., Ding, S. L., Gertje, E. C., Mancuso, L., Kliot, D., Das, S. R., & Wolk, D. A. (2015). Automated volumetry and regional thickness analysis of hippocampal subfields and medial temporal cortical structures in mild cognitive impairment. *Human Brain Mapping*, *36*(1), 258–287. https://doi.org/10.1002/hbm.22627

Zeineh, M. M., Chen, Y., Kitzler, H. H., Hammond, R., Vogel, H., & Rutt, B. K. (2015). Activated iron-containing microglia in the human hippocampus identified by magnetic resonance imaging in Alzheimer disease. *Neurobiology of Aging*, *36*(9), 2483–2500. https://doi.org/10.1016/j.neurobiolaging.2015.05.022

CHAPTER FIVE

5.0 VASCULARIZATION OF THE HIPPOCAMPUS

5.1 OUTLINE

In this chapter, the focus is on exploring the vascularization of the hippocampus using a 7T MRI scanner, without the use of contrast agents. The arterial and venous supply of the hippocampus was investigated, as it is important for understanding possible changes in function and for successful surgery around the hippocampus. Additionally, understanding the venous supply is essential for interpreting fMRI studies of cognitive function in that area.

The study includes the identification and analysis of the major blood vessels supplying and draining the hippocampus. The in vivo angiograms of the arteries were compared to the results of previous in vivo and post-mortem studies (Wen et al., 1999). High resolution T_2* 3D GRE images were acquired from which SWI images were generated using the phase and magnitude data. The SWI images were used to investigate the venous drainage of the hippocampus.

The findings of this study provide valuable information on the vascularization of the hippocampus, which can aid in the study of neurodegenerative diseases and in surgical procedures around the hippocampus. Furthermore, the comparison of the results to previous studies enhances our understanding of the hippocampus' blood supply. The use of SWI images allows for the investigation of the venous drainage, which can improve the interpretation of fMRI studies of cognitive function in the hippocampus.

5.2 INTRODUCTION

The hippocampus is a highly complex and important brain structure that is involved in various cognitive functions, including memory consolidation, spatial navigation, and pattern separation

(Manjon et al., 2020). Its degeneration is a hallmark of Alzheimer's disease (AD) and is often used as a diagnostic criterion for this disease (H Braak & Braak, 1991). The measurement of hippocampal volume using magnetic resonance imaging (MRI) has become a valuable tool for the follow-up and treatment adjustment of AD patients (Jack et al., 2005). The hippocampus is divided into subfields, such as the dentate gyrus and Cornu Ammonis (CA) regions, which can be segmented and measured using automated segmentation techniques like Automatic Segmentation of Hippocampal Subfields (ASHS) (Yushkevich et al., 2015b), as discussed in detail in (chapters 3 and 4).

However, it is challenging to obtain in vivo studies of the vasculature of the hippocampus due to its location deep within the brain. Nonetheless, non-invasive in vivo studies are crucial for both healthy and diseased participants, providing valuable information for both neuroscience and neurology applications. Most investigations of the hippocampus are usually based on histology or post-mortem studies, which provide limited information about its dynamic function. Therefore, non-invasive in vivo studies are essential to better characterise the anatomy and ultimately to investigate the links between anatomy and function, particularly in understanding the mechanisms underlying neurodegenerative diseases like Alzheimer's.

The posterior cerebral artery (PCA) provides the primary supply to the anterior choroidal artery (AChA) (Spallazzi et al., 2019). These two arteries are the main vessels that supply blood to the hippocampus, individually or mixed. The hippocampal head is supplied by the anterior hippocampal artery (AH) and the uncus, while the hippocampal body and tail are supplied by the middle and posterior hippocampal arteries (MH and PH), respectively. The naming of the arteries is related to the part they supply (Marinković et al., 1992, Prades et al., 1993). However, considering the vasculature in more detail, a recent study by (Isolan et al., 2020) classified the hippocampal arterial vasculature of individuals into six groups, as shown in Figure 5.1:

• Group A: This group presents mixed irrigation, with the hippocampal arteries originating from the anterior choroidal, PCA, anterior infratemporal artery (AIA), and splenial artery (SA).

• Group B: The hippocampal arteries originate from the temporal branches, such as the main inferotemporal trunk, middle inferotemporal artery (MITA), posterior inferotemporal artery, or the main branch of PCA.

• Group B2: In this case, the inferior temporal arteries arise from a common trunk, with an arrowhead identifying a common inferior temporal artery.

• Group C: The anterior inferior temporal artery (AITI) is the main feeder of the hippocampus.

• Group D: The hippocampal arteries originate from the posterior cerebral artery's (PCA) main trunk, and they are the largest contributors to the hippocampus blood supply in this group.

• Group E: A single trunk of the posterior cerebral artery (named Ushimura's artery), with its origin at the main branch of PCA, irrigates practically the entire hippocampus.

• Group F: The hippocampal vessels arise exclusively from the parieto-occipital artery (POA), calcarine artery (CA), and the SA.

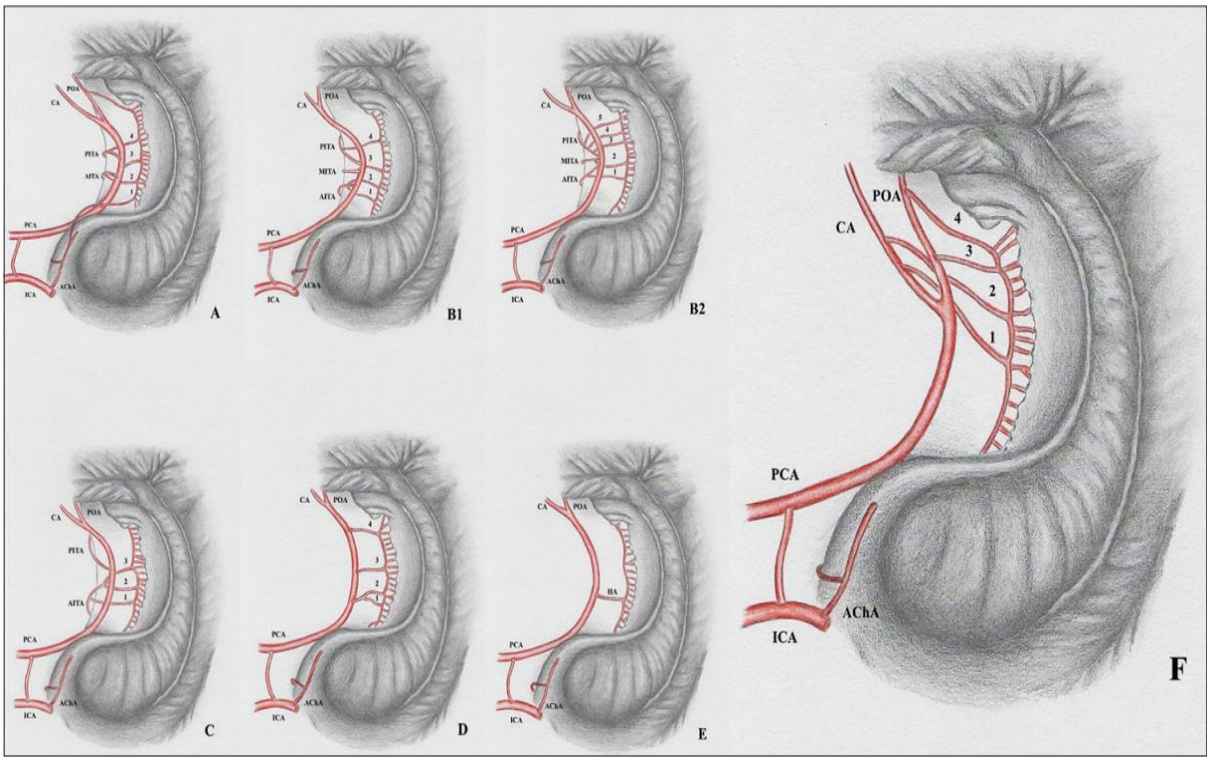


Figure 5.1: pictorial representation of different group categorizations of hippocampal arterial supply, showing the intra and extraventricular view of the hippocampus. See text for further explanation. CA: Calcarine artery; ICA: Internal carotid artery, PCA: Posterior cerebral artery, POA: Parieto-occipital artery, AITA: Anterior inferior temporal artery, MITA: Medial inferior temporal artery, PITA: Posterior inferior temporal artery, AChA: Anterior choroidal artery. 1, 2, 3, and 4: Hippocampal arteries'. (Isolan et al., 2020).

The hippocampus venous drainage has received less attention due to the technical challenges involved in studying it. However, the branches of the basal vein are known to be the main veins that drain blood from the hippocampus (Henri Duvernoy, Françoise Cattin, 2013). Within the hippocampus, two main veins can be distinguished: the sulcal intrahippocampus vein and the subependymal intrahippocampus veins (Henri Duvernoy, Françoise Cattin, 2013). The sulcal intrahippocampus vein is located between the Cornu Ammonis and the gyrus dentatus, while the subependymal intrahippocampus veins drain blood from the deep layers of the CA2, CA1 and subiculum. Knowledge of the hippocampal venous drainage is important for understanding the role of the hippocampus in cerebral blood flow regulation and in the pathophysiology of various diseases. For instance, venous congestion may lead to hypoxia and ischemia, which could damage the neurons in the hippocampus and cause cognitive impairment (Fulop et al.,

2019). Therefore, further studies are needed to better understand the venous drainage of the hippocampus and its clinical implications.

Studying the vasculature of the hippocampus in detail has been challenging in the past due to the small size of the arteries and veins, ranging between 0.2 and 1.0 mm in diameter. Most of the studies involving the vasculature of the hippocampus have been carried out using cadavers. However, with the advent of higher static field scanners (7T and above), we can use high-resolution angiography and venography to study the small vessels in vivo (Spallazzi et al., 2019).

Time-of-Flight (TOF) magnetic resonance angiography (MRA) is a non-invasive technique for imaging brain arteries and aneurysms (Akasaka et al., 2016, Sailer et al., 2014). It generates bright-blood contrast between inflowing and stationary spins, allowing visualization of the arteries in a certain region (Buck et al., 2022). The importance of TOF MRA has increased with the availability of higher field scanners, which offer increased sensitivity and longer T_1, resulting in a higher signal-to-noise ratio (SNR) and improved spatial resolution in a reasonable imaging time (Wrede et al., 2014). Therefore, TOF-MRA was used in this study at 7T to visualize small vessels such as the arteries that supply oxygenated blood to the hippocampus and other vital brain tissues (Spallazzi et al., 2019).

Despite its usefulness, TOF MRA has some pitfalls. For example, signal loss may occur due to slow flow or vessels in which flow is within (rather than across) the scan plane because of desaturation. Spin-dephasing may also occur due to flow at different speeds within the vessel, and signal dropout can be caused by veins close to the artery. Confounding signal from short T_1 materials, such as haemorrhage, and motion artefacts due to the long acquisition time may also affect the quality of the images obtained.

To study venous drainage of the hippocampus in vivo, many studies have utilized contrast agents such as ultra-small superparamagnetic iron oxides (USPIO) to increase susceptibility in the veins beyond the effect of deoxyhaemoglobin, thereby increasing T_2* contrast and reducing T_1 (Buch et al., 2020, Shen et al., 2020, Buch et al., 2022, Liu et al., 2018, Buch et al., 2021). Recently, in a study at 3T, Ferumoxytol was used as a contrast agent to increase susceptibility in the vein, improving the visualization of smaller structures such as small veins using T_2* dominated sequence or Susceptibility weighted image (SWI).

In this work, SWI was used, which exploits both the intrinsic phase and magnitude (T_2*) contrast from deoxyhaemoglobin, making it particularly sensitive to venous vasculature and iron storage. The fully flow-compensated, long echo GRE pulse sequence was used to acquire the image. It should be noted that despite the benefits of contrast agents in improving image quality, their use can also have drawbacks, including potential adverse reactions, increased cost, and longer imaging times. Therefore, careful consideration must be given to their use in research studies.

In this study, we utilized high-resolution TOF-MRA images to identify the arteries around the hippocampus, while a single-echo T_2*-weighted 3D GRE sequence was used to generate the susceptibility-weighted imaging (SWI) to identify the venous supply of the hippocampus. Both imaging techniques were optimized to obtain the best possible output for the veins and arteries around the hippocampus, enabling us to study the vasculature of this important brain structure in detail. By combining the strengths of these two imaging methods, we were able to gain a comprehensive understanding of the blood supply to the hippocampus and potentially shed light on the role of vasculature in hippocampal-related diseases.

5.3 METHODS

The study was conducted at the Sir Peter Mansfield Imaging Centre at the University of Nottingham in the UK. Image acquisition was carried out using a whole-body Philips ACHIEVA 7 T system, equipped with a Nova Medical (Wilmington MA, USA) single-channel transmit, and 32-channel receive (1Tx32Rx) head coil.

First, optimization scans were performed on a number of subjects to ensure the best output for the arteries and veins around the hippocampus. Subsequently, a systematic study of the arteries and veins was carried out in 8 healthy participants (4 females and 4 males, age 30 ± 8 years) who had no known neurological or psychiatric conditions.

All participants included in the study provided informed written consent, as approved by the protocol ethics.

5.3.1 OPTIMIZATION OF IMAGING SEQUENCES

5.3.1.1 OPTIMIZATION OF TIME OF FLIGHT ANGIOGRAPHY SEQUENCE

In TOF angiography a simple FFE scan is applied in which each RF pulse saturates the signal in the imaging slab but new spins flowing in remain unsuppressed and therefore give high signal. For a maximum flow signal completely new blood must enter the slice and fill all the vessels every TR period making angiography sensitive to the flow velocity (Figure 5.2). This means that the choice of TR and slab/slice thickness should be appropriate to the expected flow-velocity in the smallest vessels to be identified and so has to be optimised for each application. This can be particularly challenging if the flow is not largely axial (cranial -caudal) as is the case in the hippocampus where flow can be coming from any direction. If a particular field of view needs to be covered then it may be better to scan several thinner slabs to reduce the chances of the blood becoming saturated and hence to produce a stronger signal.

Furthermore, if the TR is changed to accommodate a different slab thickness or flow rater, then the flip angle required to suppress background signal needs to be changed and this will depend on the local tissue types and at 7T may require a practical consideration of RF inhomogeneity effects. A final issue that must be considered is that high flip angle pulses applied at short TR can lead to high SARs which may not be allowed within safety limits.

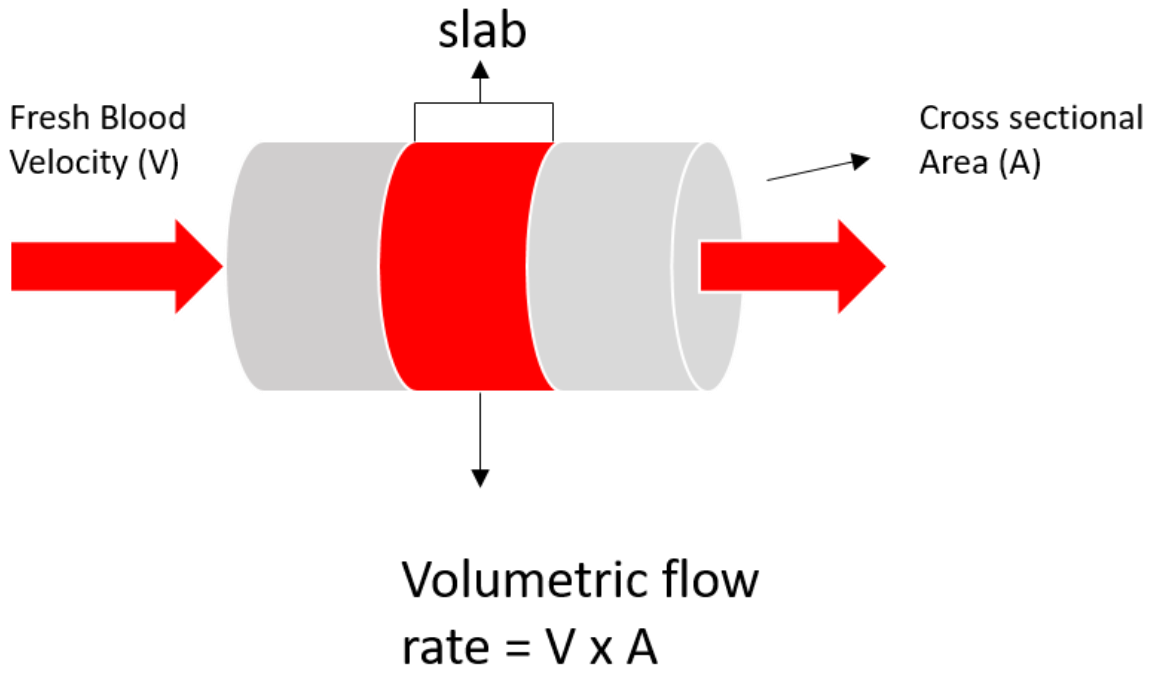


Figure 5.2: schematic showing the inflow effect in the TOF sequence for a 3D angiography. Ideally the velocity of flow must be sufficient so that the blood is replenished (refreshed) across the thickness of the whole slab in the repetition time (TR) of the FFE pulse sequence. The relationship between velocity and flow rate is also shown. In a real 3D slab it is likely that multiple small vessels will be emanating from a single point of entry at the distal end of the slab.

For optimization of angiography image imaging parameters must be chosen to enhance the visibility of blood vessels while minimizing interference from other tissues. Figure 5.3A presents the simulation of the expected relative signal from blood and tissue at various flip angles (FA) and repetition times (TR) for angiography image optimization, calculated using the equation for signal in the GRE sequence:

$$S_t = \frac{S_0 e^{-\frac{TE_t}{T^*_{2(t)}}} \times \sin\propto}{1-\cos\propto\times e^{-\frac{TR}{T_{1(t)}}}} \quad [5.1]$$

where S_b and S_t are the signal of blood and tissues, TE_b and TE_t are the echo time for blood and tissue, $T^*_{2(b)}$ and $T^*_{2(t)}$ are the T2* of blood and tissue respectively, $\propto$ is the flip angle, TR is the repetition time. For stationary tissue the signal peaks at the Ernst Angle for each TR. However, the signal from inflowing blood shows a standard saturation recovery curve.

$$S_b = S_0 e^{-\frac{TE_b}{T^*_{2(b)}}} \times \sin\propto \quad [5.2]$$

The simulation assumed full recovery of blood signal between RF pulses, T2* of blood of 80 ms, T1 of tissue of 1800 ms, T2* of tissue of 100 ms, and a minimum echo time (TE) of 4.45 ms, which is the shortest allowed. It also assumes that both blood and tissue share the same spin density. The stark difference between the curves for inflowing blood and stationary tissue demonstrates how a short TR GRE sequence can be used to highlight blood vessels in the image, provided the blood within them is moving fast enough to be refreshed within a TR. This difference in signal strength is a fundamental to angiography.

Figure 5.3B plots the difference between the blood and tissue signals to show the contrast achieved in angiography.

$$Contrast = S_b - S_t \quad [5.3]$$

This highlights that the best contrast is achieved at short TR.

However, at short TR and high flip angle specific absorption rate (SAR) increases. It is given by

$$SAR = \frac{\propto^2}{TR} \quad [5.4]$$

SAR is a critical safety consideration in MRI, as it reflects the amount of energy absorbed by the body and the scanner will limit the maximum flip angle available at short TR to limit SAR. Figure 5.3C maps the flip angle axis of Figure 5.3B onto SAR for each TR using equation 5.4.

It clear show that the optimum contrast for lowest SAR is achieved for longer TR. This situation will also provide best opportunity for complete replenishment of blood in the vessels. However longer TR also leads to longer scan time. Figure 5.3 summarizes the necessary tradeoffs when setting up an angiography sequence.

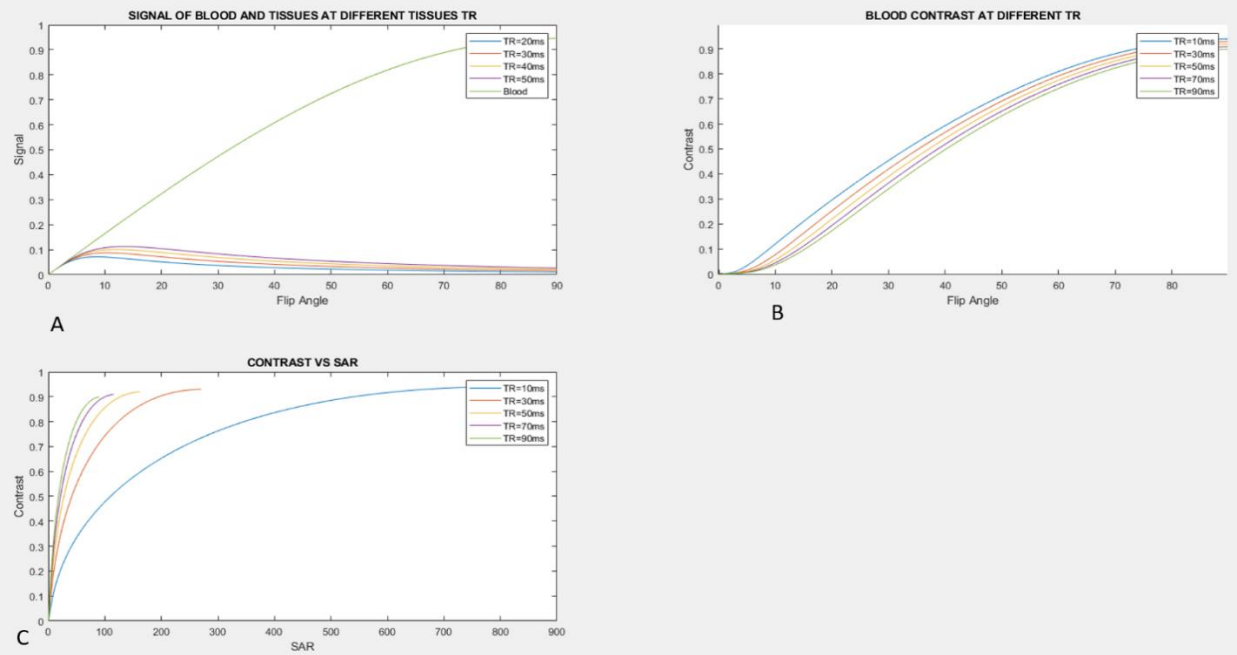


Figure 5.3: a plot of the A) signal of blood and tissue against the flip angle for different TR for the tissue B) the contrast of blood against flip angle for different TR and C) contrast against the specific absorption rate.

Informed by these simulations, three TOF sequences were investigated for visualization of the arteries as summarised in Table 5.1.

Sequence	Resolution (mm^3)	FOV (mm^3)	Coverage	Chunk	TR (ms)	TE (ms)	Fat water shift/band width (Hz/px)	FA (deg)	Time (min)
TOF1	0.2 x 0.2 x 0.8	200 x200 x8	4 stacks covering the hippocampi	0	20	3.5	8.8/115	30	4x03:03
TOF2	0.34 x 0.34 x 0.34	195 x179 x37	hippocampi	2 (thickness 18.36 mm)	10	4.4	3.65/276	20	07:23
TOF3	0.38 x 0.38 x 0.38	195 x178 x33	hippocampi	4 (thickness 8.36 mm)	14	4.5	3.65/275	22	06:07

Table 5. 1: the TOF sequences investigated, 3D FFE flow compensated sequence with the sense on

For the first sequence (TOF1 in Table 5.1), four TOF images with parameters shown were acquired with 10 slices each and then stacked together to cover the entire hippocampus as shown in Fig 5.4a. Each of the scans had an acquisition time of 03:03 min. The small slab thickness ensured the inflowing blood was unsaturated during the time of acquisition thereby generating a strong signal in the arteries, although splitting the phase encodings between different acquisitions reduces the signal to noise ratio. In this case four slabs were acquired separately to provide an opportunity for registration of data if required. However movement between acquisitions of the slabs led to loss of contrast in the overlapped region which prevented registration and the acquisition time for such a high resolution scan was too long.

To address these issues, a 3D TOF sequence (TOF2 in Table 5.1) was acquired in two chunks of thickness 18.36 mm. In this case the chunks use the Philips software for automatic alignment of the data which does not allow any motion correction between chunks but also allows faster scanning. The total acquisition time of 7:23min.

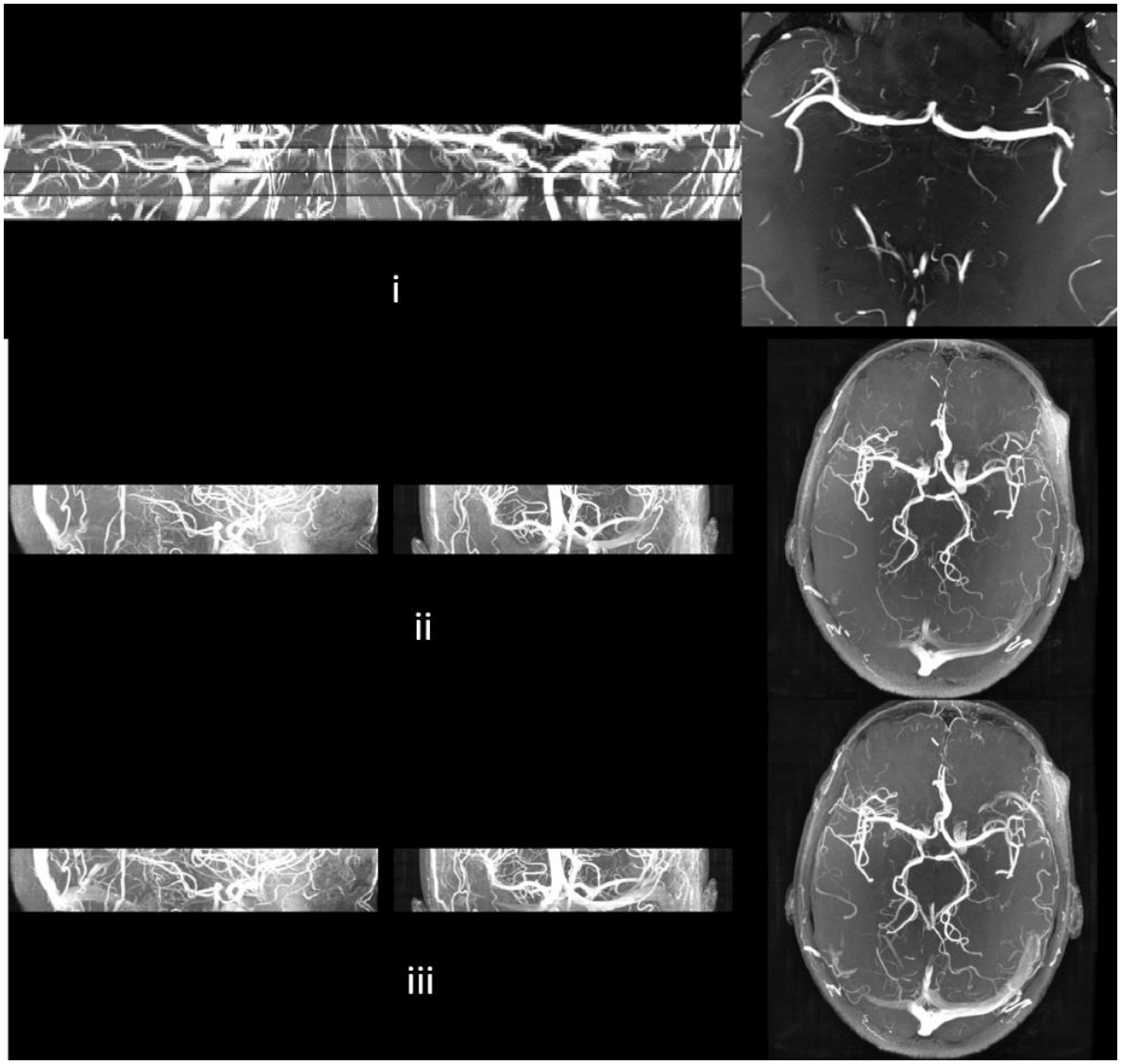


Figure 5.4a: showing the sagittal, coronal and axial of the three TOF MRA sequences investigated i) TOF1 4 stack scan ii) TOF2 with 0.34mm isotropic resolution and iii) TOF3 with 0.38mm isotropic resolution covering the entire hippocampus. This was use for the identification of the arteries around the hippocampus

Lastly, the TOF3 sequence (Table 5.1), explored the implications of reduced acquisition time, a crucial factor for motion limitation. This was achieved by augmenting the number of chunks to 4, with reduced thickness, and an increase in both TR and flip angle. As shown in Figure 5.4b, this optimization enhanced the visualization of small arteries around the hippocampal region of the brain, all within a more efficient acquisition timeframe.

This optimization not only provides a practical solution for minimizing motion artefacts, but it also show the potential to strike a balance between imaging quality and scan duration. In

clinical settings, where patient compliance and scan efficiency are paramount, this approach could prove instrumental in achieving diagnostic accuracy while ensuring patient comfort.

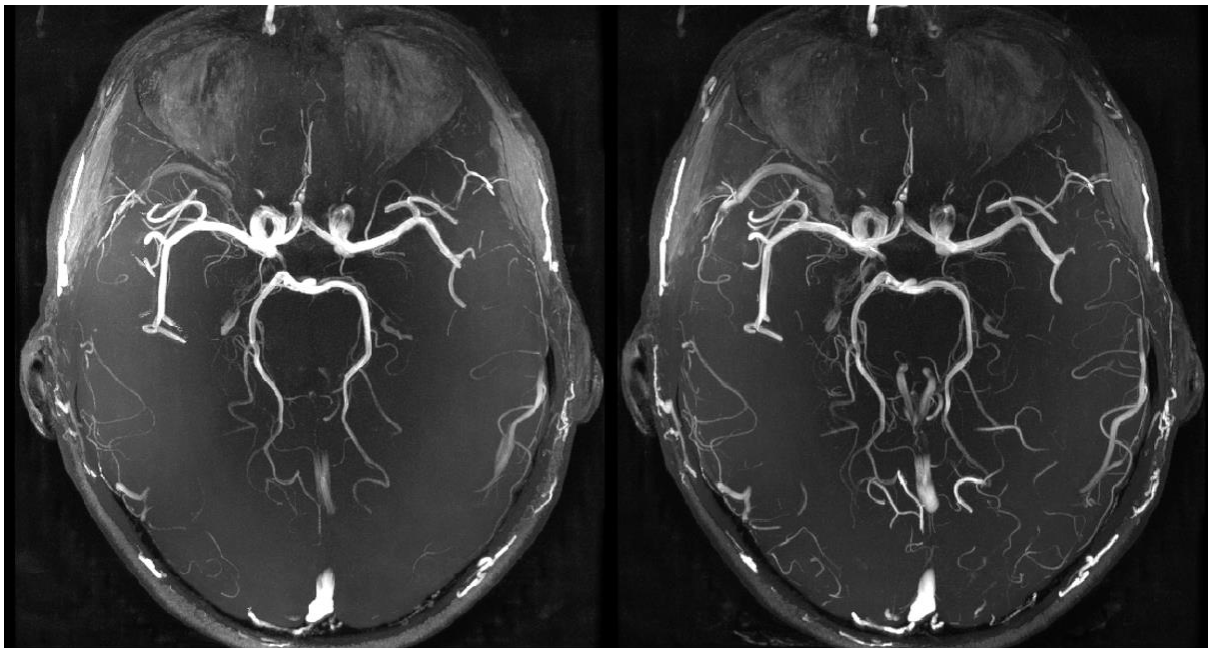


Figure 5.4b: Maximum Intensity Projection of the TOF-MRA sequences A) is the TOF2 with 0.34mm isotropic resolution and B) is the TOF3 with 0.38mm isotropic resolution). it shows clear that we can see more arteries in the TOF3 image

5.3.1.1 OPTIMIZATION OF T_2* IMAGE SEQUENCE

To understand the drainage system around the hippocampus especially the venous system in vivo, one needs to optimise T_2* images to improve the resolution of the scans to detect small veins.

The T_2* sequences investigated for the identification of the hippocampus veins are summarised in Table 5.2 below they are all flow compensated to reduce flow artefacts from vessels and CSF.

	Sequence	Resolution (mm^3)	FOV (mm^3)	Coverage	TR (ms)	TE (ms)	WSF/BW (HZ/px)	FA (deg)	Time (min)
GRE1	2D FLASH	0.3 x 0.30 x 1.20	180x 180x 54	Whole head	1000	25	28.9/35	70	04:35
GRE2	3D MULTI-ECHO GRE	0.38 x 0.37 x 0.74	224x 185x 50	hippocampi	24	8.2 and 18.4	5/202.5	8	06:38
GRE3	3D GRE	0.38 x 0.37 x 0.74	224x 185x 50	hippocampi	24	18	7/144	8	06:38

Table 5. 2: summary of the T_2 sequence investigated for better identification of the venous system of the hippocampus*

The first sequence (GRE1 Table 5.2) was a 2D Fast Low Angle Shot (FLASH) sequence with a long repetition time (TR =1000ms) to allow for more available signal per slice achieved due to recovery, which is an advantage as additional slices can be interleaved in the TR to reduce the overall scan time. However, this sequence was not sufficient for the identification of the hippocampal vein as the susceptibility of tissue close to the hippocampus (like the substantia nigra) generates very similar signals which made it difficult to identify and threshold the smaller region of hyperintensity coming from the veins. Another limitation of this sequence is that the 2D data had a large slice thickness of 1.2 mm which make it difficult to generate SWI (the process for generating the SWI will be explained in section 5.3.2.2) with reasonable resolution across all angles of the hippocampus

The second method (GRE2 Table 5.2) was a 3D multi-echo GRE image which aimed to generate a better SWI for identification of the hippocampal veins. This image was obtained with coverage perpendicular to the hippocampus axis. Reduction in the slice thickness to 0.74 mm helped improve visualisation of smaller veins and the 3D acquisition improved the SNR, though the acquisition time was increased due to the increase number of lines in the k-space despite the decrease in TR. In generating the SWI image using the multi-echo GRE we tried different combinations of the echoes of the phase and magnitude data, firstly we combined the first echo phase and magnitude together to produce the SWI, then we tried the second echo magnitude and phase and finally we tried inter-changing the echoes (i.e. combining the phase

data of echo-1 to the magnitude data of echo-2). The result of the SWI generated from the combination of the second echo phase and magnitude data produced the best SWI, as expected, because the phase data with the longest echo time most has accumulate relative phase shift complimenting for the loss of signal from the magnitude data.

The third scan, a 3D GRE single echo with same resolution as the multi-echo scan, was acquired with echo time similar to that of the longest echo time for the multi-echo, but with the advantage of being able to increase the water-fat-shift (7 pixels) and reduce the bandwidth (144 Hz) to improve the signal obtained for this image (a reduced bandwidth reduces the noise level in the pixels thereby increasing the signal-to-noise ratio of the image but at the cost of increased distortion). This also improved the quality of the SWI needed for the visualization of the veins.

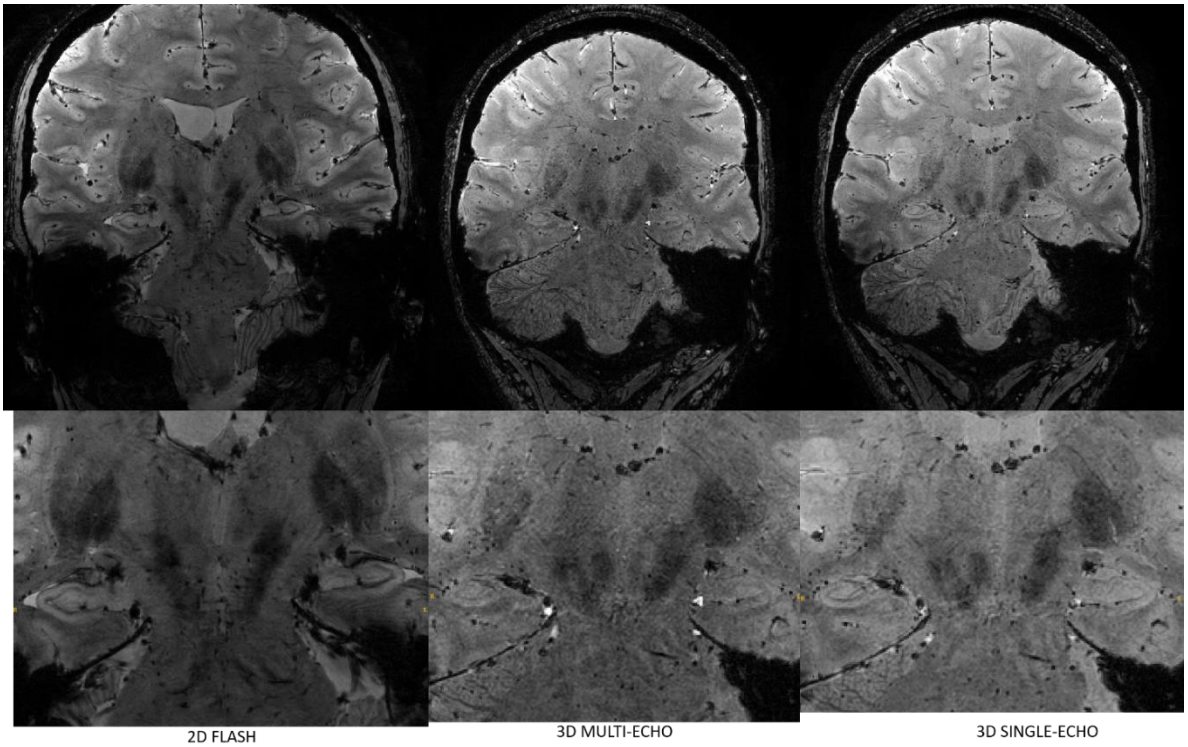


Figure 5.5: Showing the 3 sequences use for the generation of the SWI to identify the veins in this study as shown in Table 5.2.

5.3.2 METHODS AND IMAGING PROTOCOL

To locate the hippocampus for later scans and for hippocampal segmentation, a T_1-weighted PSIR image was acquired with the following parameters: 0.55 mm isotropic resolution, TR = 6.9 ms, TE = 5.1 ms, 348 number of slices and an acquisition time of 12:25 minutes.

To assist with segmenting the hippocampus a T_2-weighted FSE scan was also acquired with voxel size of $0.375 \times 0.375 \times 1.5\ mm$, TR = 5500ms, TE = 119 ms and an acquisition time of 04:24 minutes.

For the venography a T_2* single echo image was acquired perpendicularly to the long axis of the hippocampus to highlight the very tiny venous structure and was processed into a SWI. The scan had the following parameters; $0.38 \times 0.37 \times 0.74\ mm$ reconstructed at $0.35 \times 0.35 \times 0.37\ mm$ TR = 24 ms, TE = 18 ms, FA =8^0, Water-fat shift was set at 7 pixels and bandwidth at 144.6 Hz, and a practical optimization of the trade-off between SNR and distortion in the SWI; the acquisition time was 06:39 min.

The last set of images acquired was TOF angiography. We optimized this scan to maximise saturation of tissue and minimise saturation of inflow blood, in the shortest possible time, covering the entire hippocampus and at a resolution of 0.38 mm isotropic using 4 packages, TR = 14 ms, TE = 4.5, FA = 22^0 the TA was 06:07 min.

5.3.3 IMAGE PROCESSING AND ANALYSIS

5.3.3.1 HIPPOCAMPAL SEGMENTATION

The hippocampus segmentation was performed using Automatic Segmentation of Hippocampus Subfield (ASHS), a software developed by (Yushkevich et al., 2015b). This method utilizes both T_1-weighted and T_2-weighted images to generate a segmentation of the hippocampus, as explained in chapter 3. Fig 5.6 shows a 3D representation of the segmentation obtained from ASHS and the segmentation overlaid on a T_2-weighted image. To ensure the

accuracy of the segmentation, the segmented hippocampus mask was inspected using both FSLeyes and MeVisLab (MeVis, Bremen, Germany). MeVisLab is a powerful framework for image processing of 2D and 3D medical imaging data sets and offers rapid prototyping, a wide range of features, supported file formats, and extensibility options.

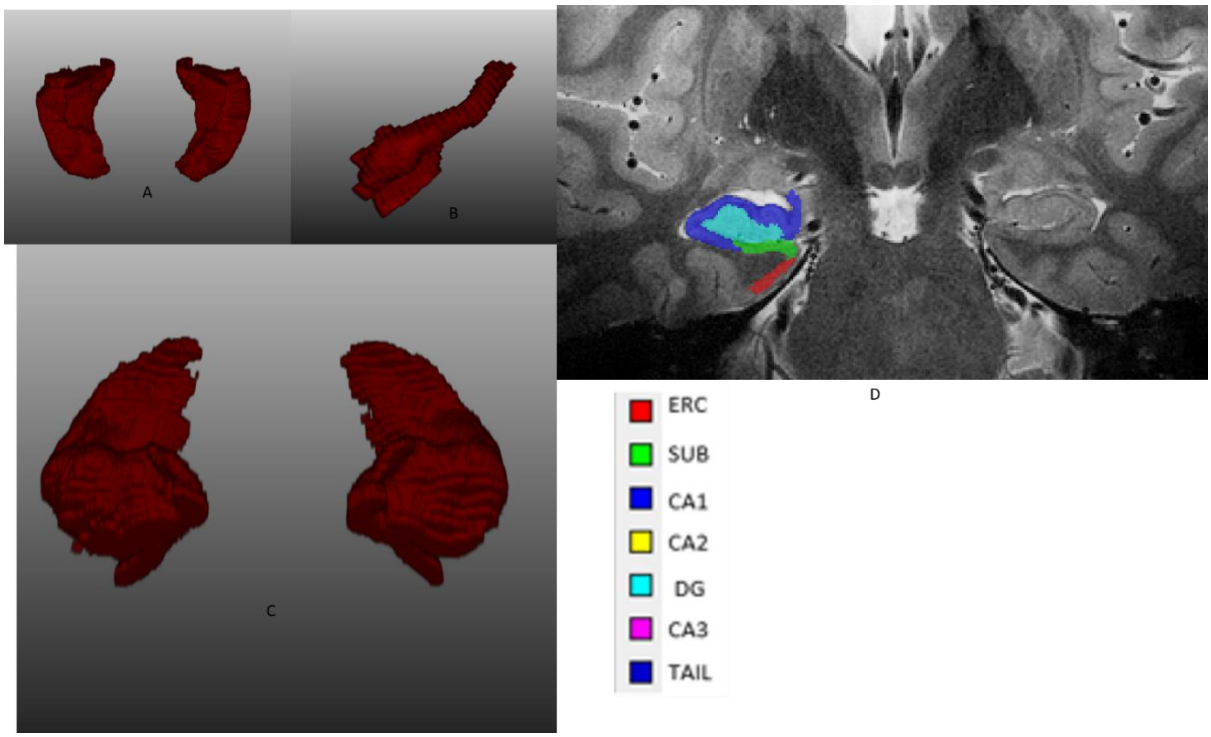


Figure 5.6: The Axial, sagittal and coronal view of the hippocampus segmentation and it overlaid on the T_2-weigthed

5.3.3.2 TOF ANGIOGRAPHY DATA

The TOF images shown in the figure below were obtained for each participant in this study and were used for identifying the arteries around the hippocampus.

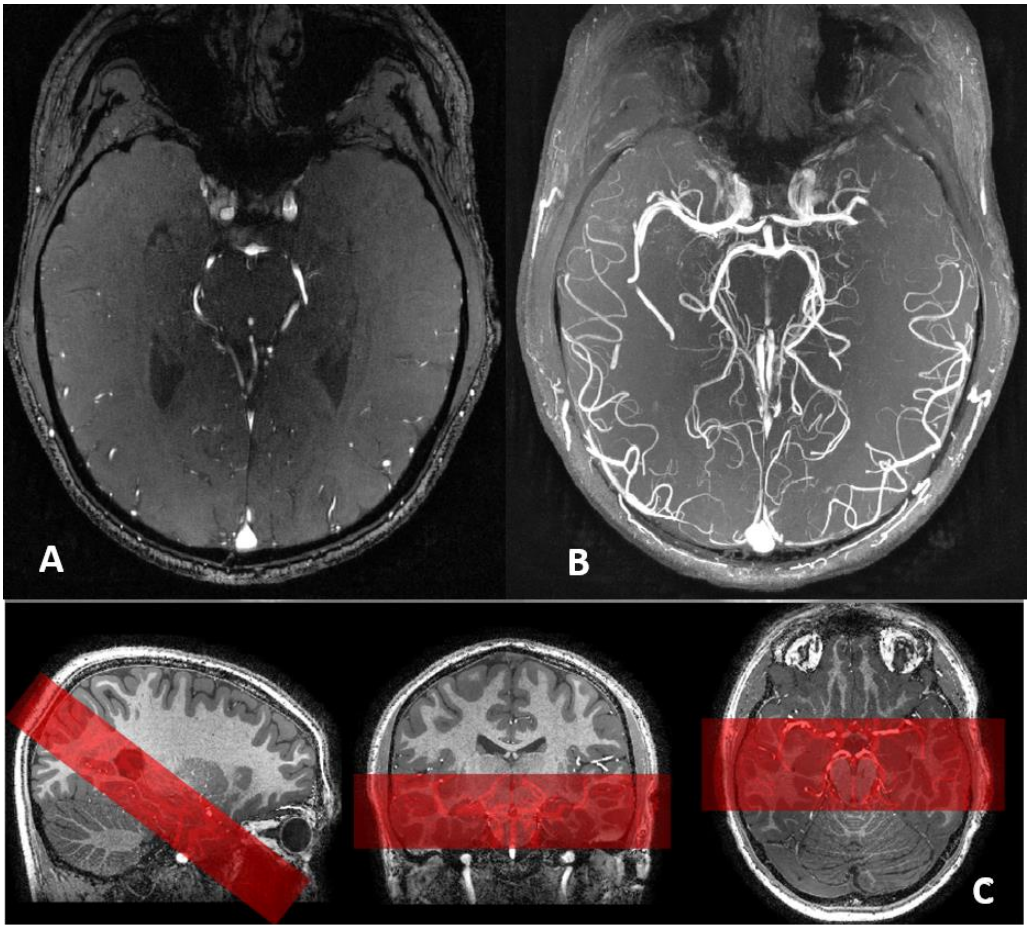


Figure 5. 7: A) The Time of Flight (TOF) B) the maximum intensity projection of the TOF for one of the participants in the study and C) the TOF (red) covering the entire hippocampus as acquired from the scanner.

To be able to visualise the tiny arteries around the hippocampus, TOF images were acquired covering the entire hippocampus as quickly as possible, to generate good contrast at a high resolution, as shown in Fig 5.7.

TOF-MRA were registered to the hippocampus mask, using FLIRT on FSL (Jenkinson et al., 2002), to avoid misidentification of the hippocampus artery (this helped eliminated arteries that were not connected to the hippocampus).

The TOF data was visualised using Maximum Intensity Projection software available in MeVisLab to identify the arteries, especially the posterior cerebral artery (PCA) and the anterior choroidal artery (AChA) as shown in Fig 5.9 to 5.17. The registered image was thresholded to extract just the signal from the arteries, with every pixel with signal below the threshold made zero. A single threshold for each data set was selected manually, depending

on the intensity of the image. The thresholding the TOF needed to be selected very carefully as it tended to lead to loss of smaller vessels.

5.3.3.3 SWI DATA

The SWI data were generated using the method described by (Haacke et al., 2004). Firstly, the phase image from the GRE data set is passed through a complex high pass filter to remove any artefacts and slowly varying phase shifts. The phase mask generated through this process is then multiplied by the magnitude image five times in MATLAB (R2020b, Mathworks, Inc., Natick, MA USA). This combination enhances the T_2* contrast with phase information and enables the identification of the venous supply of the hippocampus with high sensitivity. In the SWI images the paramagnetic deoxyhaemoglobin in the venous blood causes a signal dropout in the veins, making them appear dark in the SWI (compared to the original magnitude image as shown in Figure 5.8).

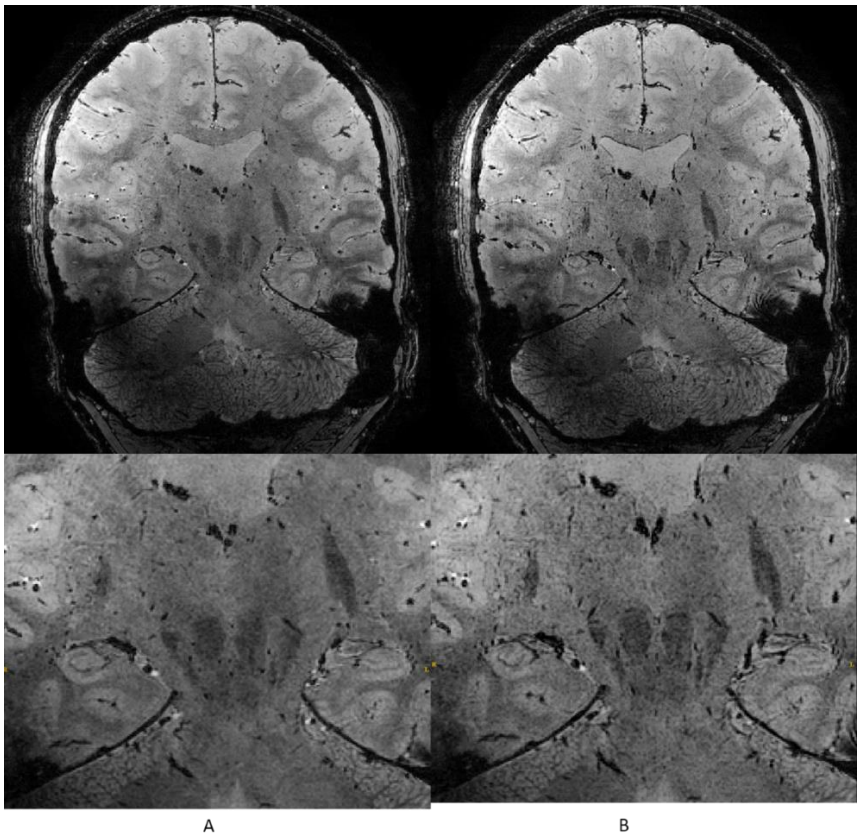


Figure 5.8: shows A) the magnitude image of the SE T_2 sequence and B) the magnitude image of the SWI obtained after processing A.*

After obtaining the SWI image, it was processed using MATLAB to segment the hippocampal veins. MeVisLab could not be simply used because of the reverse contrast of the SWI images. Firstly, the SWI was manually thresholded to identify the lowest signal potentially corresponding to the veins. This method has limitations as low signals from iron-rich tissues such as the Red Nucleus may lead to a loss of signal of smaller vessels, so a mask was used to remove such areas. Signals less than the threshold were set to zero, and signals greater than or equal to the threshold were set to one. The resulting vessel mask was then inverted, making the veins the brightest signals in the image, using 'imcomplement' function on MATLAB. The image was then denoised by removing voxels with less than 50 voxels connected to them, this was done by using the 'bwareaopen' function in MATLAB, which remove all connected component that contain fewer than 50 voxels in the T2* image, as those are considered to be noise. To identify the veins around the hippocampus, the denoised image was multiplied by a dilated mask of the hippocampus to avoid overlap from surrounding veins in the maximum intensity projections (MIPs). The resulting 3D image of the veins was finally visualized using MeVisLab software, as shown in Fig 5.9 to 5.17.

5.4 RESULTS

Here we present the results of the eight participants involved in this study. The subject demographics are given in Table 5.3. The groups to which the arteries were considered to fall are also given in Table 5.3.

	Age	Sex	Group
Subject 1	31	Female	Group A
Subject 2	23	Male	Group E
Subject 3	25	Male	Group C

Subject 4	28	Female	Group D
Subject 5	31	Male	Group F
Subject 6	59	Female	Group F
Subject 7	33	Female	Group F
Subject 8	20	Male	Group F

Table 5. 3: Subject demographics and assigned group for arteries

The results aim to provide a comprehensive 3D visualization of our dataset within the MevisLab environment. Figures 5.8 to 5.16 offer an insights into the veins responsible for draining the hippocampus, as well as the prominent arteries that supply blood to this region, across the eight participants within our study cohort. It's important to emphasize that these visualizations were attained without the application of any contrast agent.

A consistent pattern emerges from these visual representations, showing the consistent arrangement of veins and arteries around the hippocampal region. Nonetheless, individual anatomical distinctions contribute to some variations within this pattern. Also in the Fig 5.18-5.22, shows the specific vascularization pattern pertinent to each individual subject. A noteworthy comparison can be drawn between our findings and the schematic representation of vascularization patterns as categorized by (Isolan et al., 2020). Notably, Isolan et al.'s classification encompasses six distinct patterns, thereby offering an additional layer of insight into the hippocampal vasculature.

The findings revealed distinct vasculature patterns among the subjects. Subj01 exhibited a vasculature pattern aligned with group A from Isolan et al., featuring a combination of PCA, AchA, AIA, and SA as the sources of hippocampus arteries. Subj03 corresponded to group C, where the anterior inferior temporal artery (AITI) predominated as the primary hippocampus artery. Subj04 was categorized within group D, characterized by PCA as the predominant supplier to the hippocampus. Subj02 demonstrated characteristics of group E. Finally, subj05,

subj06, and subj08 showcased vasculature consistent with group F, the most common pattern within our cohort. In this configuration, hippocampal vessels emanated exclusively from the parieto-occipital artery (POA), calcarine artery (CA), and the SA. This diversity underscores the individual variability in hippocampal vasculature patterns within our study group.

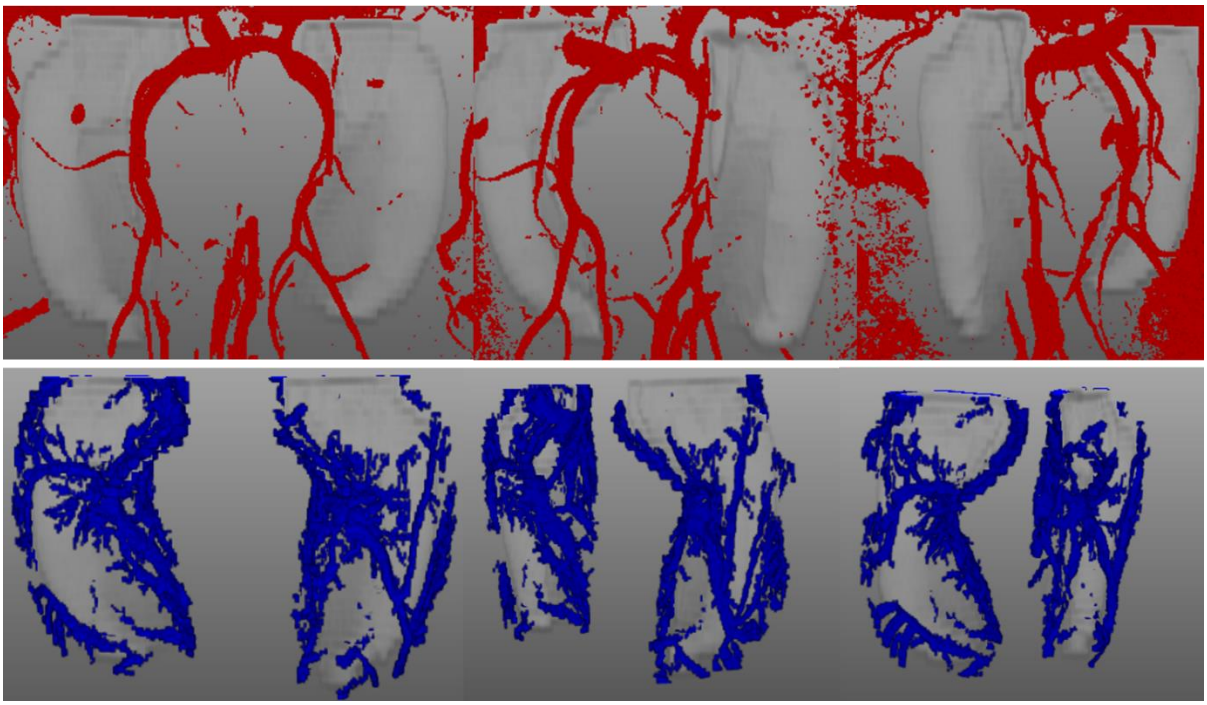


Figure 5.9: showing the arteries (red) and veins (blue) overlaid on the segmentation of the hippocampus for Subject 1. The images are taking from different orientations to show the vascularization clearly around the hippocampus. Subj01 exhibited a vasculature pattern aligned with group A from Isolan et al., featuring a combination of PCA, AchA, AIA, and SA as the sources of hippocampus arteries.

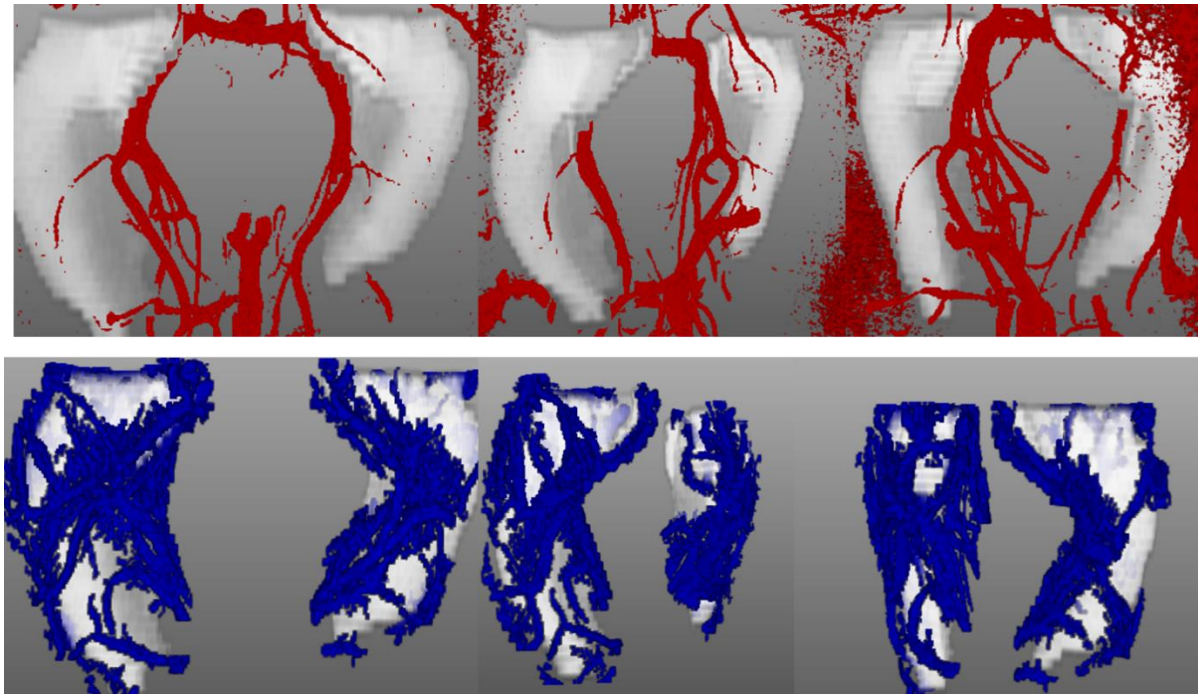


Figure 5.10: showing the arteries (red) and veins (blue) overlaid on the segmentation of the hippocampus for Subject 2. The images are taking from different orientations to show the vascularization clearly around the hippocampus. Subj02 exhibited a vasculature pattern aligned with group E from Isolan et al., featuring a combination of PCA, AchA, AIA, and SA as the sources of hippocampus arteries.

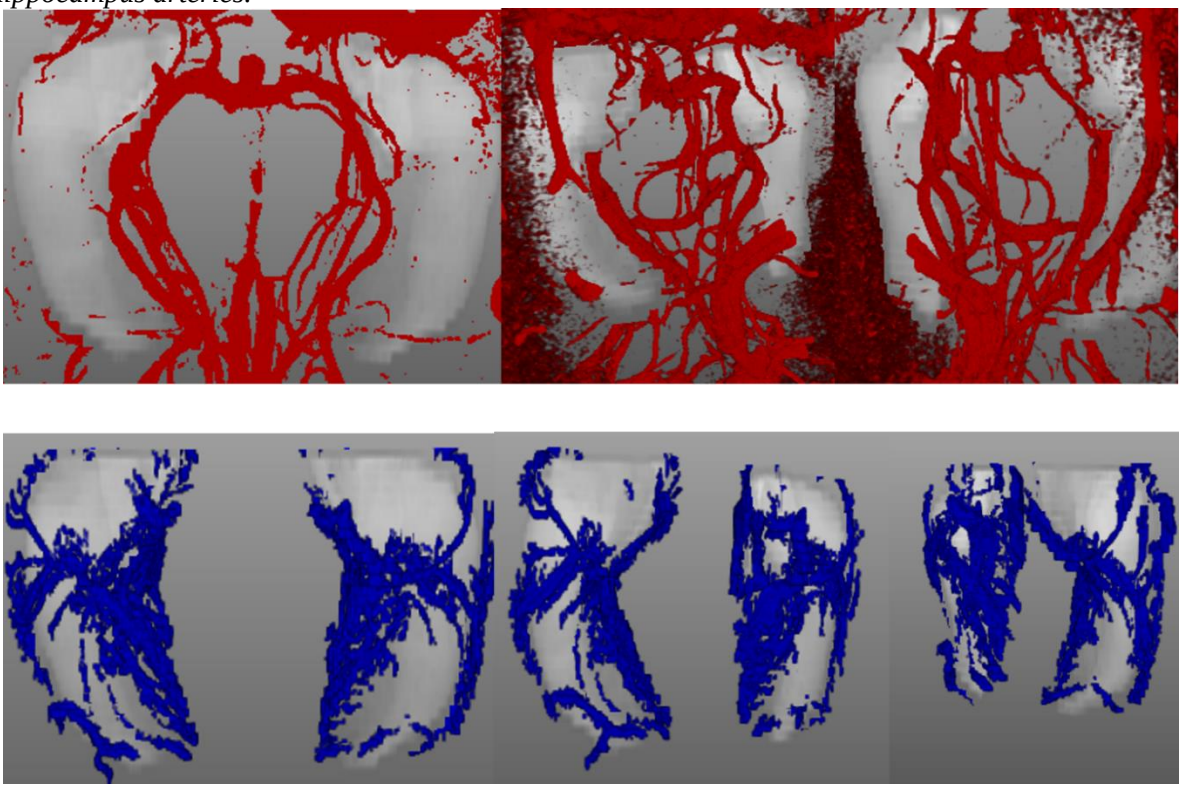


Figure 5.11: showing the arteries (red) and veins (blue) overlaid on the segmentation of the hippocampus for Subject 3. The images are taking from different orientations to show the vascularization clearly around the hippocampus. Subj03 exhibited a vasculature pattern aligned with group C from Isolan et al., featuring a combination of PCA, AchA, AIA, and SA as the sources of hippocampus arteries.

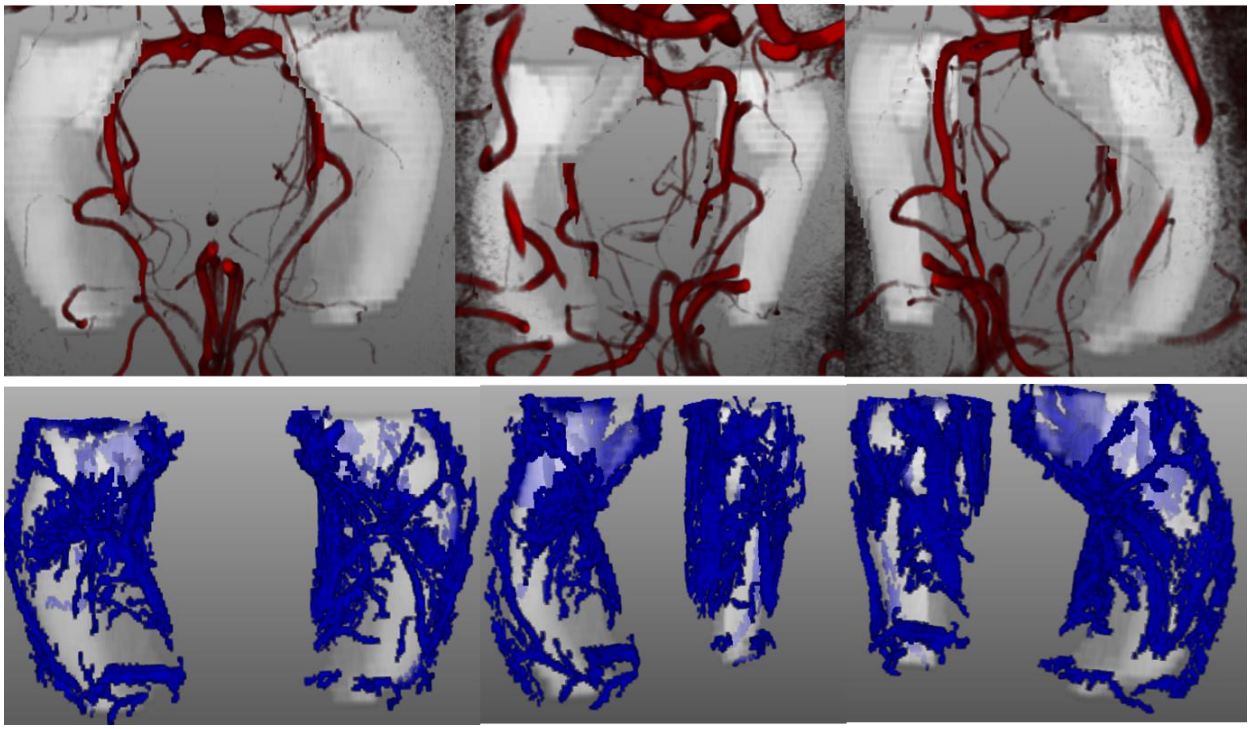


Figure 5. 12: showing the arteries (red) and veins (blue) overlaid on the segmentation of the hippocampus for Subject 4. The images are taking from different orientations to show the vascularization clearly around the hippocampus. Subj04 exhibited a vasculature pattern aligned with group D from Isolan et al., featuring a combination of PCA, AchA, AIA, and SA as the sources of hippocampus arteries.

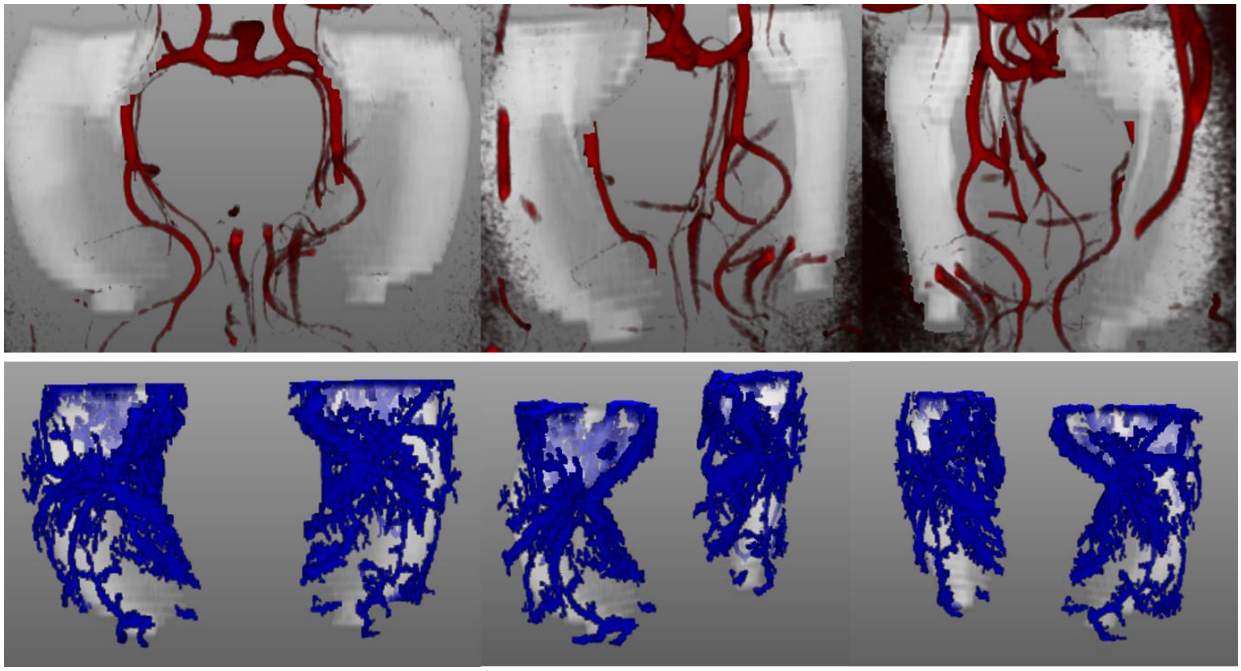


Figure 5. 13: showing the arteries (red) and veins (blue) overlaid on the segmentation of the hippocampus for Subject 5. The images are taking from different orientations to show the vascularization clearly around the hippocampus. This subject correspond to group F

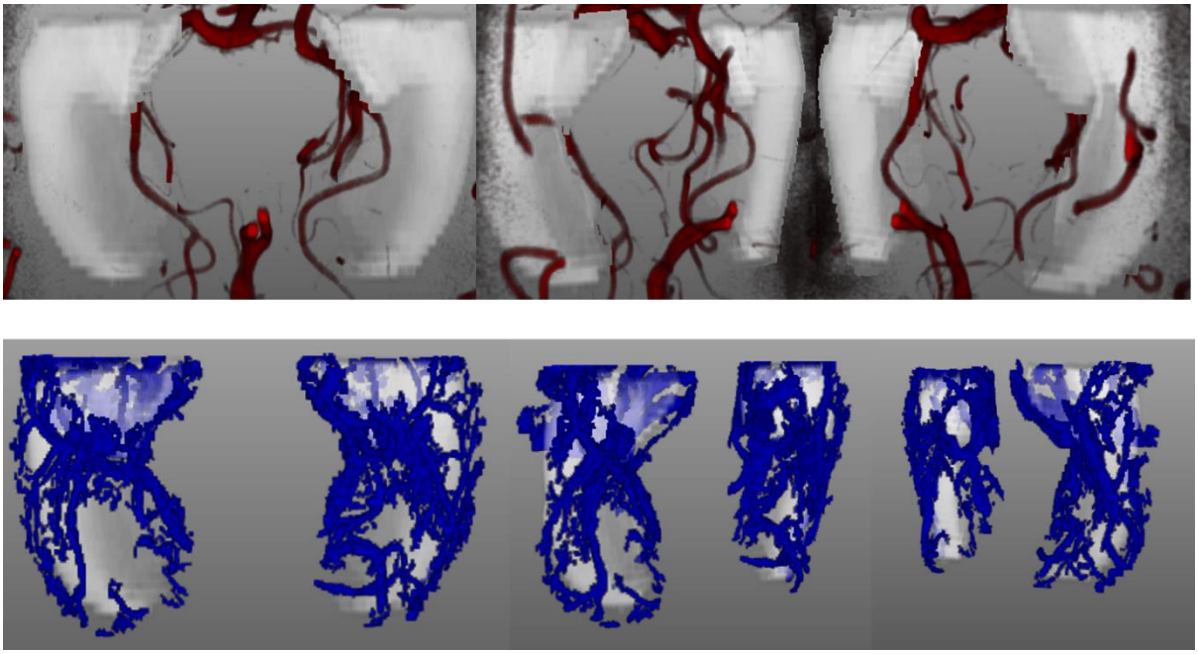


Figure 5. 14: showing the arteries (red) and veins (blue) overlaid on the segmentation of the hippocampus for Subject 6. The images are taking from different orientations to show the vascularization clearly around the hippocampus. Subject 6 also correspond to group F

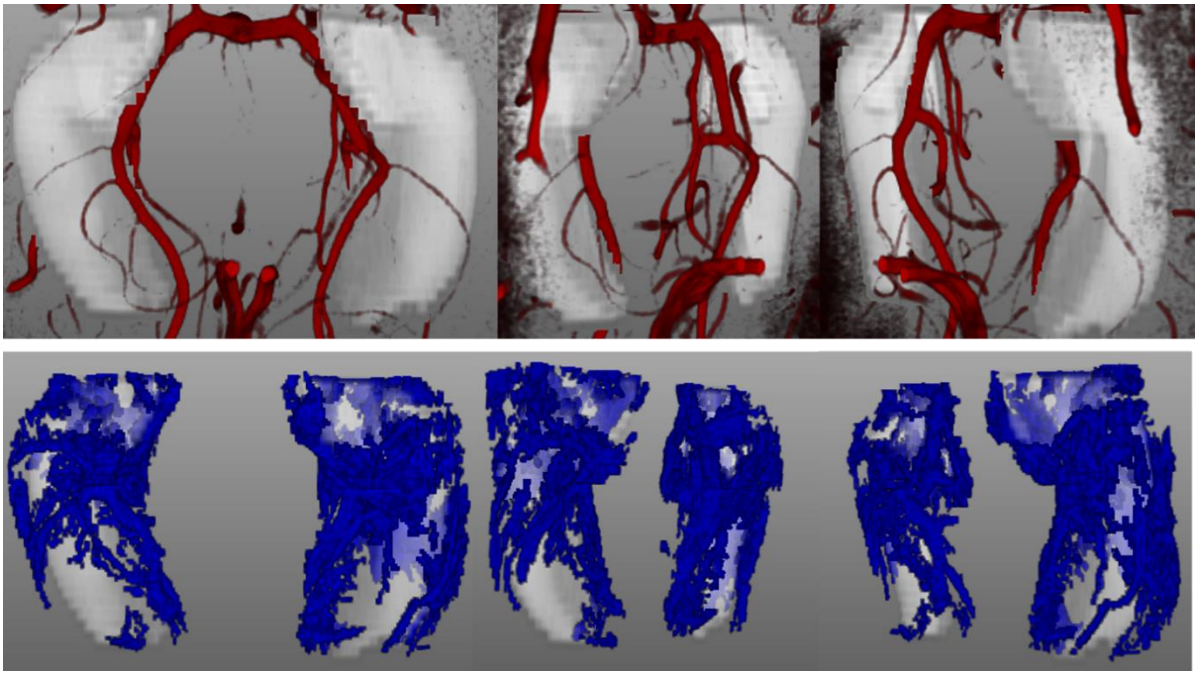


Figure 5. 15: showing the arteries (red) and veins (blue) overlaid on the segmentation of the hippocampus for Subject 7. The images are taking from different orientations to show the vascularization clearly around the hippocampus

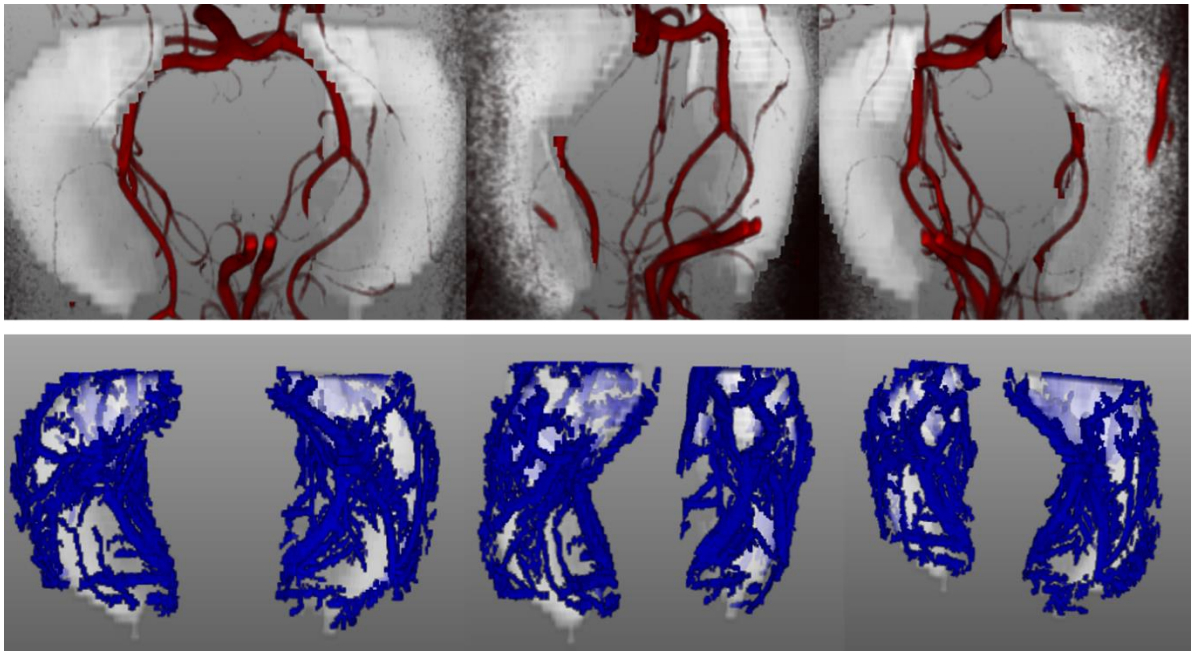


Figure 5. 16: showing the arteries (red) and veins (blue) overlaid on the segmentation of the hippocampus for Subject 8. The images are taking from different orientations to show the vascularization clearly around the hippocampus. Subject 8made the last groups that align with group F

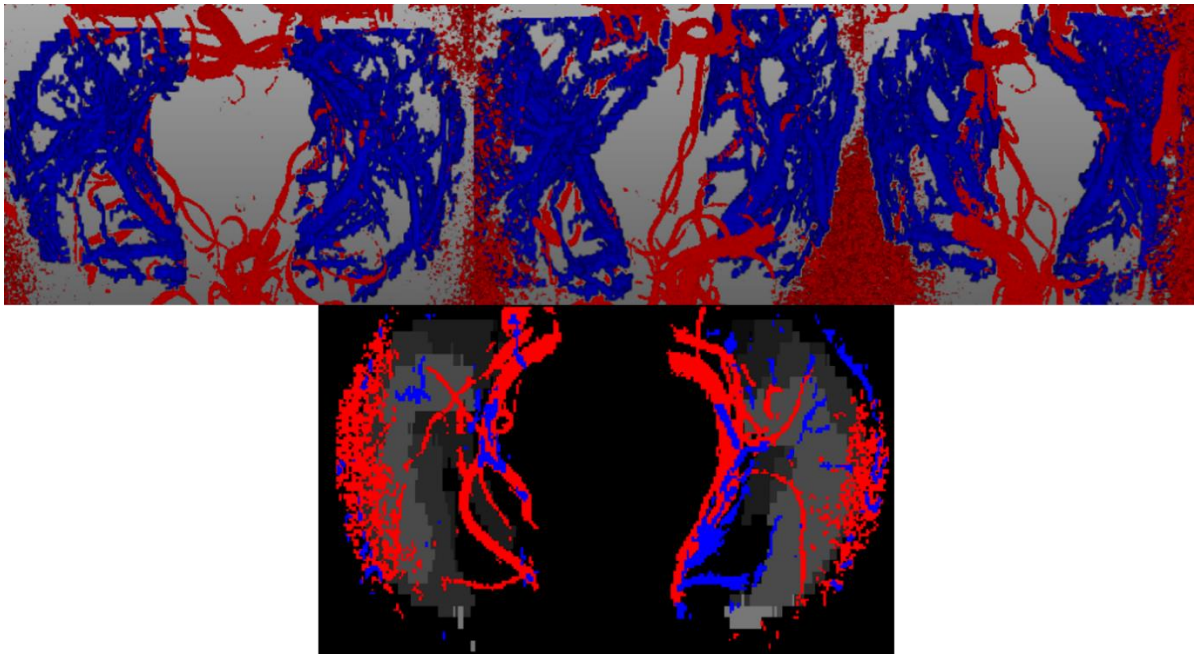


Figure 5. 17: show the complete vasculature of the hippocampus i.e a combination of both the artery (red) and veins (blue) and a 2D presentation overlaid on the segmentation of the hippocampus for subject 8.

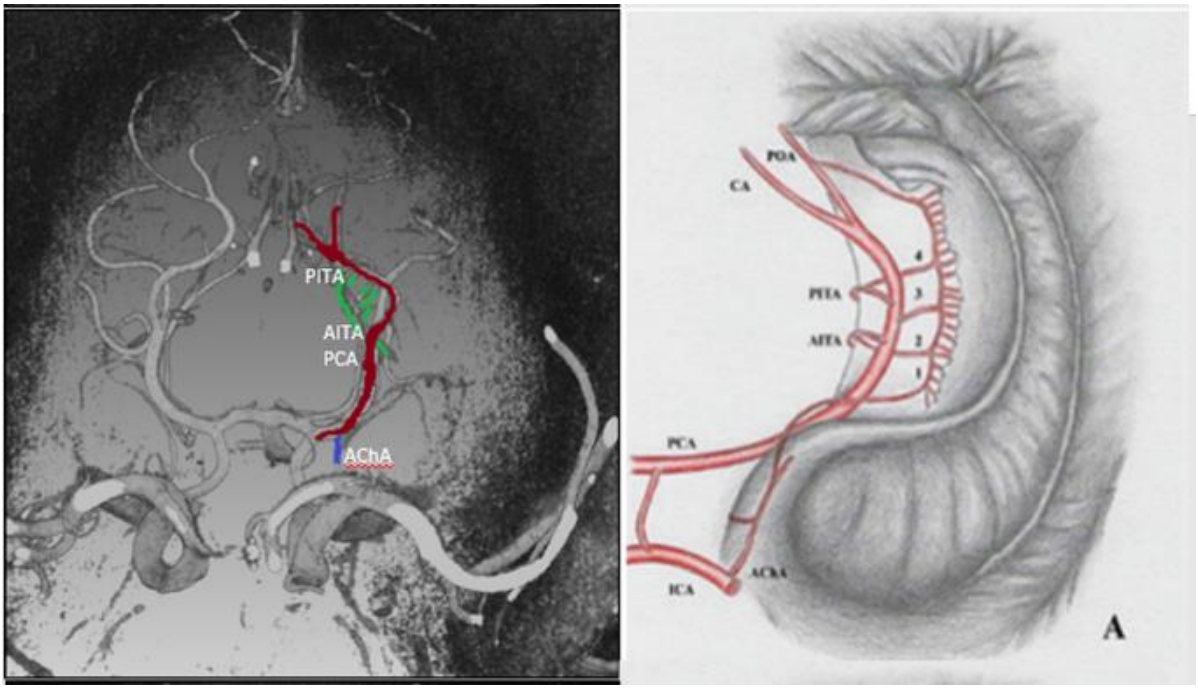


Figure 5.18: showing the hippocampus vascularisation pattern observed in subject 1; on the left is the TOF MRA image and on the left is the pattern from (Isolan et al., 2020) study. PCA: Posterior cerebral artery (red), AChA: Anterior choroidal artery (blue) and (PITA: Posterior inferior temporal artery/HA: Hippocampal arteries/AITA: Anterior inferior temporal artery) are in green

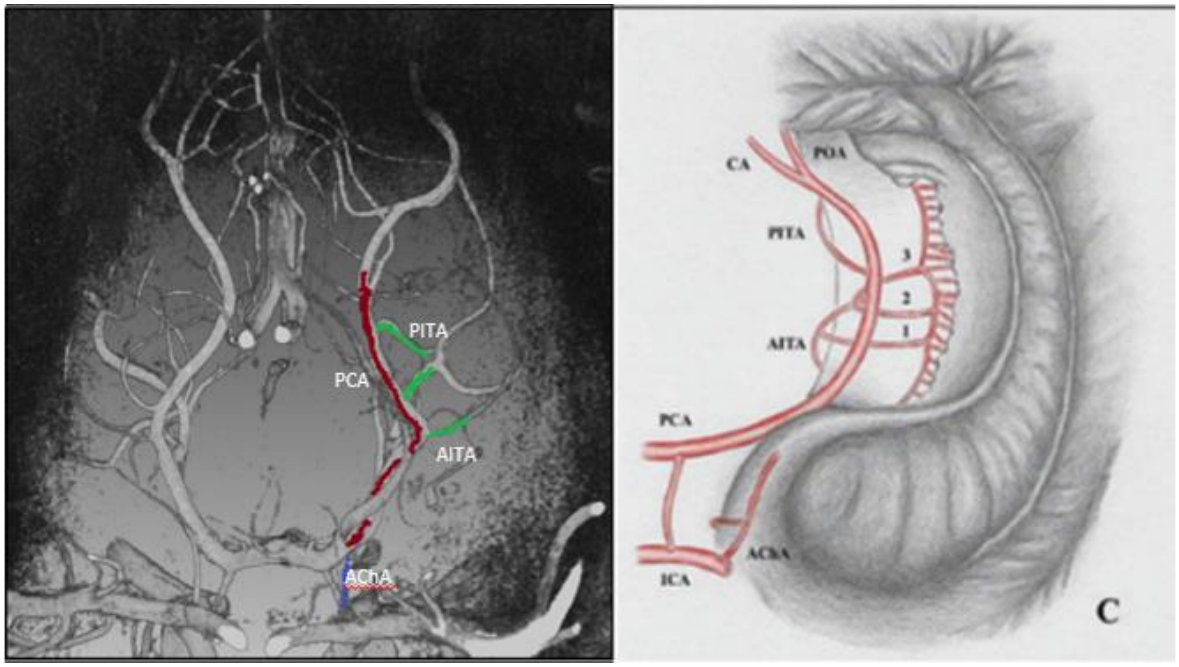


Figure 5.19: showing the hippocampus vascularisation pattern observed in subject 3; on the left is the TOF MRA image and on the left is the pattern from (Isolan et al., 2020) study. PCA: Posterior cerebral artery (red), AChA: Anterior choroidal artery (blue) and (PITA: Posterior inferior temporal artery/HA: Hippocampal arteries/AITA: Anterior inferior temporal artery) are in green

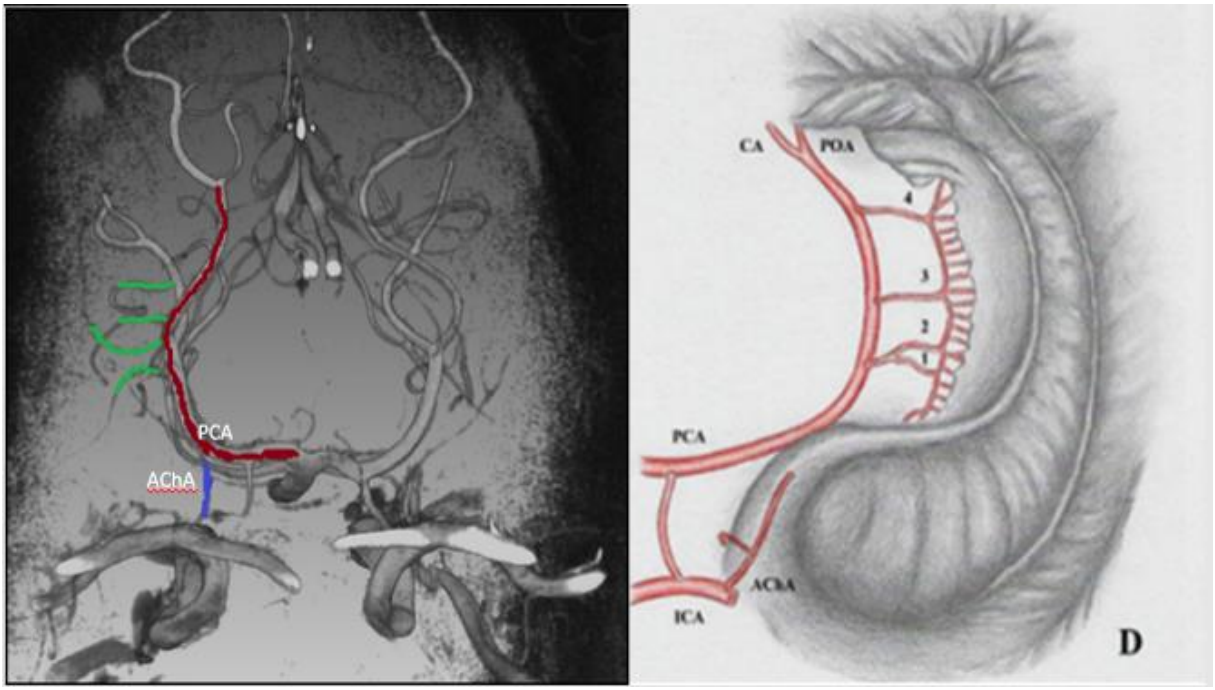


Figure 5.20: showing the hippocampus vascularisation pattern observed in subject 4; on the left is the TOF MRA image and on the left is the pattern from (Isolan et al., 2020) study. PCA: Posterior cerebral artery (red), AChA: Anterior choroidal artery (blue) and (PITA: Posterior inferior temporal artery/HA: Hippocampal arteries/AITA: Anterior inferior temporal artery) are in green

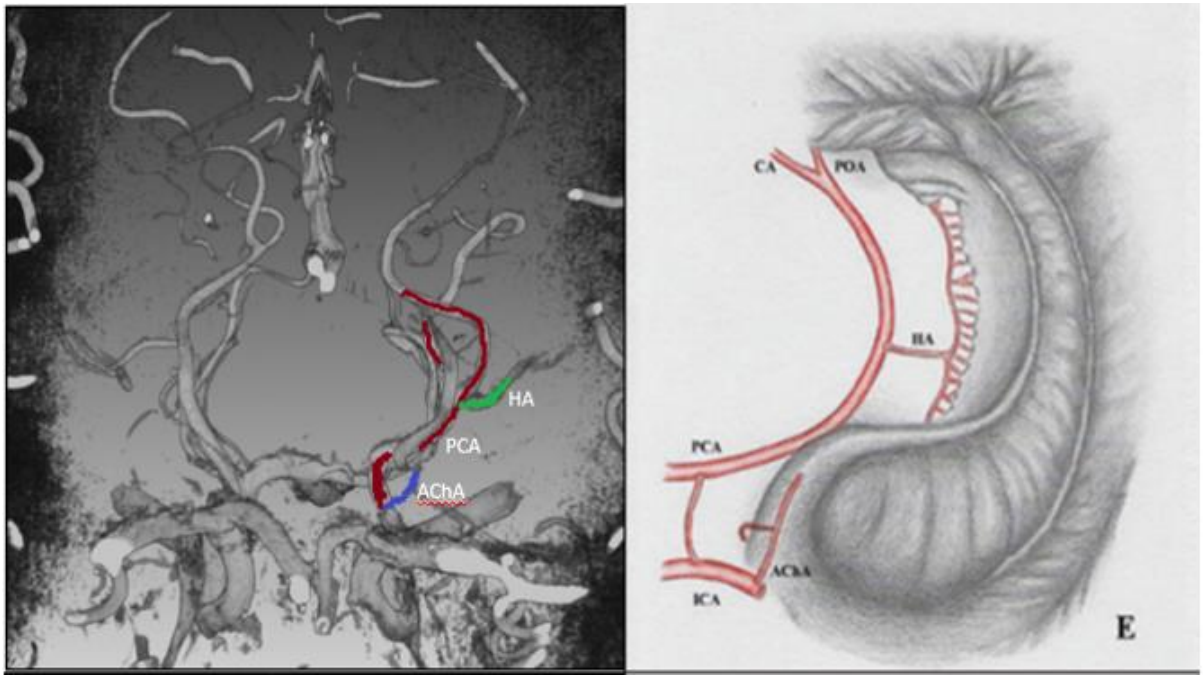


Figure 5.21: showing the hippocampus vascularisation pattern observed in subject 2; on the left is the TOF MRA image and on the left is the pattern from (Isolan et al., 2020) study. PCA: Posterior cerebral artery (red), AChA: Anterior choroidal artery (blue) and (PITA: Posterior inferior temporal artery/HA: Hippocampal arteries/AITA: Anterior inferior temporal artery) are in green.

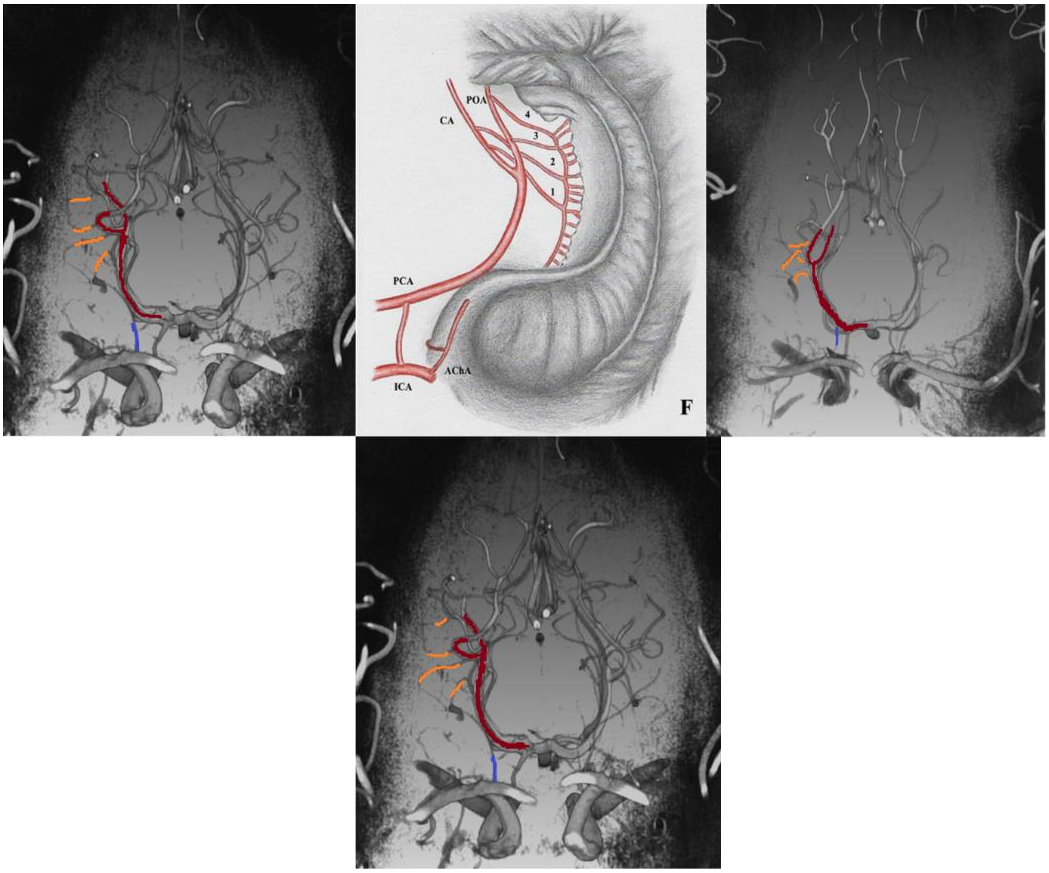


Figure 5.22: showing the pattern of hippocampal vascularisation observed in subject 5 (left), subject 6 (right) and subject 8 (bottom); the central image is the pattern from (Isolan et al., 2020) study. PCA: Posterior cerebral artery (red), AChA: Anterior choroidal artery (blue).

Figure 5.23 provides a comparative analysis between our findings and those presented in a cadaver study by (Wen et al., 1999). Through this comparison, we match certain arteries and veins obtained from subj07 with the corresponding anatomical structures depicted in the inked cadaver image. This parallel assessment show the alignment of our in vivo imaging outcomes with the anatomical information derived from a cadaveric context.

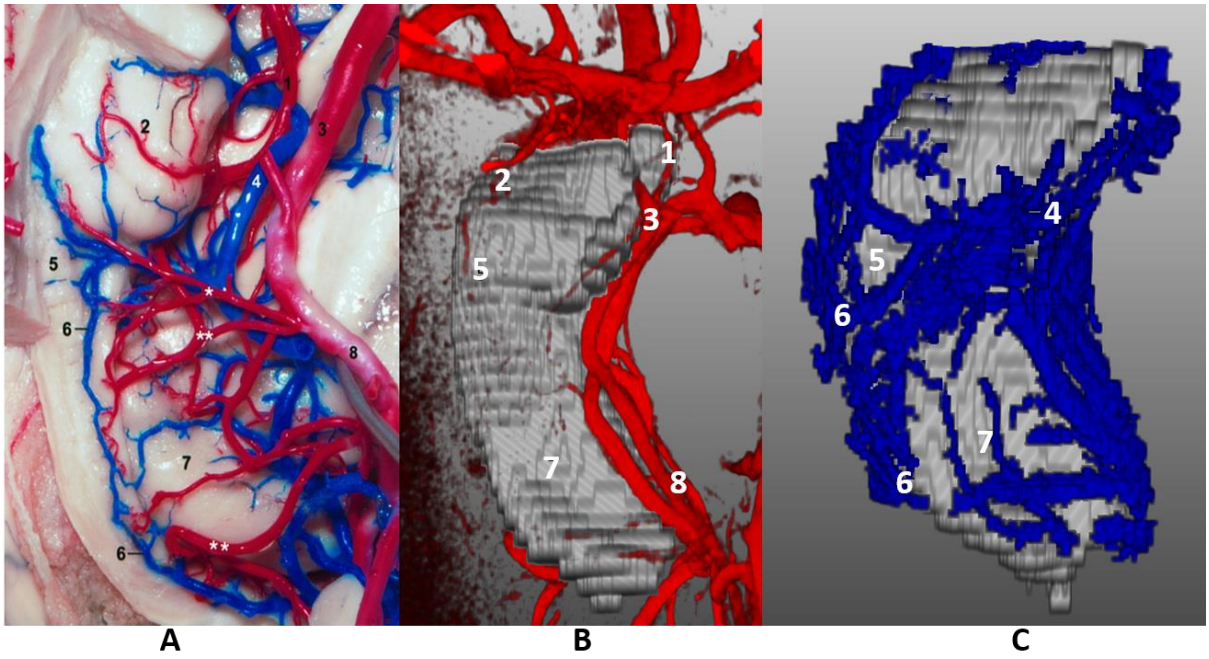


Figure 5.23: comparing A) the Cadaver image of the hippocampus (Wen et al., 1999) with B) our image of the arteries overlaid on the hippocampus and C) veins overlaid on the hippocampus. 1*, anterior choroidal artery;* 2*, inferior surface of the posterior segment of the uncus;* 3*, P2A segment of the posterior cerebral artery;* 4*, basal vein;* 5*, dentate gyrus and fimbria;* 6*, anterior and posterior longitudinal hippocampal veins;* 7*, pulvinar of the thalamus;* 8*, P2P segment of the posterior cerebral artery; *, hippocampal arteries; **, lateral posterior choroidal artery.*.

5.5 DISCUSSION

In this preliminary investigation, we have explored the potential of non-contrast imaging methods to map out the intricate vasculature of the hippocampus in vivo. By doing so, we identified the major arteries and veins responsible for supplying and draining blood from the hippocampus in individual subjects. This preliminary insight holds promise for further investigations into the relationship between hippocampal vasculature and degenerative pathology. In a study of an AD model in mice, a reduction in diameter of the artery that supply blood to the hippocampus (Dentate Gyrus) was observed together with a change in the vasculature pattern (Zhang et al., 2019).

To delineate the arterial network, we used the time-of-flight (TOF) imaging. Leveraging the contrast between fresh spins of blood and surrounding tissues, we employed high-resolution TOF with isotropic resolution of 0.38 mm to produce vivid images of arteries, as demonstrated

in Figures 5.9 to 5.17. This approach enabled us to identify arteries such as the posterior cerebral artery (PCA) with diameters between 2-3 mm, anterior choroidal artery (AChA), diameter 0.7-2mm, and various branches of the PCA, diameter 1mm (Spallazzi et al., 2019), with notable limitations in detecting smaller arteries below 0.5 mm due to the resolution constraints.

Post-mortem studies by Erdem (Erdem et al., 1993) and further classifications by (Isolan et al., 2020), our investigation classified hippocampal arterial vasculature according to distinct groups. Our analysis, uses a single hemisphere in each of the 8 participants, unveiled patterns of arterial supply aligned with five out of the six groups delineated by Isolan et al. (2020), as evident in Figures 5.18 to 5.22. The PCA emerged as the primary source of hippocampal supply, often accompanied by contributions from AChA. Three out of our 8 participants were classified as group F which is the most common group found in this study.

Moreover, the importance of Susceptibility-Weighted Imaging (SWI) for visualizing the small veins encircling the hippocampus, a goal that has previously usually required the use contrast agents (Buch et al., 2020, Shen et al., 2020, Buch et al., 2022, Liu et al., 2018, Buch et al., 2021) or only been possible in cadaver studies (Wen et al., 1999). Figures 5.9 to 5.17 show the utility of 7T 3D GRE with a resolution of 0.38 x 0.37 x 0.74 mm for generating SWI and visualizing these intricate structures. While the need for high resolution impacted signal-to-noise ratio (SNR), a consistent pattern of veins was identified, particularly around the basal vein. In this work we used a single threshold across the image, but it is possible that an local thresholding might provide improvements.

Our findings correspond well to the superficial arteries and veins extracted from a cadaver hippocampus (Wen et al., 1999), as illustrated in Figure 5.23. The PCA and its associated branches were prominently delineated, while the AChA, basal vein, and subependymal

intrahippocampus vein were also identified. This show the potential, validity and utility of our preliminary investigation in portraying the hippocampal vasculature.

5.6 CONCLUSION

In essence, this preliminary study serves as a foundational stepping stone toward potential advancements in comprehending the complex interplay between hippocampal vasculature and degenerative pathologies, all propelled by the application of non-contrast imaging methods. By shedding light on the intricate vascular networks within the hippocampus, our findings not only open avenues for further explorations but also underscore the practicability of gleaning invaluable insights from these imaging modalities. Furthermore, our study paves the way for investigating variations into the diameters of arteries and veins among individuals with neurodegenerative diseases, potentially illuminating whether these changes could serve as pivotal triggers for such conditions.

5.7 REFERENCES

Akasaka, T., Fujimoto, K., Yamamoto, T., Okada, T., Fushumi, Y., Yamamoto, A., Tanaka, T., & Togashi, K. (2016). Optimization of regularization parameters in compressed sensing of magnetic resonance angiography: Can statistical image metrics mimic radiologists' perception? *PLoS ONE*, *11*(1), 1–14. https://doi.org/10.1371/journal.pone.0146548

Braak, H., & Braak, E. (1991). Acta H ' pathologica Neuropathological stageing of Alzheimer-related changes. In *Acta Neuropathol* (Vol. 82).

Buch, S., Chen, Y., Jella, P., Ge, Y., & Haacke, E. M. (2022). Vascular mapping of the human hippocampus using Ferumoxytol-enhanced MRI: Intra-hippocampal vascular density. *NeuroImage*, *250*(January), 118957. https://doi.org/10.1016/j.neuroimage.2022.118957

Buch, S., Subramanian, K., Jella, P. K., Chen, Y., Wu, Z., Shah, K., Bernitsas, E., Ge, Y., & Haacke, E. M. (2021). Revealing vascular abnormalities and measuring small vessel density in multiple sclerosis lesions using USPIO. *NeuroImage: Clinical*, *29*(November 2020), 102525. https://doi.org/10.1016/j.nicl.2020.102525

Buch, S., Wang, Y., Park, M. G., Jella, P. K., Hu, J., Chen, Y., Shah, K., Ge, Y., & Haacke, E. M. (2020). Subvoxel vascular imaging of the midbrain using USPIO-Enhanced MRI. *NeuroImage*, *220*(March), 117106. https://doi.org/10.1016/j.neuroimage.2020.117106

Buck, M. H. S., Jezzard, P., & Hess, A. T. (2022). Optimization of undersampling parameters for 3D intracranial compressed sensing MR angiography at 7 T . *Magnetic Resonance in Medicine*. https://doi.org/10.1002/mrm.29236

Erdem, A., Gazi, M., & Roth, P. (1993). Microsurgical anatomy of the ethmoid. *Surgical and Radiologic Anatomy*, *15*(1), 9–14. https://doi.org/10.1007/BF01629855

Fulop, G. A., Ahire, C., Csipo, T., Tarantini, S., Kiss, T., Balasubramanian, P.,

Yabluchanskiy, A., Farkas, E., Toth, A., Nyúl-Tóth, Á., Toth, P., Csiszar, A., & Ungvari, Z. (2019). Cerebral venous congestion promotes blood-brain barrier disruption and neuroinflammation, impairing cognitive function in mice. *GeroScience*, *41*(5), 575–589. https://doi.org/10.1007/s11357-019-00110-1

Haacke, E. M., Xu, Y., Cheng, Y. C. N., & Reichenbach, J. R. (2004). Susceptibility weighted imaging (SWI). *Magnetic Resonance in Medicine*, *52*(3), 612–618. https://doi.org/10.1002/mrm.20198

Haegelen, C., Berton, E., Darnault, P., & Morandi, X. (2012). A revised classification of the temporal branches of the posterior cerebral artery. *Surgical and Radiologic Anatomy*, *34*(5), 385–391. https://doi.org/10.1007/s00276-011-0921-8

Henri Duvernoy, Françoise Cattin, P.-Y. R. (2013). The Human Hippocampus. In *Vascularisation* (3rd ed., pp. 69–105). Springer Nature Switzerland.

Isolan, G. R., Stefani, M. A., Schneider, F. L., Claudino, H. A., Yu, Y. H., Choi, G. G., Telles, J. P. M., Rabelo, N. N., & Figueiredo, E. G. (2020). Hippocampal vascularization: Proposal for a new classification. *Surgical Neurology International*, *11*(378), 1–6. https://doi.org/10.25259/SNI_708_2020

Jack, C. R., Wengenack, T. M., Reyes, D. A., Garwood, M., Curran, G. L., Borowski, B. J., Lin, J., Preboske, G. M., Holasek, S. S., Adriany, G., & Poduslo, J. F. (2005). *Neurobiology of Disease In Vivo Magnetic Resonance Microimaging of Individual Amyloid Plaques in Alzheimer's Transgenic Mice*. https://doi.org/10.1523/JNEUROSCI.2588-05.2005

Jenkinson, M., Bannister, P., Brady, M., & Smith, S. (2002). Improved Optimization for the Robust and Accurate Linear Registration and Motion Correction of Brain Images. *NeuroImage*, *17*(2), 825–841. https://doi.org/10.1006/nimg.2002.1132

Liu, S., Brisset, J. C., Hu, J., Haacke, E. M., & Ge, Y. (2018). Susceptibility weighted

imaging and quantitative susceptibility mapping of the cerebral vasculature using ferumoxytol. *Journal of Magnetic Resonance Imaging*, *47*(3), 621–633. https://doi.org/10.1002/jmri.25809

Manjon, J. V., Romero, J. E., & Coupe, P. (2020). *DeepHIPS: A novel Deep Learning based Hippocampus Subfield Segmentation method*. *February*. http://arxiv.org/abs/2001.11789

Marinković, S., Milisavljević, M., & Puškaš, L. (1992). Microvascular anatomy of the hippocampal formation. *Surgical Neurology*, *37*(5), 339–349. https://doi.org/10.1016/0090-3019(92)90001-4

Prades, J. M., Veyret, C., & Martin, C. (1993). Microsurgical anatomy of the ethmoid. *Surgical and Radiologic Anatomy*, *15*(1), 9–14. https://doi.org/10.1007/BF01629855

Sailer, A. M. H., Wagemans, B. A. J. M., Nelemans, P. J., De Graaf, R., & Van Zwam, W. H. (2014). Diagnosing intracranial aneurysms with mr angiography : Systematic review and meta-analysis. *Stroke*, *45*(1), 119–126. https://doi.org/10.1161/STROKEAHA.113.003133

Shen, Y., Hu, J., Eteer, K., Chen, Y., Buch, S., Alhourani, H., Shah, K., Jiang, Q., Ge, Y., & Haacke, E. M. (2020). Detecting sub-voxel microvasculature with USPIO-enhanced susceptibility-weighted MRI at 7 T. *Magnetic Resonance Imaging*, *67*(September 2019), 90–100. https://doi.org/10.1016/j.mri.2019.12.010

Spallazzi, M., Dobisch, L., Becke, A., Berron, D., Stucht, D., Oeltze-Jafra, S., Caffarra, P., Speck, O., & Düzel, E. (2019). Hippocampal vascularization patterns: A high-resolution 7 Tesla time-of-flight magnetic resonance angiography study. *NeuroImage: Clinical*, *21*(May 2018). https://doi.org/10.1016/j.nicl.2018.11.019

Wen, H. T. M. ., Rhoton, A. L. J. M. ., de Oliveira, E. M. ., Cardoso, A. C. C. M. ., & Tedeschi, H. M. . (1999). *Microsurgical Anatomy of the Temporal Lobe: Part 1: Mesial Temporal Lobe Anatomy and Its Vascular Relationships as Applied to*

Amygdalohippocampectomy (p. 549). Neurosurgery.

Wrede, K. H., Johst, S., Dammann, P., Özkan, N., Mönninghoff, C., Kraemer, M., Maderwald, S., Ladd, M. E., Sure, U., Umutlu, L., & Schlamann, M. (2014). Improved cerebral time-of-flight magnetic resonance angiography at 7 Tesla - Feasibility study and preliminary results using optimized venous saturation pulses. *PLoS ONE*, *9*(9). https://doi.org/10.1371/journal.pone.0106697

Yushkevich, P. A., Pluta, J. B., Wang, H., Xie, L., Ding, S. L., Gertje, E. C., Mancuso, L., Kliot, D., Das, S. R., & Wolk, D. A. (2015). Automated volumetry and regional thickness analysis of hippocampal subfields and medial temporal cortical structures in mild cognitive impairment. *Human Brain Mapping*, *36*(1), 258–287. https://doi.org/10.1002/hbm.22627

Zhang, X., Yin, X., Zhang, J., Li, A., Gong, H., Luo, Q., Zhang, H., Gao, Z., & Jiang, H. (2019). High-resolution mapping of brain vasculature and its impairment in the hippocampus of Alzheimer's disease mice. *National Science Review*, *6*(6), 1223–1238. https://doi.org/10.1093/nsr/nwz124

CHAPTER SIX

6.0 CONCLUSIONS

6.1 SUMMARY

The hippocampus is an important brain structure located in the medial temporal lobe on both sides of the brainstem near to the cerebellum. It is involved in many brain functions such as memory and spatial reasoning (Manjon et al., 2020). Alzheimer's disease is a devastating and widespread illness that affects millions of people worldwide. It is a neurodegenerative disease which occurs as a result of the degeneration of the hippocampus (H Braak & Braak, 1991). The current diagnostic methods for AD are often invasive and expensive, making it difficult to detect the disease in its early stages. This thesis seeks to address this issue by investigating the potential use of high resolution 7T MRI to study the vascularity, susceptibility, and volume of the hippocampus in AD patients and healthy controls. By identifying a non-invasive and cost-effective biomarker for early diagnosis of AD, we could potentially improve patient outcomes, reduce the burden on healthcare systems, and enhance our understanding of this debilitating disease. Additionally, this research has the potential to pave the way for new treatment options and therapeutic interventions aimed at slowing or even reversing the progression of AD.

In Chapter 3, we conducted a thorough investigation of the reproducibility of measurements of the susceptibility and volume of the hippocampal subfields using high resolution T_2*, T_2- and T_1-weighted images. Our study focused on segmenting the hippocampal subfields using ASHS (Yushkevich et al., 2015b) and then obtaining the subfield volumes. We also assessed the average magnetic susceptibility in the different sub-fields. To do this, we used susceptibility maps of the brain generated using a robust multi-scale approach to quantitative susceptibility mapping (QSM) (Acosta-Cabronero et al., 2018).

The data we used for the analysis was obtained from the UK7T travelling heads study (Clarke et al., 2020a) which was collected from 5 different 7T scanners at sites in the UK. The results of our study were highly promising, we established that the susceptibility and volume of the hippocampal subfields can be measured with some degree of reproducibility. These measurements provide an assessment of the level of susceptibility change that can be reliably characterised using high-resolution QSM in healthy subjects.

Overall, these findings demonstrate the potential for using high resolution imaging techniques to successfully measure the susceptibility and volume of the hippocampus subfields, which could prove to be a valuable tool in studying the structural changes associated with Alzheimer's disease.

Building upon the reproducibility of the susceptibility and volume measurements of the hippocampus discussed in Chapter 3, Chapter 4 delved deeper into the potential clinical applications of these measurements. By comparing the values of magnetic susceptibility and volume of the hippocampal sub-fields between Alzheimer's disease patients and healthy controls, we were able to identify statistical significant differences that suggest the possibility of using high-field-high-resolution MRI as a biomarker for early detection of the disease.

Moreover, by correlating the susceptibility and volume measurements with CSF proteins, we were able to establish a strong association between the volume of the entorhinal cortex and Amyloid$\beta_{1\text{-}42}$ concentration, further supporting the potential of using MRI as a biomarker for Alzheimer's disease. Additionally, we found a correlation between the susceptibility of specific hippocampal subfields such as the dentate gyrus and cornu Ammonis and cognitive scores as measured by the Montreal Cognitive Assessment (MoCA), providing another potential avenue for early detection of Alzheimer's disease.

These findings have important clinical implications as early detection of Alzheimer's disease can lead to better management of the disease and improved patient outcomes.

Chapter 5 of the thesis utilized high resolution time-of-flight imaging with an isotropic resolution of 0.38 mm to identify the arteries supplying blood to the hippocampus, and high resolution, 3D GRE T_2* scanning with a resolution of 0.38 x 0.37 x 0.74 mm^3 to generate susceptibility weighted images for the identification of veins draining blood from the hippocampus. One noteworthy aspect of this work is that the imaging was performed without the application of any contrast agent. The results obtained for the vascularization of the hippocampus were compared to those of post-mortem studies, and the similarities were striking. The major arteries and veins supplying and draining the hippocampus could be easily identified. Understanding the vasculature of the hippocampus is important, as it provides valuable insights into how diseases affect this brain structure, potential changes in its function, and the success rate of surgeries performed in this region.

6.2 FUTURE WORK

In addition to the limitations and future directions mentioned in the individual chapters, there are other avenues for future research that could be explored. For instance, the current study only focused on the relationship between hippocampal vascularity, susceptibility, and volume in AD, but there are other neurodegenerative diseases such as Parkinson's and Huntington's diseases that could also be investigated in future studies. Also, a deeper understanding of the relationship between the changes in the volume and susceptibility of the hippocampus and its subfields and the progression of Alzheimer's disease could be gained through longitudinal studies that follow participants over time. This could help establish a more accurate and comprehensive understanding of the biomarkers of AD, as well as providing insights into potential interventions and treatments.

Furthermore, the current study only looked at structural changes in the hippocampus, but functional changes could also be explored using techniques such as functional MRI (fMRI).

Combining structural and functional imaging could provide a more comprehensive understanding of how neurodegenerative diseases affect the hippocampus.

Finally, the use of artificial intelligence and machine learning could also be explored in future studies to develop more accurate and reliable biomarkers for early detection of AD and other neurodegenerative diseases. In particular the development of new image processing techniques based on deep learning algorithms (Salvi et al., 2021), could help reduce the effects of motion artifacts and improve the precision of imaging data. Similar approaches could be used for automatic categorization of the vascularization patterns observed in this hippocampus. This could further enhance the reproducibility of the results and increase the clinical utility of high-resolution MRI in the diagnosis and monitoring of neurodegenerative diseases.

6.3 REFERENCE

Acosta-Cabronero, J., Milovic, C., Mattern, H., Tejos, C., Speck, O., & Callaghan, M. F. (2018). A robust multi-scale approach to quantitative susceptibility mapping. *NeuroImage*, *183*, 7–24. https://doi.org/10.1016/j.neuroimage.2018.07.065

Braak, H., & Braak, E. (1991). Acta H ' pathologica Neuropathological stageing of Alzheimer-related changes. In *Acta Neuropathol* (Vol. 82).

Clarke, W. T., Mougin, O., Driver, I. D., Rua, C., Morgan, A. T., Asghar, M., Clare, S., Francis, S., Wise, R. G., Rodgers, C. T., Carpenter, A., Muir, K., & Bowtell, R. (2020). Multi-site harmonization of 7 tesla MRI neuroimaging protocols. *NeuroImage*, *206*(October 2019), 116335. https://doi.org/10.1016/j.neuroimage.2019.116335

Manjon, J. V., Romero, J. E., & Coupe, P. (2020). *DeepHIPS: A novel Deep Learning based Hippocampus Subfield Segmentation method*. *February*. http://arxiv.org/abs/2001.11789

Salvi, M., Acharya, U. R., Molinari, F., & Meiburger, K. M. (2021). The impact of pre- and post-image processing techniques on deep learning frameworks: A comprehensive review for digital pathology image analysis. *Computers in Biology and Medicine*, *128*, 104129. https://doi.org/10.1016/j.compbiomed.2020.104129

Yushkevich, P. A., Pluta, J. B., Wang, H., Xie, L., Ding, S. L., Gertje, E. C., Mancuso, L., Kliot, D., Das, S. R., & Wolk, D. A. (2015). Automated volumetry and regional thickness analysis of hippocampal subfields and medial temporal cortical structures in mild cognitive impairment. *Human Brain Mapping*, *36*(1), 258–287. https://doi.org/10.1002/hbm.22627